



AFOSR TR-81-0497

18

19

6

UNIVERSITY OF NEVADA - RENO - NEVADA - 89557

LEVEL

Mackay School of Mines
Seismological Laboratory

Telephone (702) 784-4975

(9) FINAL TECHNICAL REPORT 1 Oct 78-

(11) 1 May 81

30 Apr 81

(12) 102

AD A100141

ARPA Order No.	3291
Program Code	7F10
Name of Contractor	University of Nevada, Reno
Effective Date of Contract	01 Oct 1978
Contract Expiration Date	01 May 1981
Amount of Contract Dollars	\$115,000
Contract Number	(15) F49620-77-C-0070 ✓ ARPA Order-3291
Principal Investigator	(10) William A. Peppin 702-784-4975
Program Manager	William A. Peppin
Short Title of Work	(6) Close-in and Regional Source Studies for Seismic Discrimination

DTIC
ELECTRONIC
JUN 12 1981

Sponsored by

Advanced Research Projects Agency (DOD)

ARPA Order No. 3291

Monitored by AFOSR under Contract # F49620-77-C-0070

WIC FILE COPY

81 6 12 082

A DIVISION OF THE UNIVERSITY OF NEVADA SYSTEM

Approved for public release
distribution unlimited.

407259

TABLE OF CONTENTS

TECHNICAL REPORT SUMMARY	1
[1] ANALYSIS OF WIDEBAND DIGITAL DATA	1
A. The digital data set	2
B. Pictorial description of the data set	2
C. Discussion	3
[2] SEISMIC CHARACTERIZATION OF RUSSIAN EVENTS	6
[3] CLOSE-IN ACCELEROMETER DATA	7
[4] AMPLITUDE-YIELD SCALING RELATIONS OF CHEMICAL EXPLOSIONS	11
[5] THE PN-RAYLEIGH AND ANOTHER NEAR-REGIONAL DISCRIMINANT	19
[6] IMPULSE SOLUTIONS IN A LAYERED ELASTIC MEDIUM: EXTENDED LAMB'S PROBLEM	25
[7] SEISMIC DISCRIMINATION USING ONLY PN	48

Accession For	
NTIS GRA&I	<input checked="" type="checkbox"/>
DTIC TAB	<input checked="" type="checkbox"/>
Unannounced	<input checked="" type="checkbox"/>
Justification	
By	
Distribution/	
Availability Codes	
Dist	Avail and/or Special
A	

AIR FORCE OFFICE OF SCIENTIFIC RESEARCH (AFSC)
NOTICE OF TRANSMITTAL TO DDC
This technical report has been reviewed and is
approved for public release IAW AFR 190-12 (7b).
Distribution is unlimited.
A. D. BLOSE
Technical Information Officer

TECHNICAL REPORT SUMMARY

This report covers contract work for the time period 01 Oct 1978 to 30 Apr 1981. The time has been the most successful and productive that I have spent on DARPA/AFOSR objectives in seismic discrimination. The report is divided into two parts. The first part describes contract work that is now being written up in publishable manuscripts. Topics covered include: [1] analysis of wideband digital data for elucidation of the seismic source (two manuscripts in preparation), [2] analysis of eastern Kazakh explosions for the effects of anomalous tectonic excitation (1 in preparation), and [3] an evaluation of the seismic moment tensor method for analysis of close-in accelerometer data of the JORUM, PIPKIN,, and HANDLEY tests (1 in preparation). The second part of the report consists of 4 manuscripts that have been completed for submission to the journals. Topics covered include: [4] amplitude-yield scaling of chemical explosions; [5] new evidence on the Pn-Rayleigh and another near-regional seismic discriminant, [6] the computation of near-field canonical sources by exact theory in a multilayered medium, and [7] seismic discrimination at near-regional distances using only Pn.

[1] ANALYSIS OF WIDEBAND DIGITAL DATA

Ever since my participation in the Near-Field Project sponsored by AFOSR, I have felt that a primary, ongoing need for the advancement of earthquake source theory is the acquisition of better data than had hitherto been available; source models are numerous, but seismologists still disagree on some of the most fundamental points. Therefore, I have felt a responsibility to obtain such data as time and resources have permitted. With the advent of digital event-recording seismographs, we began a program of digital data acquisition on eastern Sierra earthquake sequences. The rate of data return has been very high compared with the modest costs of acquiring it.

We were fortunate in that eastern Sierra seismicity began to increase, af-

fording the opportunity to record a number of distinct aftershock sequences. We were extremely fortunate to have placed event recorders in the field 6 months prior to the onset of the major sequence at Mammoth Lakes, culminating in ten ML 5+ events in the last week of May, 1980. The area is of considerable tectonic interest, and these sequences led us to a number of research projects (Somerville and Peppin, 1980a,b; Peppin and Somerville, 1980; Peppin and Somerville, 1981a). The work relevant to DARPA was done on an extension of the original contract, and involved processing the digital data acquired. This work will be described in two manuscripts in preparation (Peppin and Somerville, 1981b; Somerville and Peppin, 1981).

A. The digital data set

In Figure 1.1 is presented an image showing the locations and number of three-component digital seismograms recorded. The data is recorded wideband displacement flat (0.1 to 50 Hz) using seismograph systems as described by Peppin and Bufe (1980). Altogether some 1,500 3-component seismograms were analyzed. For almost all events analysis consisted of: (1) dumping the digital data to named mass-storage files; (2) computing amplitude spectra of the vertical-component P and horizontal-component S-waves; (3) constructing plots of all data traces and spectra; (4) measuring spectral corner frequencies; (5) computing seismic moment from the long-period spectral asymptote; and (6) computing synthetic Wood-Anderson magnitudes. In addition we have computed adjusted Berkeley magnitudes where possible and seismic stress drop using Brune's (1970, 1971) formulas. More detailed analysis awaits obtaining accurate locations for study events of interest, a problem rendered nontrivial for several reasons, mostly because of complex geology, poor station distribution, and record overlap in foreshocks. Data quality is superior, with large signal-to-noise ratio extending over most or all of the recording bandwidth.

B. Pictorial description of the data set

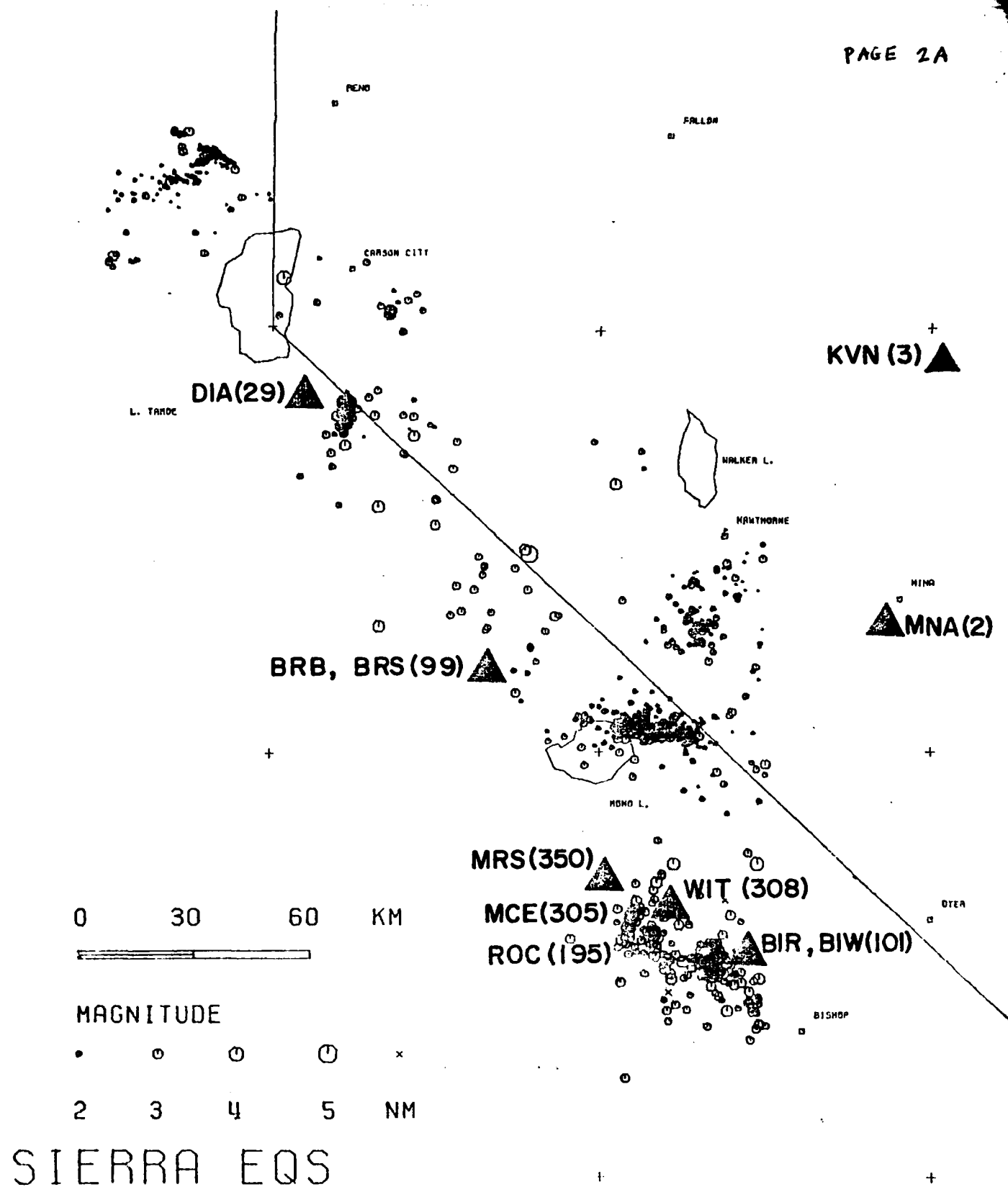


Figure 1.1. Indicating station names where digital data was collected and the number of three-component records obtained at each site. Seismicity 1975-1979 is shown also.

For so large a data set, it is of interest to provide some sort of visual characterization. Presented here are plots of log seismic moment versus ML (Figures 1.2 and 1.3), log of seismic moment versus P- and S-wave spectral corner frequency (Figures 1.4 and 1.5), log of seismic moment versus their ratio (Figure 1.6), and their ratio versus P-wave spectral corner frequency (Figure 1.7).

C. Discussion

The original purpose of this experiment was to acquire a set of excellent data close to the source of earthquakes. Then we could experiment with waveform inversion methods for determining the seismic source function. One problem in particular remains in question today, namely: what source parameter relates to the time duration of seismic waves emanating from the source (or similarly, to the spectral corner frequencies of P and S waves)? The prevailing view has been that the spatial source dimension (i.e., length of faulting) controls the observed frequencies. However, Helmberger and colleagues have had good success modelling moderate earthquakes essentially as point sources in their studies of teleseismic body waves. Indeed, for our data set it is remarkable how far the point-source approximation can be taken. In Figure 1.8 we show data recorded close (1 second S - P time) to two sizeable Mammoth aftershocks. Synthetic seismograms for a point source in a halfspace have also been prepared, and the fits are remarkable under the circumstances. The larger earthquake has a seismic moment of 1.7E23 dyne-cm, one of the bigger events in the sequence. And yet, as can be seen, the effect of source finiteness is difficult to identify.

Hanks (1981) explains how the point-source assumption, if incorrect, could lead to distinctly wrong values of mantle Q for P (versus S) waves. The reason for the problem is this. What if in fact it is a general result that the P-waves leaving the source are richer in high frequencies than the S-waves. Then we would expect to see this effect in teleseismic body waves (which we do). But if the difference is then attributed to whole-path Q, we will erroneously

$$\text{LOG } M_0 = (0.89 \pm 0.02) \text{ML} + (17.29 \pm 0.07)$$

N = 714

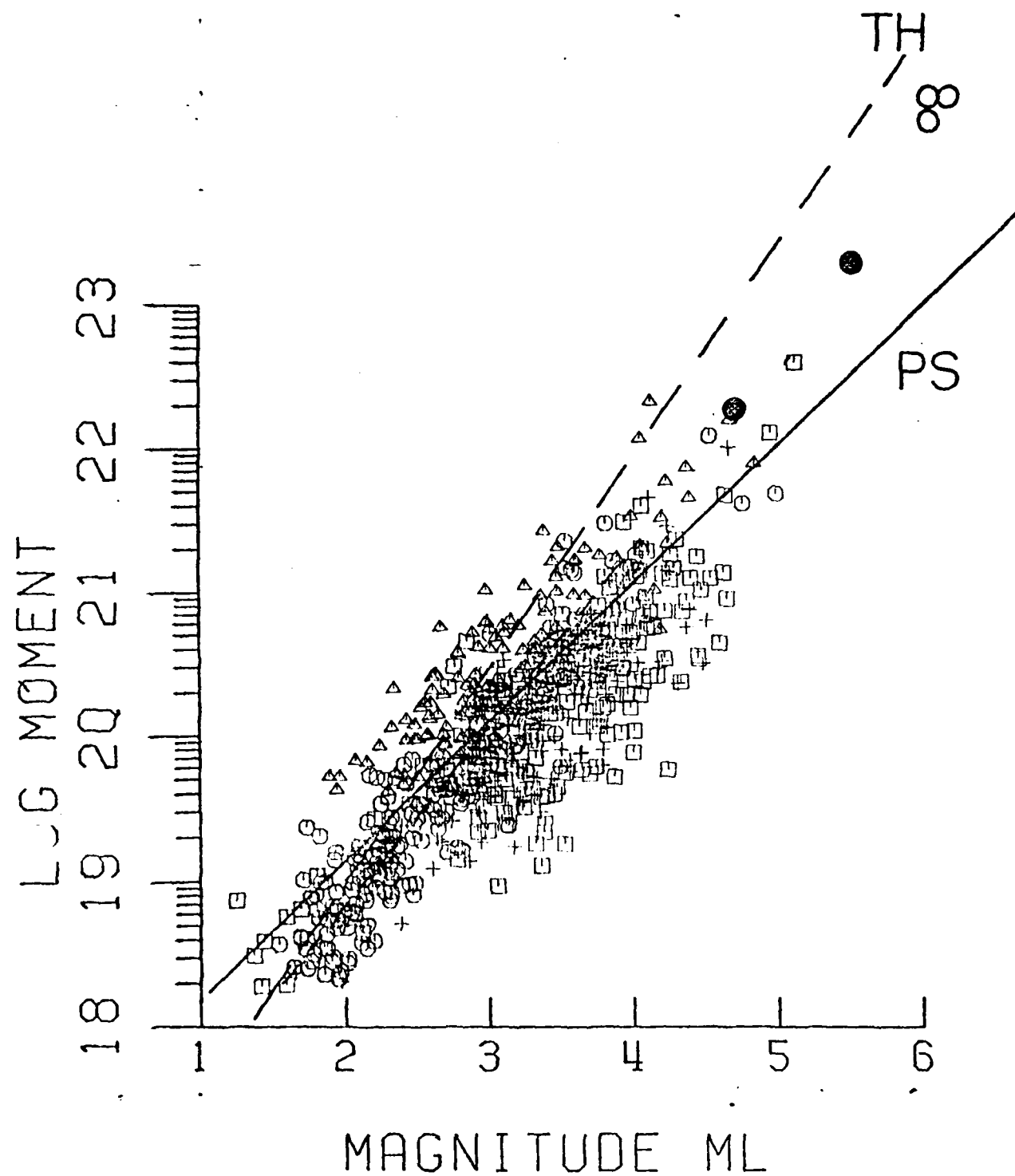


Figure 1.2. Log seismic moment versus local magnitude computed synthetically. The regression line "PS" is given above. Dashed line for southern California events (Thatcher and Hanks, 1973). Solid circles: moments by time-domain fits; open circles: estimates of moment from Uhrhammer and Furguson (1980).

$$\text{LOG } M_0 = (0.73 \pm 0.04) \text{ML} + (18.23 \pm 0.15)$$

N = 300

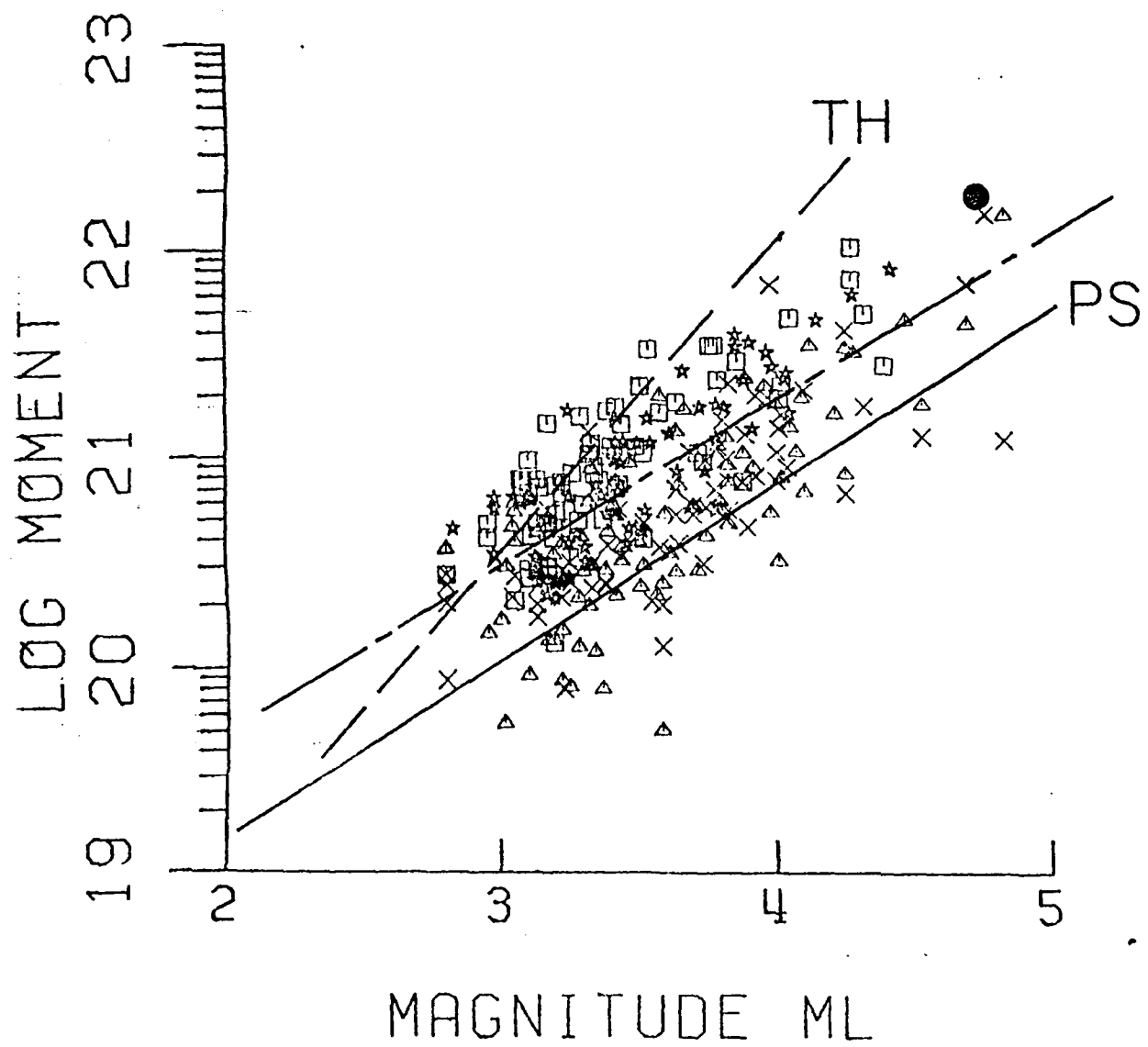
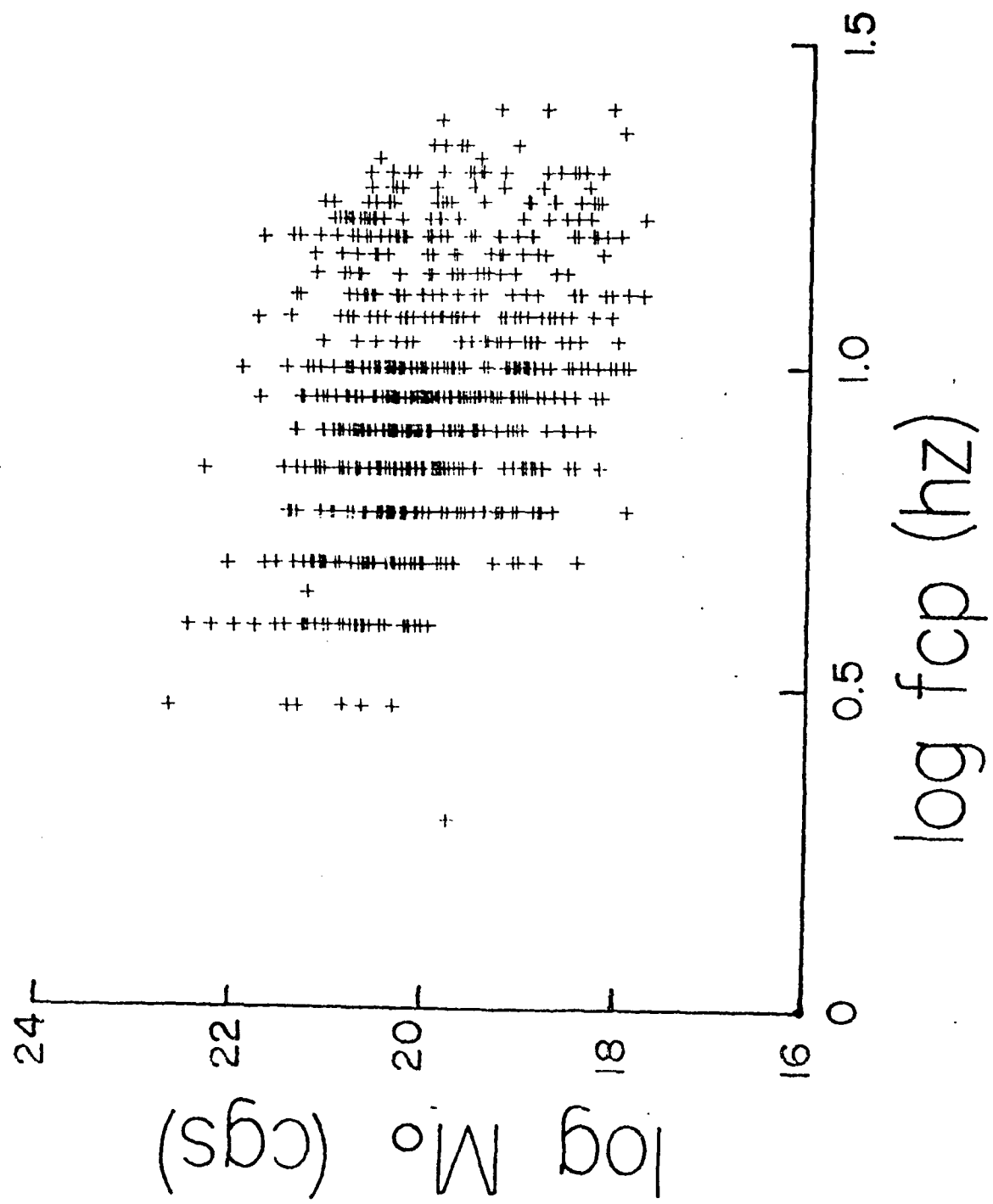


Figure 1.3. Same format as Figure 1.2, but the magnitudes are adjusted Berkeley ones. Only events recorded at Mammoth Lakes represented here. Different symbols are different stations.



Fig

Figure 1.4. Log seismic moment versus log of the vertical-component P-wave spectral corner frequency. These were inferred by overlaying templates on the spectra and picking the corners by eye, most to within a confidence range of about 20%.

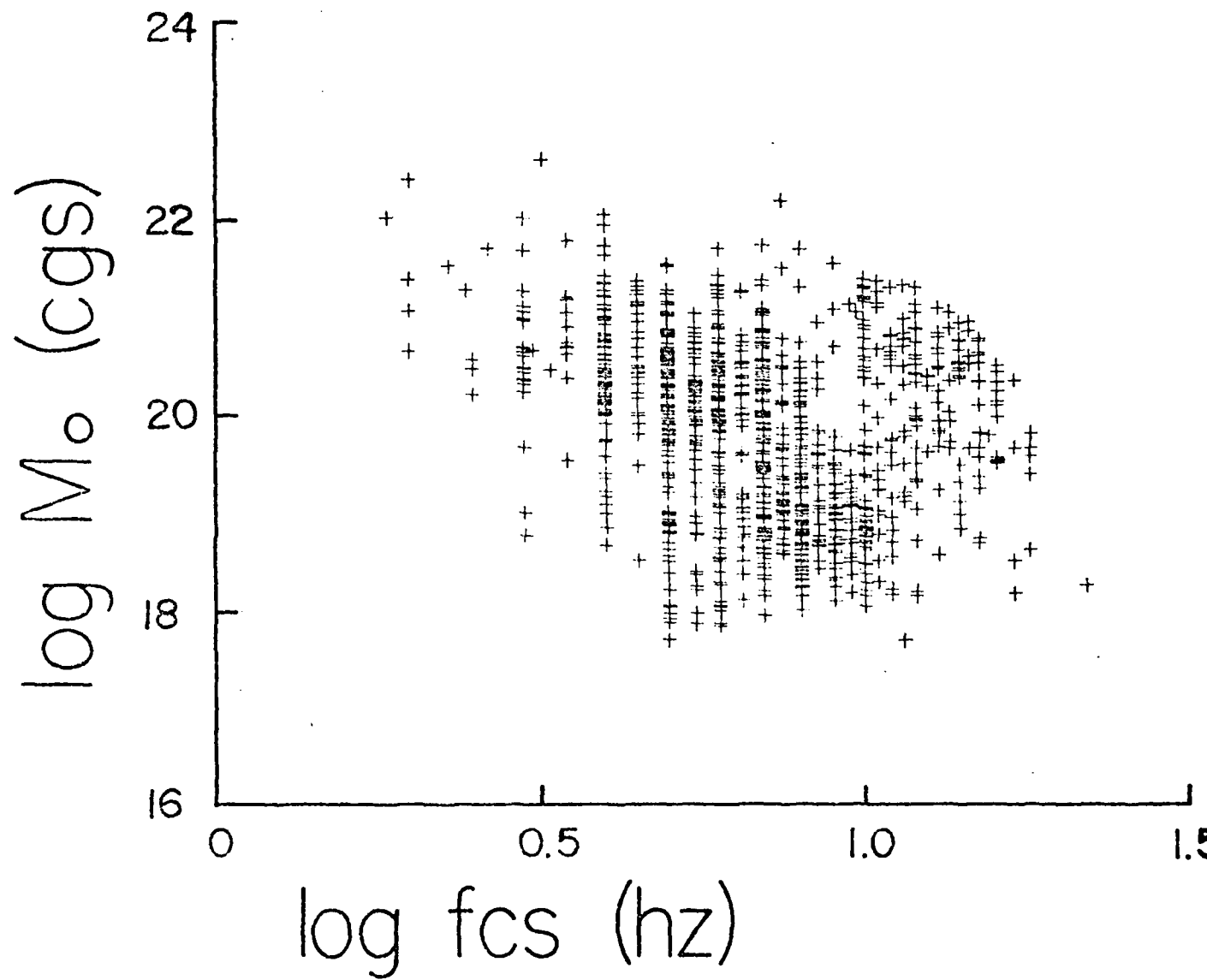


Figure 1.5. Log of seismic moment versus log of horizontal-component S-wave spectral corner frequency. Inferred by overlaying a template and picking by eye. Most are precise to about 20%.

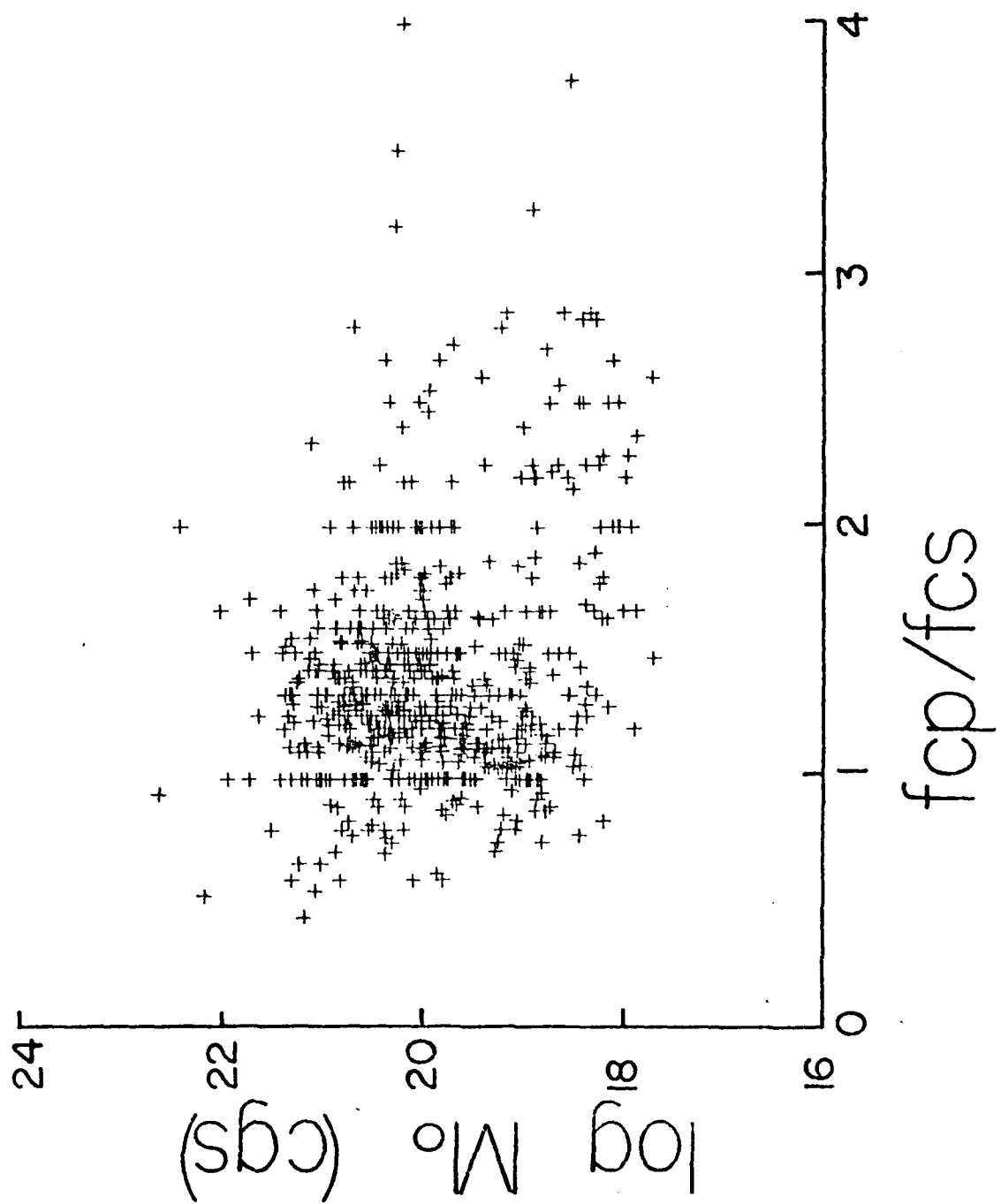


Figure 1.6. Log of seismic moment versus the ratio "R" of vertical-component P versus horizontal-component S spectral corner frequency. Because of overlapping points, it is not clear in the figure that the average of all values is about 1.3.

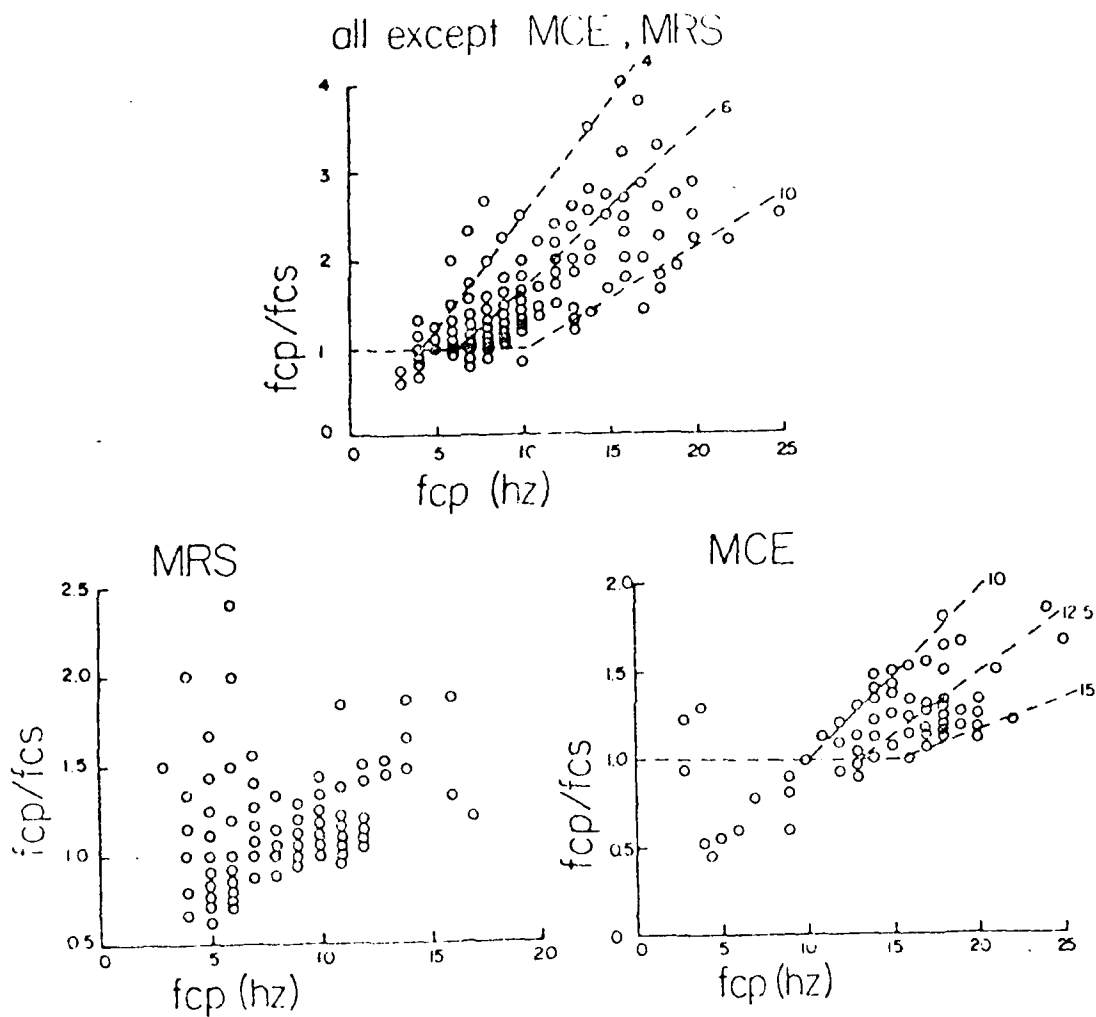


Figure 1.7. Spectral corner-frequency ratio "R" versus vertical-component P-wave spectral corner frequency at all stations except MCE and MRS (top), MRS (lower left), and MCE (lower right). Dashed lines are trend lines predicted as described in text. Numerals beside each line indicate cutoff frequency for S selected. At all stations except MRS there seems to be a noticeable correlation between R and the P-wave spectral corner frequency.

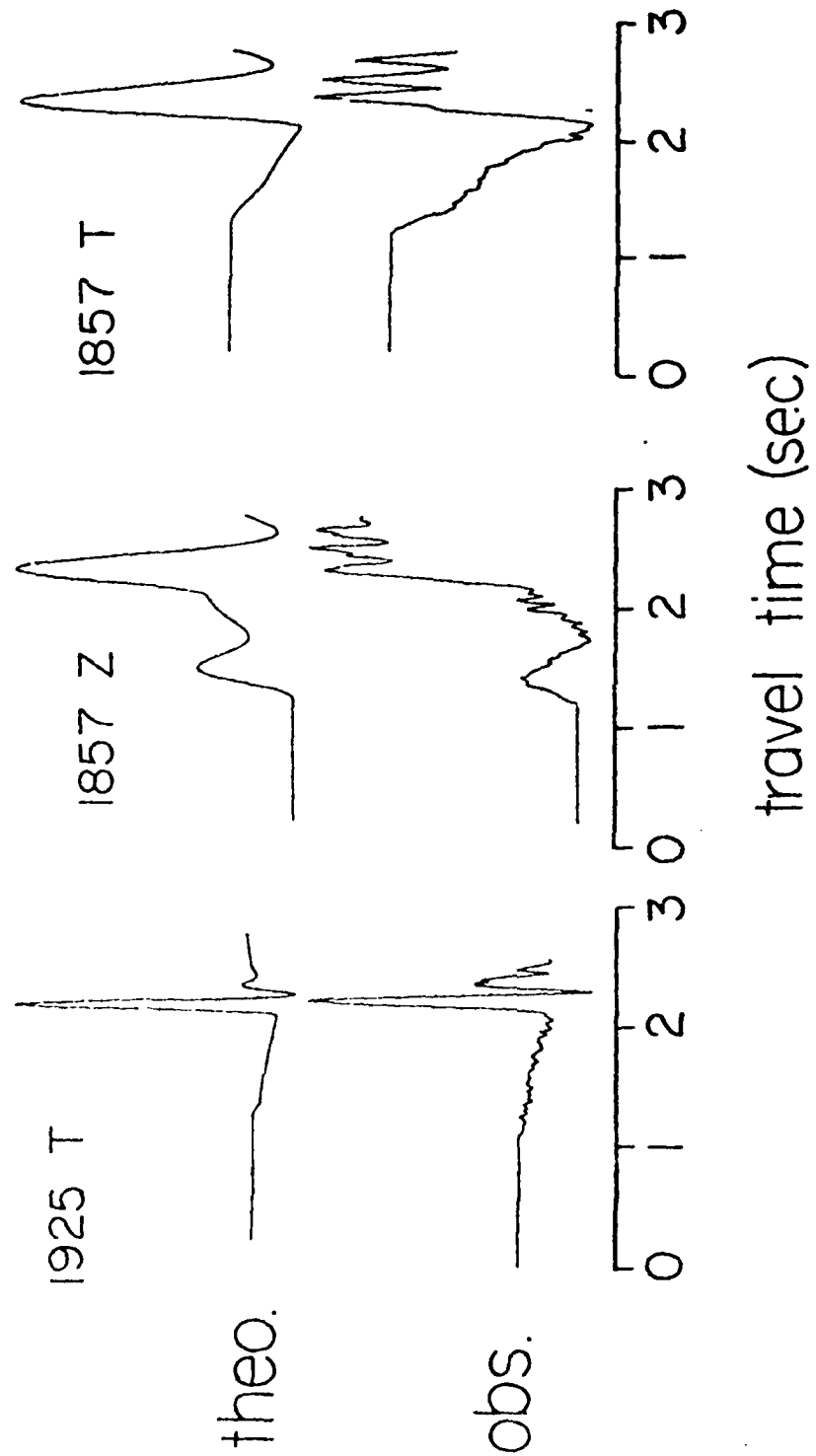


Figure 1.8. Observed and theoretical seismograms for two large events, 26 May 1925, ML 4.6 (left, transverse) and 26 May 1980 1857, ML 5.5 (vertical and transverse, right). Ramps between P and S phase are the near-field terms, visible on vertical as well as transverse components. For 1857 the preamplifiers are clipped after onset of the S-phase (last, large arrival on all traces).

infer values of Q for P too high relative to Q for S.

Now, says Hanks, we do see this frequency shift in the majority of data studies published, regardless of recording distance. Therefore, he asserts that the shift is a source effect, which implies that the length of the rupture zone controls the frequencies observed.

With the sizeable data set at hand, and given its superb quality, important new evidence can be brought to bear on this question. In Figure 1.6 we have plotted the ratio "R" of P to S wave spectral corner frequency for the events possessing good-quality corner frequencies on each phase. We see that the data support Hanks in that the P-waves appear to be enriched in high-frequency energy relative to S. However, we can give a different interpretation. At each recording station a "cutoff frequency" can almost always be identified for the S-waves spectral corners, but not the P. This cutoff is frequently quite clearly identifiable. Consider, for example, the data at the Whitmore station shown in Figure 1.9. The S-wave data seem cut off at all levels of seismic moment at about 7 Hz, while P-wave corners go up to 15 Hz or more for fairly large events. One obvious explanation for these facts is the action of anelastic attenuation. Suppose that this effect works in such a way as to band-limit S-waves while leaving P unaffected. Then we would expect R to correlate with P-wave spectral corner frequency.

In Figure 1.7 we suppose that R is unity at the source and that a separate cutoff frequency exists at each station for S. Above the cutoff the observations of R should begin to increase. The lines in Figure 1.7 are predicted trend lines on the assumption of varying cutoff frequencies for S; the fit to the observations is reasonable for cutoff values close to those as observed in Figure 1.9.

From this analysis we conclude that no statement can be made about conditions at the source based on the observations (Figures 1.4 and 1.7) until the

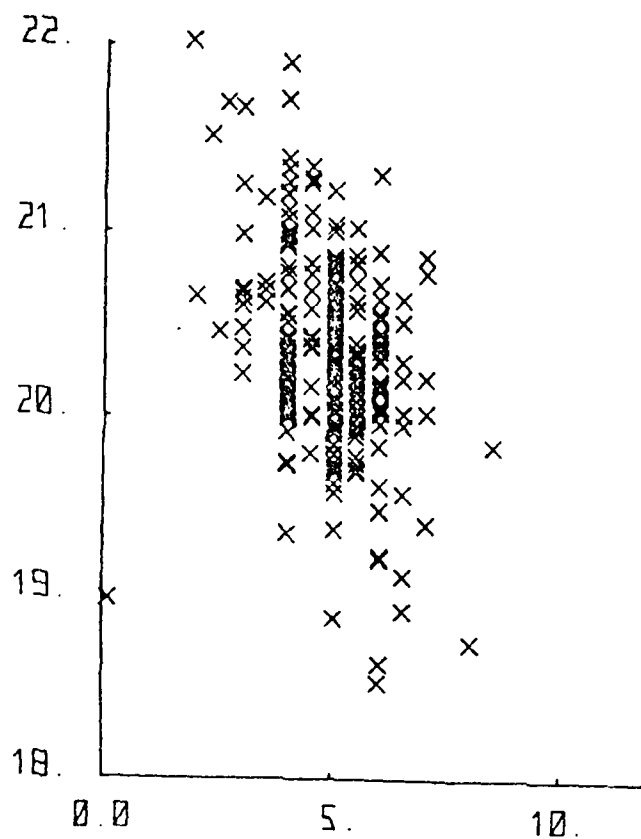


Figure 1.9. S-wave spectral corner frequency (abscissa) versus Log of seismic moment for events recorded at the Whitmore station. The corner frequency data are almost cutoff completely at 7 Hz. Such cutoffs can be identified at all of the stations except DIA.

effects of anelastic attenuation are better known, so that Hanks' (1981) premise is not justified for this data set. In fact, let cutoff frequencies be selected from Figure 1.7. Then let R be computed only when the P-wave corner is strictly not greater than this cutoff. At 8 of 9 stations, the average value of R is indistinguishable from unity (Table 1). In support of this general idea, note that the rate of falloff to high frequency is observed to be significantly greater in S-waves than in P-waves, consistent with the proposition that the S-waves are being more strongly affected by anelastic loss. In contrast, I know of no source theory that can predict such a difference in high-frequency falloff on elastic rheology.

To me all this means that R is probably unity at the source for these events. Then it must be the source rise time that dictates the spectral corner frequencies, not the spatial source dimension. If true, this result can also explain the observation of rather weak scaling of the P-wave spectral corner frequencies (factor of near 2 over 4 orders of magnitude in seismic moment). Source dimensions should scale more rapidly with moment than this on any reasonable hypothesis.

I believe these results are quite relevant to the DARPA discrimination program, because they relate in a fundamental way to our treatment of earthquake sources. I can see no way to make sense of the observations unless these earthquakes are strongly controlled at all magnitude levels by asperities of more-or-less limited size range (say 25 ± 10 m). In this case, high-frequency body waves are seeing the failure of rather small asperities, while surface waves are seeing the effects of a rupture that radiates out over a larger, but less energy-rich rupture surface. "Stress drop" for such a failure has no useful meaning when taken over the whole fault, but might have meaning correlative with the strength and/or texture of rocks in the source region. If this is a general result, it means that theoretical treatment of earthquake sources for the discrimination problem should be modified in fundamental ways; for earthquakes are then highly "dissimilar" in the sense of Aki (1967). If so, our dis-

Table 1. Spectral Corner Frequency Ratios

Station	Sequence	R(all data)	N	cutoff freq.	R (P cutoff)	N
MCE	Mammoth	1.17 ± .29	91	13	0.98 ± .26	30
MRS	Mammoth	1.18 ± .28	152	8	1.15 ± .33	81
ROC	Mammoth	1.33 ± .31	101	8	1.16 ± .26	44
WIT	Mammoth	1.61 ± .53	160	7	1.26 ± .27	62
BIR,BIW	Bishop	1.81 ± .66	37	8	1.12 ± .18	13
BRB,BRS	Bridgep.	1.62 ± .58	52	8	0.96 ± .09	11
DIA	Dia. Val.	2.30 ± .40	18	-	-----	--

crimination efforts should be directed more toward statistical measures of this dissimilarity in source regions of interest rather than the present heavy emphasis on waveform fitting using relatively simple sources. Where dissimilarity is great, scatter (hence overlap) of, say, Ms:mb populations of explosions and earthquakes can be expected.

[2] SEISMIC CHARACTERIZATION OF RUSSIAN EVENTS

Of recent interest to the DARPA program was the occurrence of the event of 07 July 1979, an eastern Kazakh presumed explosion showing a tremendous SH pulse at the SRO station ANTO (At a recent DARPA contractors' meeting, T. Fitch expressed the opinion that this pulse was not real; if so, then it is notorious that the motion is almost pure transverse on the two horizontal components relative to the great-circle travel path). Brian Stump and I were asked to analyze this event with a view toward answering the following 3 questions: (a) can the event be identified as an explosion? (b) can the tectonic orientation of the stresses involved in production of the SH phase be identified? (c) can we estimate the effects of the added earthquake component on the amplitude of short-period, vertical P (i.e., the effect on the body wave magnitude)?

Investigations completed so far can address (a) and (c) and indicate ways to proceed toward (b). We began by establishing a control event, that of 08 August 1979, for which the best short-period data was available, and for which no large SH pulse was evident on the SRO stations. Using eight SRO and ASRO stations, we inverted for the seismic moment tensor. For a Eurasian mantle structure provided by Helmberger and WKBJ analysis (Chapman, 1976; Dey-Sarker and Chapman, 1978) for the Green's functions, the following extreme (unsigned) values of the moment tensor $M_{ij}(t)$ were obtained:

$$\begin{bmatrix} 11.0 & 7.00 & 2.00 \\ 7.00 & 17.0 & 2.00 \\ 2.00 & 2.00 & 1.00 \end{bmatrix}$$

A pure explosion would have equal values on the diagonal and zeroes off the diagonal. Thus, the event is inferred to be part explosion and part earthquake. We consider the result a success because: (1) only vertical component P data was used; (2) good fits of the data at all stations and somewhat reliable time functions were obtained; (3) the phase sP was not included in the Green's function due to a bug in the WKBJ code (inclusion of this phase would no doubt drive down the off-diagonal elements that are very sensitive to S leaving the source). For samples of the fits of the data, see Figure 2.1, and for samples of the inferred motions at the source, see Figure 2.2.

Regarding the seismic discrimination question (a): it appears likely that the gross nature of the source—explosion or earthquake—can be resolved by this procedure using teleseismic body waves, although investigations of other explosions and earthquakes will be required to verify this. Our conclusion regarding (c) is that mb, hence inferred yield, is unlikely to be affected by "anomalous" tectonic excitation at the level of the 07 July 1979 event. Question (b) remains. Recent communications with C. H. Chapman have verified some mistakes in the WKBJ source terms employed by Stump and me for eastern Kazakh events. Thus, we need to recompute the necessary Green's functions incorporating the phase sP. For the 08 August 1979 event we were able to infer principal directions of stress for the deviatoric part of the solution. The results was a thrust mechanism with compression axis at N 15 deg E, plunge 10 degrees, and with tension axis at about S 20 deg E, plunge 50 degrees. These inferred directions are likely to be altered significantly by inclusion of sP in the Green's functions, but our other conclusions about these sources will probably not be altered substantively.

[3] CLOSE-IN ACCELEROMETER DATA

The University of California at Berkeley conducted experiments to record ground motions near several large underground explosions JORUM (16 Sept 1969), PIPKIN (08 Oct 1969), and HANDLEY (26 Mar 1970). Results of the analyses of

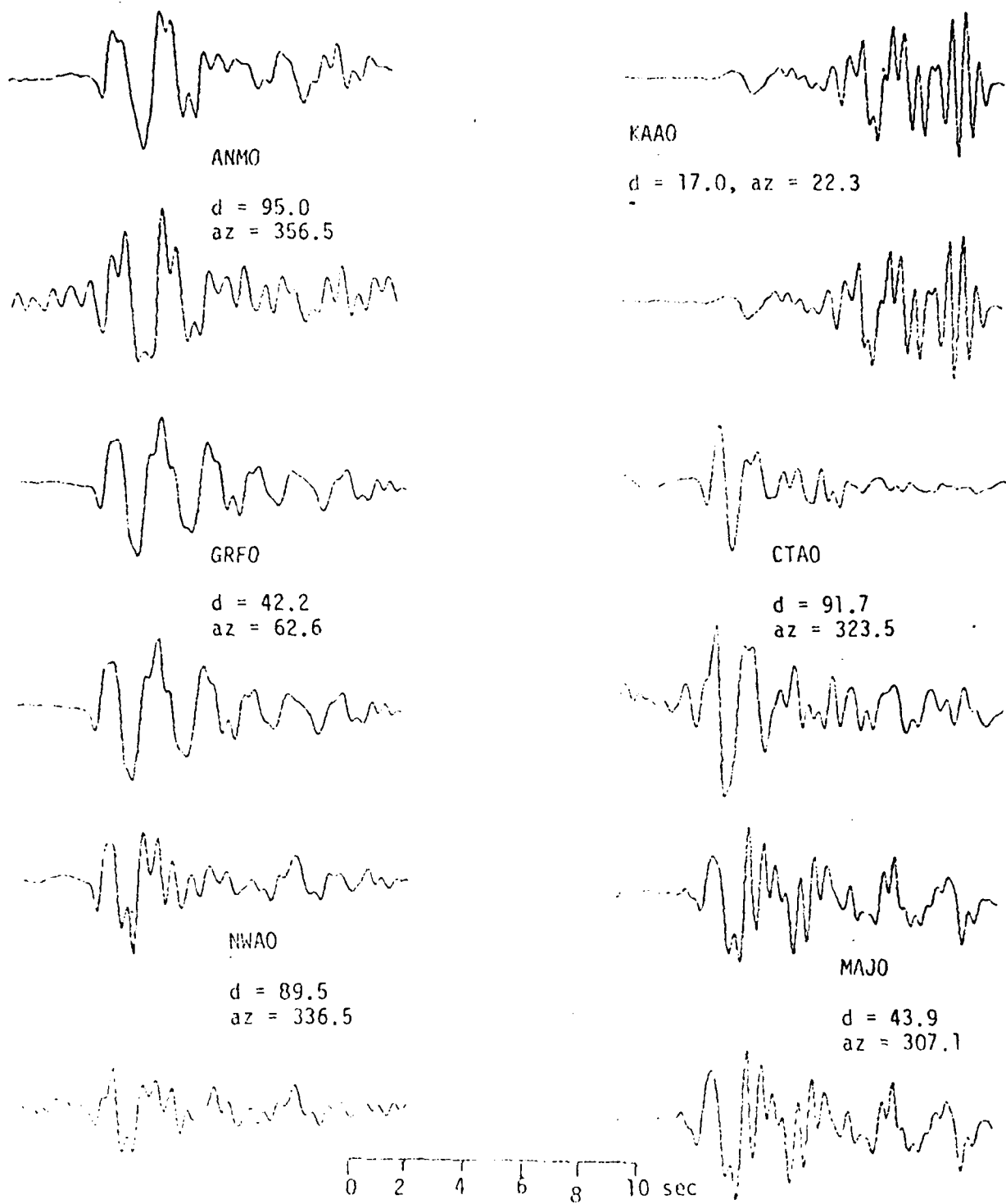


Figure 2.1. Data (top trace) and fit (bottom trace of each pair) that results from fitting 8 vertical-component short-period SRO and ASRO records of the eastern Kazakh explosion of 08 Aug 1979. Fits for stations not shown are as good, except the CHTO record. Distances in degrees ("d") and station-to-epicenter azimuth ("az") are given. Traces are scaled for relative amplitude between data and fits.

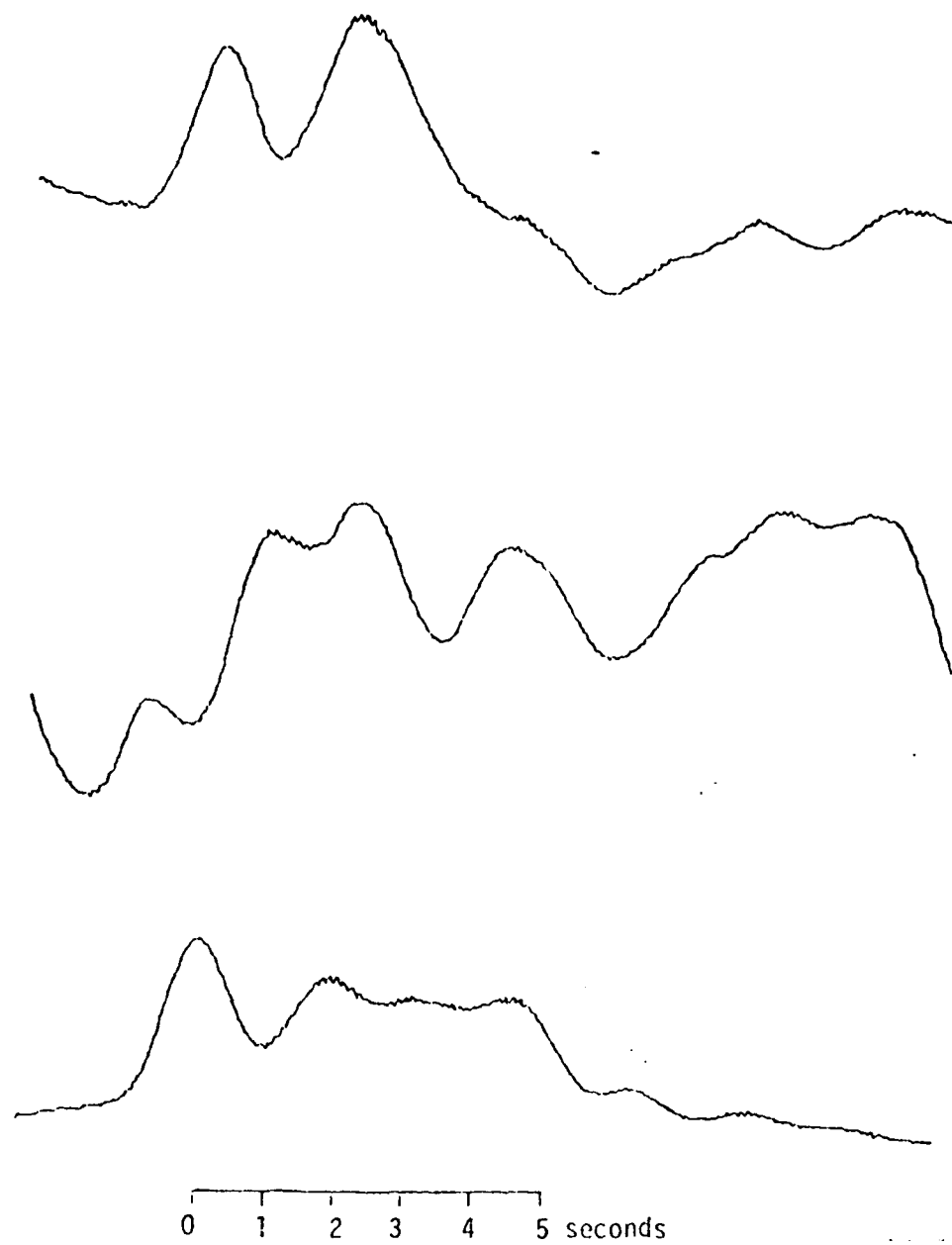


Figure 2.2. Inferred motions at the source for the eastern Kazakh explosion shown in Figure 2.1. Top: trace of the moment tensor (explosive part); Middle: $M_{12}(t)$; Bottom: $M_{22}(t)$. Note the prominent arrival after the onset suggestive of spall closure. Note the roughly steplike appearance of the deviatoric component (center trace). Finally, note that these records (top trace) seem to indicate that the explosive part of the source has overshoot.

these records are a major part of two theses (Peppin, 1974; Stump, 1979), as well as recent work by Helmberger and Hadley (1981) and Stump and Johnson (1981). The aim here has been: determine the source function of nuclear explosions using observations taken close to the source; then questions pertinent to seismic discrimination, e.g., the shape of the time function and amplitude-yield scaling, will improve our understanding of why the various discriminants are effective.

Recently Brian Stump and I put our two codes together. My code produces Green's functions for multilayered media close to the source with no approximation, having been designed specifically for this problem (Peppin, 1981, this report), and his does the linear inversion for the source. I have made four runs on the HANDLEY data and one with the PIPKIN data with the aim of addressing these questions: how stable are the results to large-scale perturbations in structure and what can we infer as true source motion?

The answer is mixed. Stump and Johnson (1981) have considered the effect of computing Green's functions for one structure with different sets of generalized rays, while here we consider the effects of distinctly different layer models. If we make a comparison based on the maximum values of the moment tensor, as presented in the previous section, then all structures shown in Figure 3.1 lead to the unequivocal characterization of the event as dominantly an explosion as found by Stump and Johnson. The models for the halfspace and for the source in the top layer (Figure 3.1) show a source which exhibits departure from spherical symmetry in the vertical direction; the Helmberger-Hadley and source-below-the-layer models in Figure 3.1 give values of $M(i,j)$ with the off-diagonal terms a twentieth or less of the on-diagonal terms and these are within a few percent of being identical in magnitude and shape. All of the models in Figure 3.1 lead to excellent fits of all 12 components of recorded acceleration on vertical, radial, and transverse components essentially throughout the whole record. As a result of these efforts I am convinced that one significant problem has been identified and solved. For the halfspace Green's function

LAYER MODELS

$$\begin{array}{c}
 \text{surface} \\
 \hline
 \alpha = 3.30 \quad \beta = 1.95 \\
 \rho = 2.70 \quad h = 1.3 \\
 *
 \end{array}$$

$$\begin{array}{c}
 \text{surface} \quad \downarrow \\
 \hline
 \alpha = 3.30 \quad \beta = 1.95 \\
 \rho = 2.60 \quad h = 1.3 \\
 *
 \end{array}
 \quad
 \begin{array}{c}
 \text{surface} \quad \downarrow \\
 \hline
 \alpha = 2.00 \quad \beta = 1.20 \quad \rho = 2.50 \quad h = 1.3 \\
 \rho = 2.67 \quad \beta = 2.21 \quad h = 1.3 \\
 *
 \end{array}
 \quad
 \begin{array}{c}
 \text{surface} \quad \downarrow \\
 \hline
 \alpha = 6.10 \quad \beta = 3.55 \\
 \rho = 2.70 \quad h = 1.3
 \end{array}$$

$$\begin{array}{c}
 \text{surface} \quad \downarrow \\
 \hline
 \alpha = 2.70 \quad \beta = 0.8 \quad \rho = 2.60 \quad h = 1.3 \\
 \alpha = 3.40 \quad \beta = 1.20 \quad \rho = 2.70 \quad .58 \text{ km} \\
 \alpha = 3.80 \quad \beta = 1.80 \quad \rho = 2.80 \quad .68 \text{ km} \\
 *
 \end{array}
 \quad
 \begin{array}{c}
 \text{surface} \quad \downarrow \\
 \hline
 \alpha = 4.40 \quad \beta = 2.50 \quad \rho = 2.82 \quad 1.2 \text{ km}
 \end{array}$$

Figure 3.1. Layer models used in source inversions of close-in accelerometer data.

or for the Green's function corresponding to a source in the top layer, the theoretical solutions predict significantly larger radial than vertical motion while the reverse is observed in the main P-wave of the explosion. This leads directly to the inference of an axial component in the source (the inversion has no other way to make the vertical component larger than the radial). Thus, this axial component is definitely an artifact, not part of the source. When any Green's function is used which gives the correct vertical/radial amplitude ratio, the axial component disappears, leaving a spherically-symmetric source. Consequently, I am now inclined to reject the non-explosive source component inferred by Peppin (1977), at least insofar as the generation of close-in body waves is concerned.

The problem is that the inferred time histories of the source are quite variable from model to model; compare the time histories inferred for the explosion part of the source presented in Figure 3.2. It appears that the method is such that the relative strengths of the $M(i,j)$ are insensitive to changes in the model, but the phase information, which controls the shape of the time history, is sensitive. That is to say: we can get some useful information with structure known only vaguely, but we can get much more if the structure is known to better precision. Stump and Johnson (1981) find elements in common with all of their inferred sources; however, their solutions appear unsatisfactory to me in that the most energetic part of the source lags 1.3 seconds behind the first impulse. More work is needed on this problem.

Once satisfactory inversions can be performed, our aim is to try and find elements of similarity in the source functions inferred under different circumstances with different explosions (do all need overshoot? do all need no overshoot?). We want to know whether a simple source is sufficient, or if spall phenomena contribute (here note the second arrival in the source function about 2 seconds after the event onset in Figure 3.2, corresponding to spall closure time for an event of this magnitude: Springer, 1974). The overshoot question has been studied using the same data set by Peppin (1977), Stump (1979), Helm-

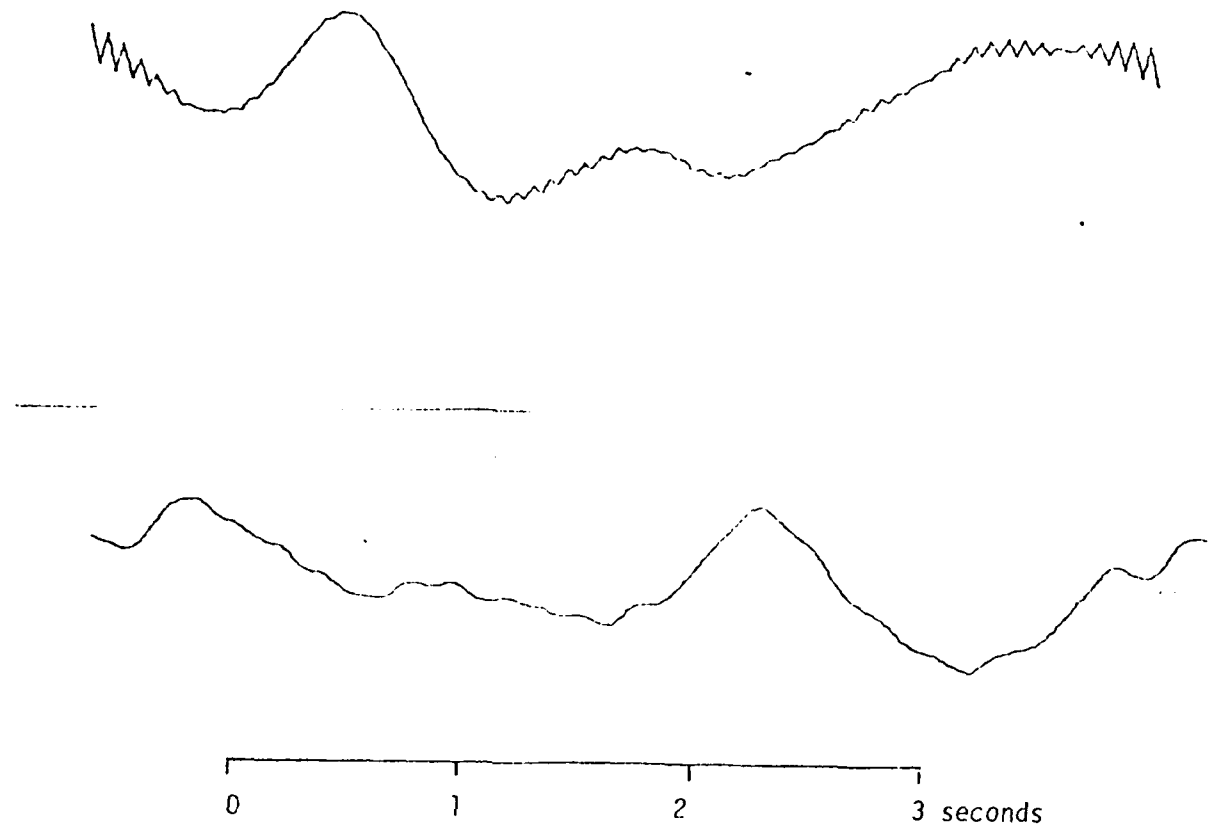


Figure 3.2. Inferred source motions for the explosive part of the source of the HANDLEY explosion. Top trace: for the model left-center in Figure 3.1; bottom trace: for the model right-center in Figure 3.1. Prominent secondary arrival seen on second trace as found by Stump (1979) for a half-space and by Stump and Johnson (1981) for the bottom layer model of Figure 3.1. Again the source appears to have overshoot; compare with Figure 2.2.

berger and Hadley (1981), and Stump and Johnson (1981) with diverging opinions. We must be prepared to accept that different source functions may be required to explain data at close-in versus teleseismic distances; and we must then assess the implications for seismic discrimination insofar as transferring inferences based on the one data set to the other.

REFERENCES CITED

Aki, K., 1967. Scaling law for seismic spectrum, *Jour. Geophys. Res.*, 72, 1217-1231.

Brune, J. N., 1970. Tectonic stress and spectra of seismic shear waves from earthquakes, *Jour. Geophys. Res.*, 75, 4997-5009.

Brune, J. N., 1971. Correction, *Jour. Geophys. Res.*, 76, 5002.

Chapman, C. H., 1978. A new method for computing synthetic seismograms, *Geophys. Jour. R. A. S.*, 54, 481-518.

Dey-Sarkar, S. K. and C. H. Chapman, 1978. A simple method for the computation of body-wave seismograms, *Bull. Seism. Soc. Am.*, 68, 1577-1594.

Hanks, T. C., 1981. The corner frequency shift, earthquake source models, and Q., *Bull. Seism. Soc. Am.*, submitted.

Helmburger, D. V. and D. M. Hadley, 1981. Seismic source functions and attenuation from local and teleseismic observations of the NTS events JORUM and HANDLEY, *Bull. Seism. Soc. Am.*, submitted for publication.

Peppin, W. A., 1974. The Cause of the Body Wave-Surface Wave Discriminant between Earthquakes and Underground Nuclear Explosions at Near-Regional Distances, Ph.D. Thesis, University of California, Berkeley.

Peppin, W. A., 1977. A near-regional explosion source model for tuff, *Geophys. Jour. R. A. S.*, 48, 331-349.

Peppin, W. A., 1981. Impulse solutions in a layered elastic medium: extended Lamb's problem [this report].

Peppin, W. A. and C. G. Bufe, 1980. Induced versus natural seismicity: search for a seismic discriminant, *Bull. Seism. Soc. Am.*, 70, 269-281.

Peppin, W. A. and M. R. Somerville, 1980. Spectral studies of earthquakes in the Mammoth Lakes, CA region, Nov 1979 to mid-July 1980, *EOS, Trans. Am. Geophys. Un.*, 61, 1041.

Peppin, W. A. and M. R. Somerville, 1981a. Mammoth-eastern Sierra earthquakes: further studies of wideband digital data, manuscript in preparation.

Somerville, M. R. and W. A. Peppin, 1980a. Recent seismicity patterns near Mammoth Lakes, California, *Earthquake Notes, Seism. Soc. Am.*, 50, 4-5.

Somerville, M. R. and W. A. Peppin, 1980b. Mammoth Lakes seismicity, past and present, *EOS, Trans. Am. Geophys. Un.*, 61, 1041.

Somerville, M. R. and W. A. Peppin, 1981. The validity of ML computed at close-in recording stations, manuscript in preparation.

Springer, D. L., 1974. Secondary sources of seismic waves from underground nu-

clear explosions, Bull. Seism. Soc. Am., 64, 581-594.

Stump, B. W., 1979. Investigation of Seismic Sources by the Linear Inversion of Seismograms, Ph.D. Thesis, University of California, Berkeley.

Stump, B. W. and L. R. Johnson, 1981. The effect of Green's functions on the determination of source mechanisms by the linear inversion of seismograms, manuscript in preparation.

Stump, B. W. and L. R. Johnson, 1977. The determination of source properties by the linear inversion of seismograms, Bull. Seism. Soc. Am., 67, 1489-1502.

[4] AMPLITUDE-YIELD SCALING RELATIONS OF
CHEMICAL EXPLOSIONS

William A. Peppin

Vaughn E. Culler

SUMMARY

Forty-six chemical explosions (24 to 515 pounds of C4 equivalent) were detonated above ground in a carefully-controlled experiment for seismic amplitude-yield scaling relations. Wideband (0.1 to 50 Hz) digital seismic data was recorded at four sites 1-4 km from various shotpoints. The seismic phases analyzed were a P-wave refracting along a shallow interface and the ground response to the air blast. Twenty-seven amplitude-yield scaling parameters were developed. Analysis of analog and spectral parameters shows the superiority of the latter in several respects: reduced dependence on source coupling and receiver conditions; greater ease of measurement standardization; improved objectivity in making a measurement. These results encourage the investigation of

spectral amplitude-yield scaling relations for the phase Pn at regional distance ranges.

INTRODUCTION

A sizeable literature exists on the subject of seismic amplitude-yield scaling (Carder and Cloud, 1959; Romney, 1959; Adams et al., 1961; Carder and Mickey, 1962; Kovach et al., 1963; Murphy and Lahoud, 1969; Springer and Hannon, 1973). However, summarized results (Murphy and Lahoud, 1969, Tables 2 and 3; Springer and Hannon, 1973) differ markedly with charge size, recording instrumentation, distance range, and source/receiver geology. At Lawrence Livermore Laboratory (LLL), it was felt that insufficient data was available in the relevant ranges of charge size and recording distance. Accordingly, we designed a seismic experiment which was conducted at the Site 300 testing facility near LLL for the purpose of developing a set of amplitude-yield scaling relations for the seismic amplitudes produced by above-ground chemical explosions.

Two facts establish the distinctive nature of our experiment as compared with previously-conducted ones. First, we collected some of the best seismic data ever taken for this purpose, and second, the design of the experiment was left to a seismologist within fairly broad constraints. Thus, we were able to obtain exactly the data we thought relevant, and because this data was wideband, three-component, velocity-flat (0.1 to 50 Hz; 12-bit resolution; X16 gain-range step), complete waveforms were available for all charges and recording distance ranges. A detailed description of the seismograph systems employed (DERs) is found in Peppin and Bufe (1980).

EXPERIMENTAL PROCEDURE AND RECORDS TAKEN

Three DERs were deployed 1 km SSE, 3 km SE, and 2.3 km SSW of the standard 802 shotpoint. These were given respective station names 845, Linac, and 858 (Figure 1). Three-component data was recorded at each site along with WWVB, an

absolute time standard. Horizontal components were rotated to radial (positive away) and transverse (positive to the right facing the source) components. Tests were made which showed independence of amplitude scaling with charge height above the ground (0 to 2 m) and with respect to asymmetric source modification (200 kg steel plates placed above, beside, and below 100-pound charges). For the amplitude-yield scaling series "KSG", each charge was fired 30 cm above the ground, the crater was refilled, and the next shot fired in the same spot to a precision of 4 m. Yields ranged from 24 to 515 pounds of C4 equivalent high explosive. In the source coupling series "KSF" identical 50-pound charges were fired in an X pattern over the 802 shotpoint with KSF4 at that site for reference (Figure 1).

Figure 2 shows a typical record as seen at the Linac site. On these and all other traces two phases are seen. The first motion is a seismic P-wave (longitudinal from the source, hereinafter called the "seismic wave") and the second is the ground response to the air blast (hereinafter the "acoustic wave"), which was fairly loud and sensible at this site. Figure 3 is a travel-time plot for the seismic wave. The velocity is 3.06 km/s and the intercept is consistent with a shallow refractor (typical at Site 300 is 60 m of loose material over Cenozoic sedimentary rocks). Thus, the arrival undoubtedly is a refraction along the top of the Cenozoic rocks, analogous to Pn observed regionally in the western U.S. In Figure 2 note the long-period undulations seen on each component preceding the event onset. These are the six-second microseisms, which demonstrates the system recording bandwidth. We identified no other seismic phase (such as S, Love, or Rayleigh waves). Peppin (1978) gives a complete presentation of all data recorded and a fuller discussion of these records.

DATA ANALYSIS

Analog measurements were made from the 400 data traces available from each component of seismic motion recorded. Amplitude spectra of the seismic and

acoustic phase (800 in all) were computed. The windows were 1.28 and 2.56 seconds, respectively, for these phases. A least-squares parabolic trend was removed and a 10% cosine taper applied at each end. Spectra were computed from the resulting traces. These were smoothed (3-point triangle window) and all were plotted after converting to ground motion by removing the system response. Identical processing was applied to the quiet segment preceding event onset so that an estimate of signal-to-noise ratio could be obtained as a guide for selecting appropriate passbands for amplitude-yield scaling. A sample spectrum appears in Figure 4; the others are found in Peppin (1978). All of the scaling measurements were made either from the preprocessed time trace (lower part of Figure 4) or from a spectral average of selected passbands in the amplitude spectrum of this trace (upper part of Figure 4). The analog measurements taken were the first quarter-cycle amplitude ("a") and first half-cycle amplitude ("b") measured directly off the time trace in Figure 4 (all are plotted the same height and the maximum amplitude in digital counts is given to the right of the time trace). Spectral scaling averages were determined by trial and error (at Linac the band 6-9 Hz was selected). "Better" passbands were those giving more uniform amplitude-yield scaling of the KSG series. We claim no completeness in our search for possible scaling parameters.

RESULTS

A. Source/Receiver Effects

The shots of the KSG series, all on 802, provided seismic records which overlaid site by site and component by component apart from a scaling of amplitudes with charge size. Thus, amplitude-yield scaling was precise to 5% and accurate to 10% for charges fired at that site and recorded at any of the three seismographs. The KSF series was designed to investigate variable source coupling (see Figure 1). In Table 1 we consider the ratio of a given measurement resulting from a shot off 802 to the same measurement resulting from the KSF4 shot on 802. Since all charges of this series had the same weight (50 pounds),

Table 1. Variability in source coupling by measurement type

Quantity Measured	Fraction of KSX4
Linac seismic, spectral	.753
845 seismic, spectral	.944
858 seismic, spectral	.609
Linac acoustic, spectral	1.03
845 acoustic, spectral	.99
858 acoustic, spectral	1.02
Linac seismic, analog	.652
845 seismic, analog	.635
858 seismic, analog	.762

a unit ratio implies identical source coupling. From Table 1 note the significant variation in source coupling (shots spaced only tens of m apart) and that spectral measurements are less source-dependent than analog ones. Note also that the acoustic wave shows no variation in source coupling, as is expected.

Table 2 provides a more detailed breakdown for each shot of the KSF series. In this table we present the ratios for the seismic analog and spectral measurements by shot. In column 4 we give the ratio we would expect and in column 5 we state why; for example, as KSF2 was placed on a dry sandstone outcrop, we would expect reduced motions near the source as compared with KSF4 fired in loosely-consolidated mud and gravel. This table shows that in each case except KSF8 the spectral measurement gave the more reasonable ratio relative to KSF4.

To pursue these effects further, we fired a shot at a completely different site 851 (see Figure 1). We were thus able to evaluate the amplitude-yield and distance scaling relations found from the KSG series. The spectral measurements at Linac, 845, and 858 gave an estimated yield of 94 ± 25 pounds and the analog measurements gave 50 ± 20 pounds for a 100-pound charge at Site 851. This reinforces the conclusion reached in the preceding paragraph.

Amplitude variations associated with receiver site are also clearly identifiable. The KSX series consisted of four charges detonated at 802, all of nearly equal weight. For the last two, KSX3 and KSX4, seismometers at Site 845 were moved 30 m into a concrete bunker dug into bedrock. In this high-velocity material we expect smaller amplitudes as noted by other investigators, and this effect is seen in Figure 5 for the KSX2 and KSX3 shots. The respective charge weights of these shots were 42 and 46 pounds of C4 equivalent. The ratios of the corresponding "a", "b", and spectral average measurements were 1.49, 2.22, and 1.63, showing that the spectral measurement is almost as good as "a" and better than "b" in terms of receiver-site independence.

B. Amplitude-Yield Scaling Relations

Table 2. Ratio of Shot X to KSF4

X	Seismic spectral	Seismic analog	expected	comments
KSF1	.98 ± .35	.52 ± .15	1	wet, dark mud like KSF4
KSF2	.48 ± .12	.46 ± .07	small	on dry sandstone
KSF3	.58 ± .05	.60 ± .05	small	near KSF2
KSF5	.85 ± .40	.72 ± .04	near 1	near edge of gully-mud
KSF6	.99 ± .46	.62 ± .14	1	similar to KSF1
KSF7	.83 ± .13	.80 ± .06	1	similar to KSF1
KSF8	1.27 ± .57	.95 ± .09	1	similar to KSF1

To determine amplitude-yield scaling relations, the KSG series was fired at Site 802. The charges used were 24, 40, 50, 72, 93, 112, 157, 217, 315, and 515 pounds of C4 equivalent high explosive. Regression of the log of the measurement made versus the log of the charge weight in pounds was performed at the three recording sites. Results appear in Table 3. Values of the yield scaling exponent "m" range from 0.6 to 1.0. Tables 2 and 3 of Murphy and Lahoud (1969) give slightly higher yield scaling exponents for displacement than for velocity (0.761 versus 0.646 in their Table 3). Here the spectral measurements represent displacement and the analog ones represent velocity. Our Table 3 gives 0.887 and 0.774 for the respective yield-scaling exponents. We might have expected the analog measurements to scale like Springer and Hannon's (1973) Pn data, which gave 0.63 (similar mode of wave propagation). As found by those authors, the peak frequency in the analog record scales weakly with yield, here varying by less than 25% over the whole range of charges fired. Undoubtedly the seismic waves suffer anelastic attenuation over these shallow paths.

DISCUSSION

The most significant result found is that spectral measurements, made on wideband digital systems, are superior to analog ones in several ways for amplitude-yield scaling. First, they are less dependent on variations in source coupling and receiver conditions; second, they permit measurement standardization; third, they appear more objective. We discuss each of these points below.

We should have expected less dependence on source/receiver effects in the spectral averages. The analog "a" and "b" measurements sample only the first arrival, a particular takeoff angle from the source. The spectral measurements included the whole group, thus samples a range of source takeoff angles. This should stabilize the measurement somewhat by the fact that it is an average. Similarly, the receiver response function, which is probably strongly frequency-dependent, will affect the measurement less if we average over a size-

Table 3. Yield-scaling exponents, $\log A = m \log Y + b$, where "A" is amplitude, "Y" is yield in pounds.

Measurement*	m	uncertainty**	b	uncertainty**
Linac seismic Z 6-9 Hz	.937	.0257	-4.00	.0524
Linac seismic R 6-9 Hz	.944	.0339	-3.81	.0691
Linac seismic T 6-9 Hz	.798	.0316	-3.79	.0645
Linac acoustic Z 3-7 Hz	.635	.0539	-2.54	.110
Linac acoustic R 3-7 Hz	.710	.0665	-2.86	.136
Linac acoustic T 3-7 Hz	.750	.0585	-2.61	.119
Linac seismic Z "a"	.782	.0339	1.41	.0691
Linac seismic Z "b"	.725	.0303	1.98	.0617
Linac seismic R "a"	.809	.0693	1.06	.147
Linac seismic R "b"	.881	.0360	1.46	.0735
858 seismic Z 4-9 Hz	.862	.0363	-4.00	.0728
858 seismic R 4-9 Hz	.880	.0315	-4.39	.132
858 seismic T 4-9 Hz	.798	.0606	-4.06	.135
858 acoustic Z 1.5-3 Hz	.735	.0440	-2.87	.0883
858 acoustic R 1.5-3 Hz	.925	.0791	-3.20	.159
858 acoustic T 1.5-3 Hz	.908	.0646	-3.36	.130
858 seismic Z "a"	.815	.0954	1.31	.192
858 seismic Z "b"	.725	.0575	1.89	.115
845 seismic Z 8-12 Hz	.695	.0483	-3.06	.0985
845 seismic R 9-12 Hz	.820	.0661	-2.76	.135
845 seismic T 9-12 Hz	1.25	.189	-3.73	.386
845 acoustic Z 5-10 Hz	.847	.0738	-2.84	.150
845 acoustic R 5-10 Hz	.659	.0868	-2.46	.177
845 seismic Z "a"	.608	.0441	2.46	.0900
845 seismic Z "b"	.590	.0438	2.96	.0892
845 seismic R "a"	.962	.0578	1.65	.118
845 seismic R "b"	.944	.0449	2.23	.0915

*spectral measurements include pass band of average used. In this case, the amplitude is in units of micron-s. Analog "a" and "b" measurements are in arbitrary units.

**uncertainties of slopes and intercepts estimated from standard regression formulas.

able pass band to smooth the variations.

Measurement standardization is made possible by presenting each spectrum as in Figures 4 and 5, with ordinate in terms of absolute ground motion. This permits the mixing of data recorded on unmatched systems. It also eliminates the problem that analog measurements, taken from a wideband signal viewed through a narrow-band system, cannot be related simply to absolute ground motion; thus, analog measurements from different systems cannot be compared directly as can absolute spectral ones.

Objectivity is aided in computing spectral averages because it bypasses the variation in signal character seen on analog traces by discarding the phase information. In Figure 5 note the large variation in signal character, and in particular the large difference between the ratio of "a" to "b"; however, a spectral average basically measures the power in the whole wave group, which should be a more stable measure of yield than measuring a particular phase amplitude, whose character may change markedly in different source regions as is seen for NTS explosions.

Finally, note that the wave group analyzed was a refracting phase whose mode of propagation is evidently similar to the Pn phase. Thus, our results suggest that Springer and Hannon's (1973) amplitude-yield scaling relations can profitably be extended using spectral averages.

ACKNOWLEDGMENTS

This work was performed with the assistance and cooperation of Maylin Dittmore, Lloyd Guyman, Murray Kavanaugh, Jim Hannon, and Marv Denny of Lawrence Livermore Laboratory; it was supported by Grant No. 9473703 from LLL. The digital event recorders were designed and built under grants from the Advanced Research Projects Agency monitored by the Air Force Office of Scientific Research, Contract Numbers F44620-72-C-0069 and F49620-77-C-0070.

REFERENCES CITED

Adams, W. M., Preston, R. G., Flanders, P. L., Sachs, D. C. & Perret, W. R., 1961. Summary report of strong-motion measurements, underground nuclear detonations, *J. geophys. Res.*, 66, 903-942.

Carder, D. S. & Cloud, W. K., 1959. Surface motion from large underground explosions, *J. geophys. Res.*, 64, 1471-1487.

Carder, D. S. & Mickey, W. V., 1962. Ground effects from underground explosions, *Bull. seism. Soc. Am.*, 52, 67-75.

Kovach, R. L., Lehner, F. & Miller, R., 1963. Experimental ground amplitudes from small surface explosions, *Geoph.*, 28, 193-798.

Murphy, J. R. & Lahoud, J. A., 1969. Analysis of seismic peak amplitudes from underground nuclear explosions, *Bull. seism. Soc. Am.*, 59, 2325-2341.

Peppin, W. A., 1978. Yield Determination of Chemical Explosions by Seismic Measurements, Final Report to Lawrence Livermore Laboratory, Z-Division, Account No. 9473703.

Peppin, W. A. & Bufe, C. G., 1980. Induced versus natural earthquakes: search for a seismic discriminant, *Bull. seism. Soc. Am.*, 70, 269-281.

Romney, C., 1959. Amplitudes of seismic body waves from underground nuclear explosions, *G. geophys. Res.*, 64, 1489-1498.

Springer, D. L. & Hannon, W. J., 1973. Amplitude-yield scaling for underground explosions, *Bull. seism. Soc. Am.*, 63, 477-500.

FIGURE CAPTIONS

Figure 1. Left: plan view of standard 802 shotpoint, special 851 shotpoint, and the three seismic recording sites described herein. Right: plan view of shot locations in the KSF source coupling experiment. The shotpoint numbered "4" is the standard 802 shotpoint.

Figure 2. Three-component records of Shot KSG7 as recorded at the Linac site. Traces from top to bottom: WWVB time code, vertical, radial, and transverse system output, essentially ground velocity. All seismic traces are scaled to the same plot amplitude; this maximum corresponds to the amplitude given left of each seismic trace in digital counts.

Figure 3. Travel-time curve for the seismic wave as recorded for all shots and all distance ranges. A least-squares line for travel-time "T" in seconds versus distance "X" in km gives $T = 0.327X + 0.160$.

Figure 4. After windowing, detrending, and tapering (see text), the

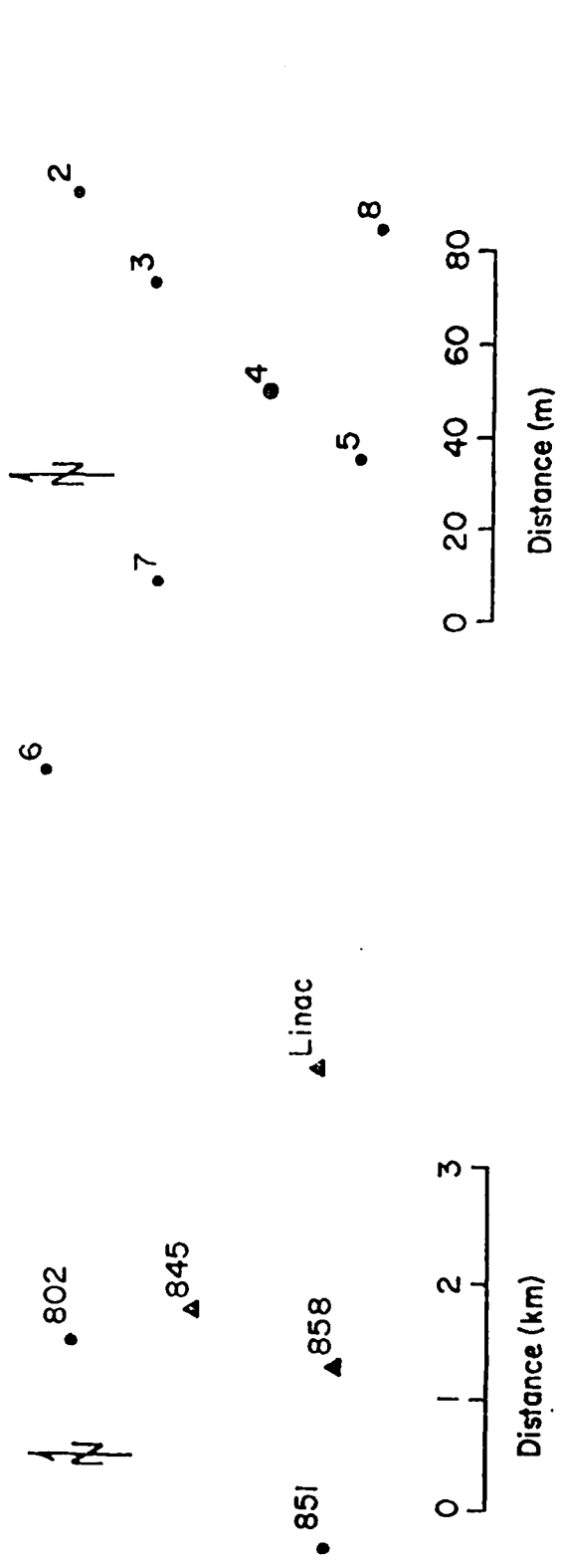


Fig 1

Fig 1

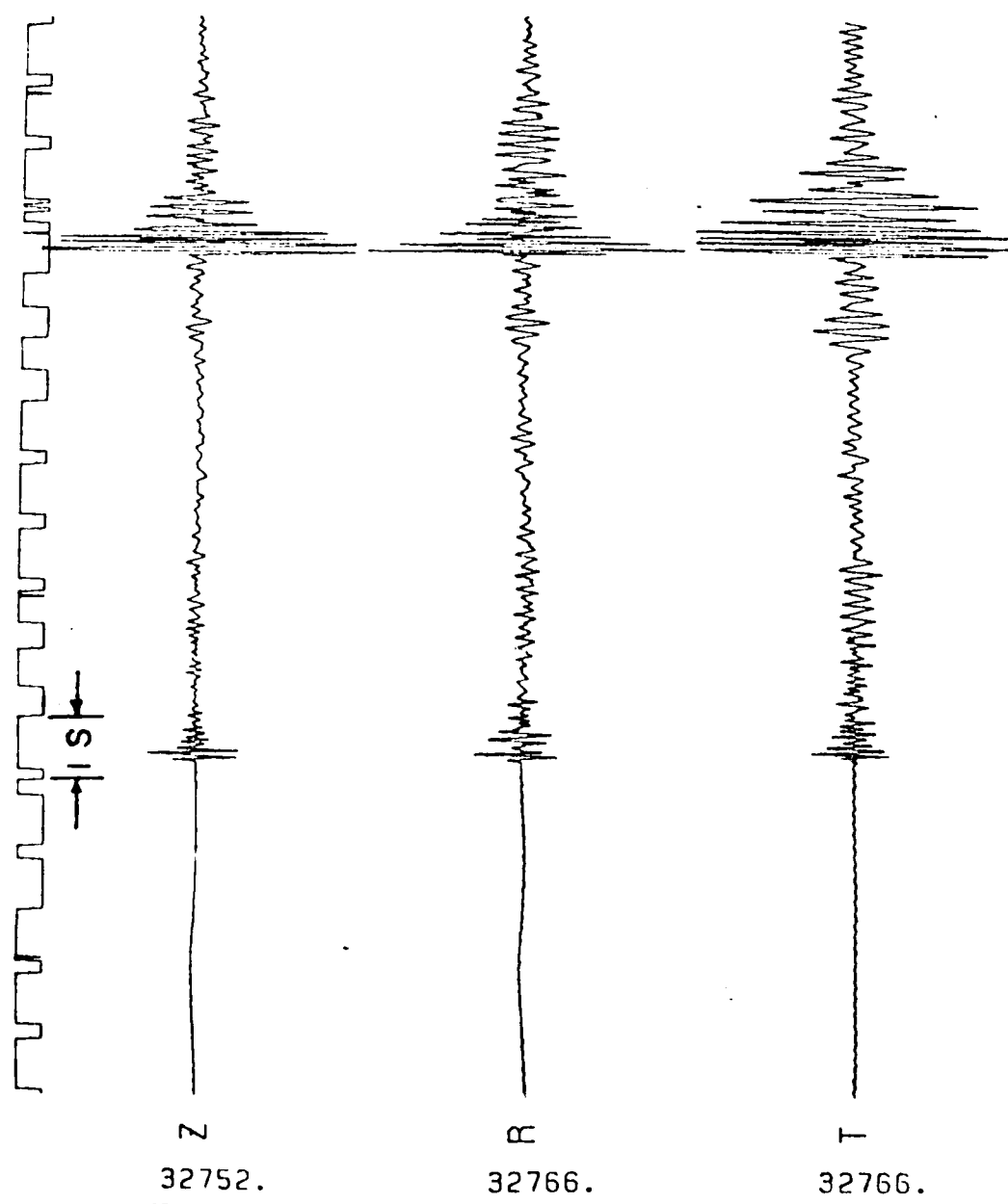


Fig 2

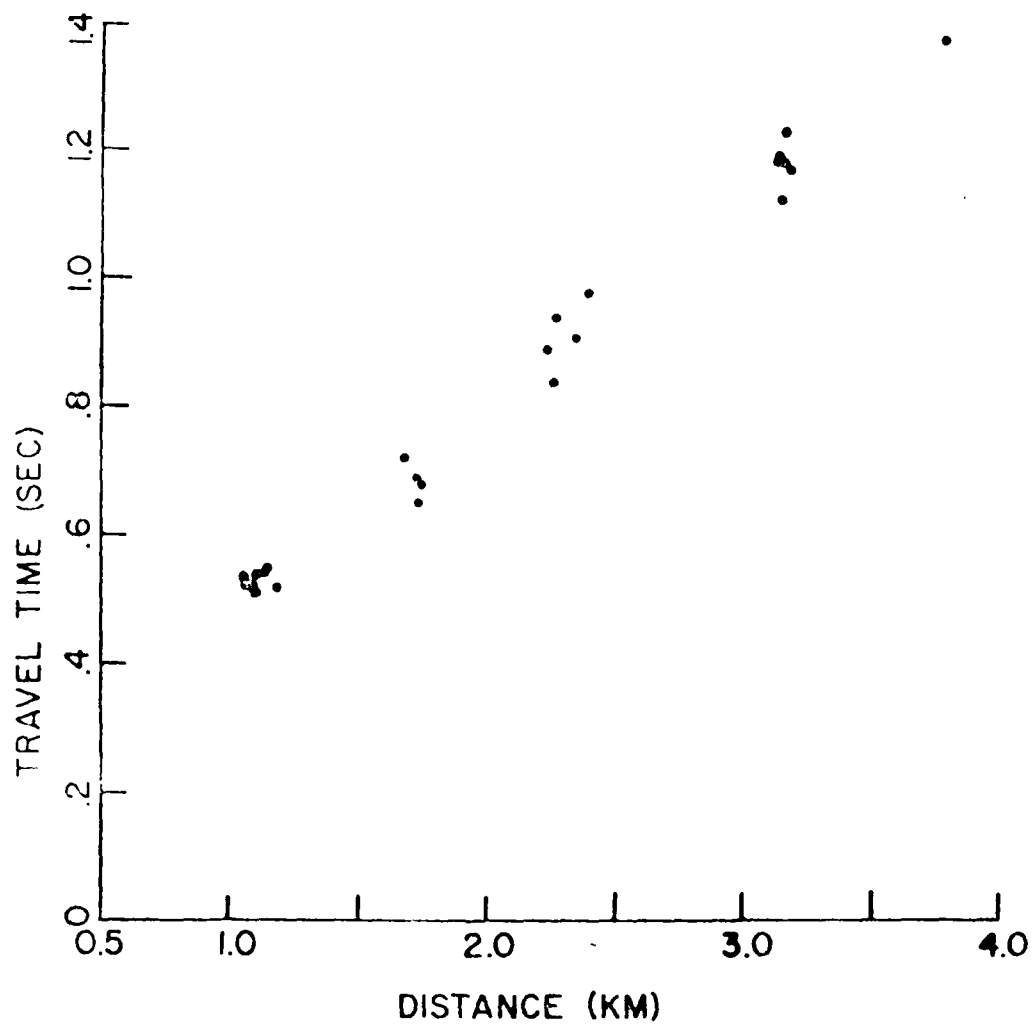


Fig 3

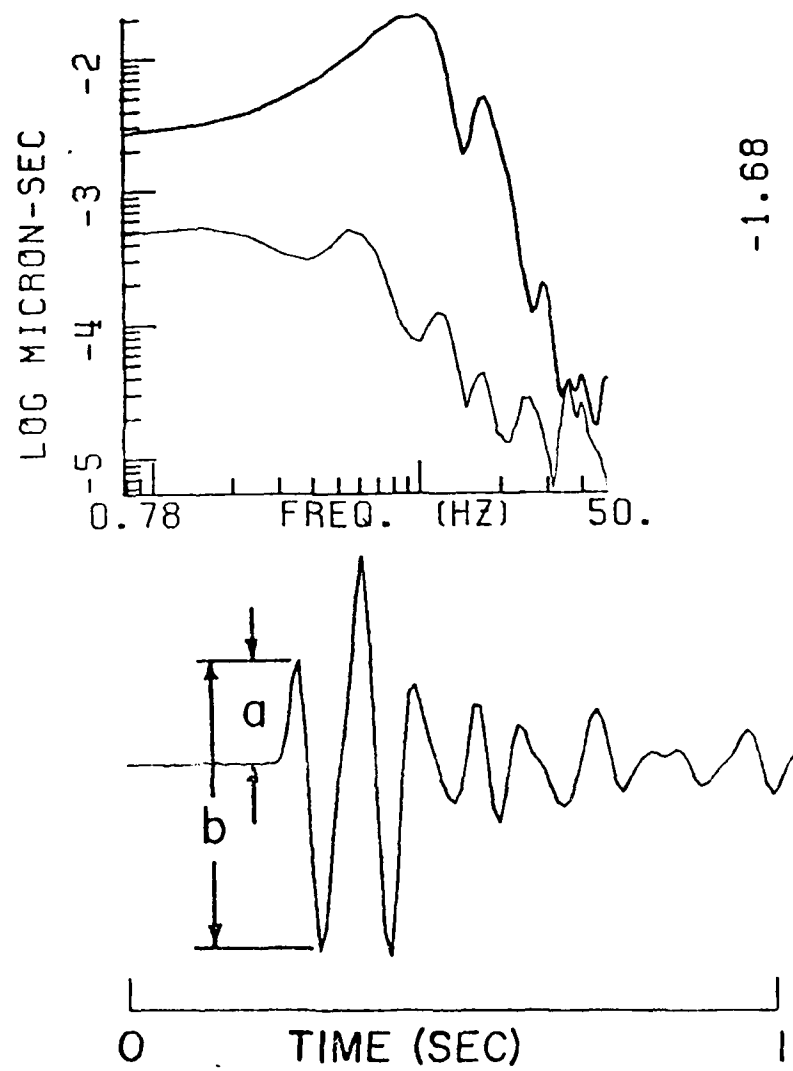


Fig 4

Z 9738.
KSG7LIN.DA

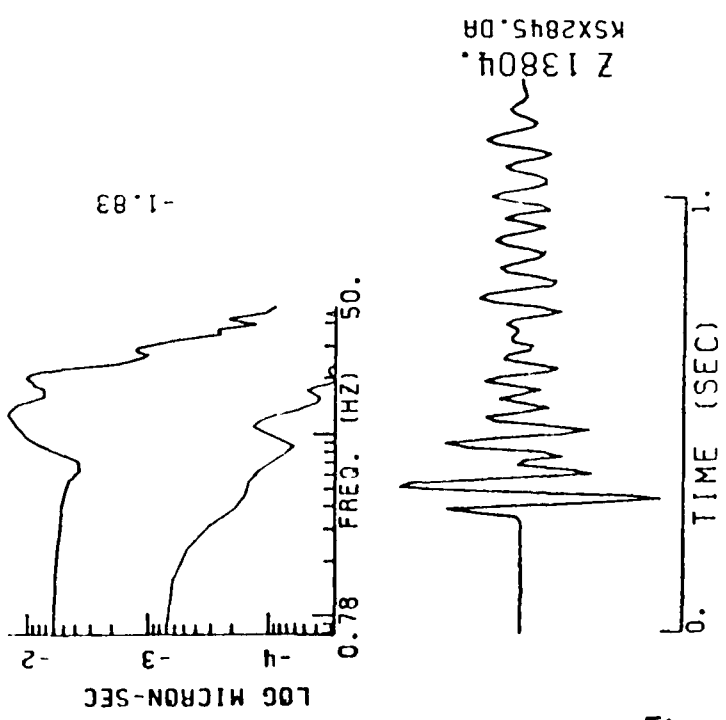
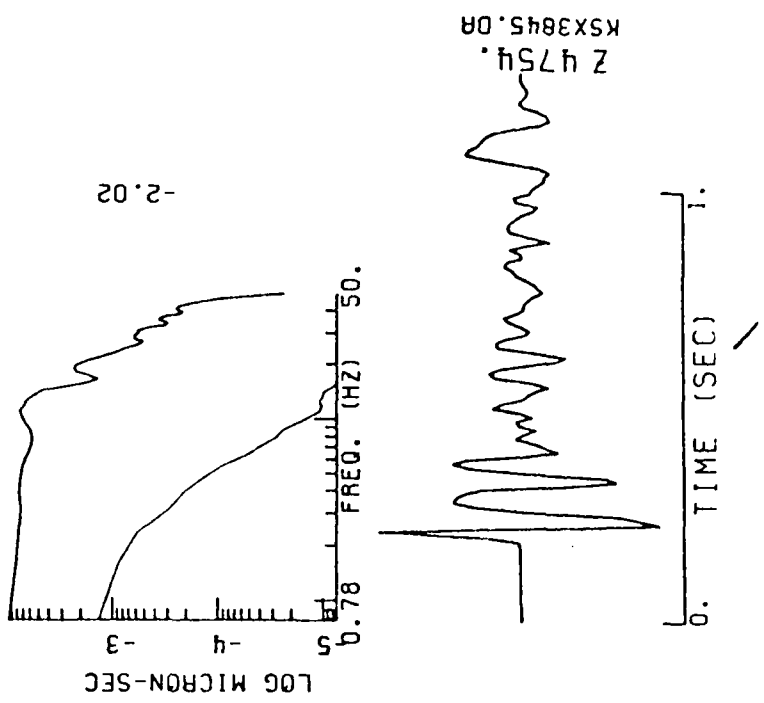


Fig 5

vertical-component seismic phase from Figure 2 looks like the lower trace given (maximum amplitude in digital counts right of the trace). Above in bold is the Fourier amplitude spectrum after smoothing and correction to ground motion. The thin trace is the spectrum of record segment preceding event onset which has been processed the same way. The analog measurements "a" and "b" were measured as indicated here.

Figure 5. Same format as Figure 4, but as recorded for KSX2 (left) and KSX3 (right). The recording site for KSX2 was in loose, wet soil, and for KSX3 it was 30 m SE inside a concrete bunker set in bedrock.

[5] THE PN-RAYLEIGH AND ANOTHER NEAR-REGIONAL DISCRIMINANT

WILLIAM A. PEPPIN

SUMMARY. A near-regional seismic discriminant between earthquakes and underground explosions, first proposed by McEvilly and Peppin (1972) and based on a comparison of Pn and Rayleigh amplitudes, fails for a selection of events recorded at a new wideband station Jamestown, 450 km from Nevada Test Site. The same events can be correctly identified in 49 out of 60 cases if a comparison is made between the amplitude ratios of envelopes drawn around the Sg and Pg phases. This discriminant, similar to some of the earliest proposed, has the advantages of: potential extension to small (Richter magnitude ML .1t. 3.0) events at regional distances; ease of application; ready explanation of why it is effective; and probable weak dependence on earthquake focal mechanism.

INTRODUCTION

McEvilly and Peppin (1972) and Peppin and McEvilly (1974) found a successful seismic discriminant between small (ML .ge. 3.6) near-regional explosions and earthquakes. Using wideband (0.04 to 10 hz) vertical data recorded at Berkeley (BRK), Mina (MNV), Kanab (KAN), Landers (LAN) and Elko (ELK), 200 to 550 km from Nevada Test Site (NTS), 0.5 to 5-Hz Pn amplitude was plotted versus 0.02 to 0.1-Hz Rayleigh amplitude for explosions and earthquakes (many on NTS) with satisfactory separation of explosions from other events at all stations and all magnitudes studied (3.5 .le. ML .le. 6.3). In 1975 the University of California at Berkeley began operation of another wideband system at Jamestown (JAS) in the Sierra foothills. An attempt was made to check the effectiveness of the discriminant based on new (1975-1979) data in view of recent interest in regional seismic discrimination. I present results of the analysis for this and one other discriminant in this paper.

DATA

In Figure 1 is presented the instrument characteristics for data traces recorded at JAS. Multigain recording of the 4 data channels is on compensated, 40-percent deviated, FM analog magnetic tape. Data channels consist of a high-gain short-period Benioff vertical (SPZ), a wideband velocity system (0.025-10 Hz, BBV), and a wideband displacement system (capacitance transducer on the same pendulum). The high-gain and low-gain displacement outputs, DHG and DLG, are separated by 46 dB. The DLG channel is such that a one megaton explosion on NTS records near full-scale. Therefore, essentially any seismic event in California or Nevada with 3.0 .le. ML .le. 6.5 is well-recorded by the system on at least one data trace, providing if anything superior data to that used in the earlier studies. Analog layouts of filtered Pn (0.5 to 5 Hz, 48 dB/octave) and Rayleigh waves (0.02 to 0.1 Hz, 48 dB/octave) were prepared using an experimental procedure identical to that employed by McEvilly and Peppin (1972) and Peppin and McEvilly (1974).

SELECTION OF EVENTS FOR ANALYSIS

We face the frustration that no earthquake has occurred on NTS between 1975 and 1979 that would be suitable for direct comparison with explosions as done by Peppin and McEvilly (1974). Thus, following McEvilly and Peppin (1972), we take earthquakes at an approximate distance to JAS equal to the distance to NTS. Events selected are presented in Tables 1 and 2.

RESULTS: PN VERSUS RAYLEIGH DISCRIMINANT

Figure 2 is a plot of Pn versus Rayleigh amplitudes for the events given in Table 1. DHG and SPZ were taken as the standards for measuring Rayleigh and Pn amplitudes, respectively. Due to a wide range of amplitudes, empirical relations were developed between these standards and the other traces available:

$$\text{DHG} = \text{BBV}/(11.1 \pm 2.6) \\ \text{for Rayleigh waves (22 common events)}$$

$$\text{SPZ} = \text{BBV}(17.1 \pm 6) \\ \text{for Pn (15 common events)}$$

$$\text{SPZ} = \text{DHG}(34.3 \pm 12) \\ \text{for Pn (8 common events)}$$

Using these and the static gain factor of 200 between DHG and DLG, all Rayleigh amplitudes were converted to DHG and all Pn amplitudes were converted to SPZ, the numbers given in Table 1. Starred readings in this table were converted to the standard ones using the above empirical relations. Figure 3 shows the locations of JAS, NTS, and the earthquakes used in this study.

RESULTS: PG VERSUS SG ENVELOPE

The appearance of the records under considerations suggested another promising discriminant. In Figure 4 an envelope was drawn around the Pg and Sg phases on visicorder playouts. The amplitudes A and B were read and the ratio B/A formed. The SPZ channel was selected as the standard one since it recorded events of smallest magnitude. Empirical relations were developed between SPZ and the other channels as follows:

$$\text{SPZ} = \text{DHG}(17.6 \pm 7.8) \\ \text{for P, 23 common events}$$

Table 1. Amplitude data for the Pn-Rayleigh discrimination, measured in arbitrary units.

IDENTIFIER	EVENT NO	PN AMP	RAYLEIGH AMP	COMMENTS
0948				
975 JUN 27	0727	1	32	88* COLLAPSE
975 JUN 28	0948	2	28	77* COLLAPSE
975 JUL 01	0451	3	18	30 COLLAPSE
975 JUL 01	1814	4	40	248* COLLAPSE
975 SEP 06	1700	5	104	18 EXPLOSION
975 OCT 24	1712	6	323*	57 EXPLOSION
975 OCT 28	1430	7	17000*	16800 EXPLOSION
975 NOV 20	1500	8	2450	3440 EXPLOSION
975 NOV 26	1530	9	104	47 EXPLOSION
976 JAN 03	1915	10	6420*	25600 EXPLOSION
976 JAN 04	0118	11	42	76 COLLAPSE
976 JAN 24	1616	12	18+	60+ COLLAPSE
976 JAN 17	2140	13	22	40 COLLAPSE
976 FEB 04	1420	14	1275*	1160* EXPLOSION
976 FEB 04	1440	15	1600	1309* EXPLOSION
976 FEB 12	1445	16	5900	5525 EXPLOSION
976 FEB 14	1130	17	3434*	24000 EXPLOSION
976 FEB 19	1701	18	28	10 EARTHQUAKE, AZ 125, MAG 4.3, D 332
976 MAR 09	1400	19	3486*	6400 EXPLOSION
976 MAR 14	1430	20	7480*	17600 EXPLOSION
976 MAR 14	1525	21	56	200 COLLAPSE
976 MAY 12	1950	22	144	88 EXPLOSION
976 JUN 07	0035	23	2	44 EARTHQUAKE, AZ 115, MAG 4.1, D 392
976 AUG 26	1430	24	408	248 EXPLOSION
976 DEC 08	1450	25	136	112 EXPLOSION
976 DEC 21	1509	26	104	1 EXPLOSION
977 JAN 13	0719	27	74	10* EARTHQUAKE, AZ 165, MAG 3.8, D 370
977 JAN 13	2029	28	44+	28 EARTHQUAKE, AZ 340, MAG 3.7, D 377
977 FEB 16	1753	29	96	22* EXPLOSION
977 AUG 04	1640	30	328	440 EXPLOSION
977 AUG 12	0220	31	224	180 EARTHQUAKE, AZ 165, MAG 4.8, D 421
977 AUG 19	1755	32	744	1386* EXPLOSION
977 SEP 15	1436	33	72	11* EXPLOSION
977 OCT 26	1415	34	66	76 EXPLOSION
977 NOV 10	0235	35	48+	15 EARTHQUAKE, AZ 145, MAG 4.0, D 340
977 NOV 17	1930	36	88	26 EXPLOSION
977 DEC 14	1530	37	3264*	1400 EXPLOSION
978 FEB 14	0435	38	328	256 EARTHQUAKE, AZ 075, MAG 4.8, D 365
978 MAY 23	0547	39	104	74 EARTHQUAKE, AZ 045, MAG 4.6, D 434
978 JUN 16	0421	40	64	15 EARTHQUAKE, AZ 165, MAG 4.3, D 320
978 AUG 01	0902	41	56	700 EARTHQUAKE, AZ 345, MAG 4.6, D 397
978 AUG 01	0947	42	30	528 EARTHQUAKE, AZ 345, MAG 4.5, D 397
978 AUG 01	1026	43	44	58 EARTHQUAKE, AZ 345, MAG 4.2, D 397
978 AUG 31	1400	44	5440*	1400 EXPLOSION
978 AUG 31	2356	45	42	86 COLLAPSE
978 NOV 02	1525	46	168	55 EXPLOSION
979 JAN 06	0120	47	36+	39 EARTHQUAKE, AZ 75, MAG 4.2, D 365
979 JAN 24	1800	48	200	66 * EXPLOSION

- READINGS BY CONVERSION TO STANDARD ONES (SEE TEXT)

- POOR READINGS

SPZ = DHG(13.6 ± 6.1)
for S, 23 common events

SPZ = BBV(13.9 ± 4.2)
for P, 14 common events

SPZ = BBV(13.0 ± 4.5)
for S, 24 common events.

In Table 2 we present the events used, the P amplitude, and the S to P ratio which is to form the discriminant. Starred readings in the Table denote conversions to the standard ones using (2). In Figure 5 is plotted S to P ratio versus log of P amplitude.

DISCUSSION: PN VERSUS RAYLEIGH DISCRIMINANT

Figure 2 documents the complete failure of the Pn versus Rayleigh discriminant for the JAS data set. Note in Figure 3 that BRK, JAS, and MNV are all located NW of the test site. Discrimination based on Pn and Rayleigh waves was very effective at BRK and MNV, but nonexistent at JAS between these two stations. As Peppin (1974) noted: the theoretical basis for such a discriminant hasn't been unequivocally established, so perhaps the result should have been expected.

DISCUSSION: PG VERSUS SG ENVELOPE DISCRIMINANT

The discriminant shown in Figure 5, similar to those based on the Lg phase, appears to have promise and could certainly be refined following procedures adopted by, for example, Murphy and Lahoud (1975). The dashed line in Figure 5 is a decision line (explosions below and earthquakes above with one exception, #28 in Table 2). The dot-dashed lines are based on estimated uncertainties of 20 events for which the ratio could be obtained on all three channels. Thus, events inside the band delimited by these lines are not identified with certainty. Of 60 events, 11 are unresolved and one earthquake is misidentified as an explosion. Collapses, which overlap the two populations, are presumably distinctive enough as to cause no problem for identification by other methods. No

Table 2. Data for the discriminant based on the ratio of S to P envelope amplitude.

Identifier	Event No.	P Displacement	S/P ratio	Comments
976 JUN 27	0727	1	15.	1.12* COLLAPSE
976 JUN 28	0948	2	14.	1.10* COLLAPSE
976 JUL 01	0451	3	12.	1.05 COLLAPSE
976 JUL 01	1814	4	39.	2.68 COLLAPSE
976 SEP 06	1700	5	22.	1.11 EXPLOSION
976 OCT 24	1712	6	67.	1.24 EXPLOSION
976 OCT 28	1430	7	76.	0.32 EXPLOSION
976 NOV 18	1530	8	12.	1.75 EXPLOSION
976 NOV 20	1500	9	1400.	0.50 EXPLOSION
976 NOV 26	1530	10	36.	1.47 EXPLOSION
976 JAN 03	1915	11	4200.	0.48 EXPLOSION
976 JAN 04	0118	12	13.	1.26 COLLAPSE
976 JAN 04	1616	13	8.	2.40 COLLAPSE
976 JAN 18	0720	14	14.	1.75 COLLAPSE
976 JAN 21	1840	15	9.	2.11 COLLAPSE
976 FEB 03	0015	16	8.	1.33 COLLAPSE
976 FEB 04	1420	17	480.	1.20 EXPLOSION
976 FEB 04	1440	18	416.	1.58 EXPLOSION
976 FEB 12	1445	19	1400.	0.71 EXPLOSION
976 FEB 14	1130	20	3800.	0.53 EXPLOSION
976 FEB 19	1701	21	15.	3.97 EARTHQUAKE, AZ 125, MAG 4.3, D 332
976 FEB 26	1450	22	8.	1.28 EXPLOSION
976 MAR 09	1400	23	2000.	1.33 EXPLOSION
976 MAR 09	1655	24	16.	1.26 COLLAPSE
976 MAR 14	1450	25	4400.	0.45 EXPLOSION
976 MAR 14	1525	26	30.	1.22* COLLAPSE
976 MAY 12	1900	27	53.	1.18 EXPLOSION
976 JUN 07	0035	28	13.	1.77 EARTHQUAKE, AZ 115, MAG 4.1, D 392
976 JUN 19	1025	29	7.	1.71 EXPLOSION
976 AUG 22	1014	30	6.	2.26 EARTHQUAKE, AZ 075, MAG 4.0, D 365
976 AUG 26	1430	31	140.	1.47 EXPLOSION
976 DEC 08	1450	32	69.	1.12 EXPLOSION
976 DEC 21	1509	33	31.	0.98 EXPLOSION
977 JAN 13	0719	34	13.	2.00* EARTHQUAKE, AZ 165, MAG 3.8, D 370
977 JAN 13	2009	35	6.	3.96 EARTHQUAKE, AZ 340, MAG 3.7, D 377
977 FEB 16	1753	36	25.	1.25 EXPLOSION
977 MAY 31	1640	37	3.	3.67 EARTHQUAKE, AZ 330, MAG 3.7, D 330
977 AUG 04	1640	38	130.	0.86* EXPLOSION
977 AUG 12	0220	39	40.	3.73 EARTHQUAKE, AZ 165, MAG 4.8, D 421
977 AUG 19	1755	40	471.	1.27* EXPLOSION
977 SEP 15	1436	41	18.	1.28 EXPLOSION
977 OCT 26	1415	42	31.	1.54 EXPLOSION
977 NOV 10	0236	43	14.	3.28 EARTHQUAKE, AZ 145, MAG 4.0, D 340
977 NOV 17	1930	44	49.	1.18 EXPLOSION
977 DEC 14	1530	45	495.	1.13 EXPLOSION
978 FEB 14	0435	46	16.	2.96 EARTHQUAKE, AZ 075, MAG 4.8, D 365
978 MAY 23	0547	47	20.	4.45 EARTHQUAKE, AZ 045, MAG 4.6, D 434
978 JUN 16	0421	48	64.	2.17 EARTHQUAKE, AZ 165, MAG 4.3, D 370
978 JUL 07	1400	49	24.	1.16* EXPLOSION
978 JUL 29	2232	50	52.	2.08 EARTHQUAKE, AZ 058, MAG 4.0, D 380
978 AUG 01	0902	51	40.	3.87 EARTHQUAKE, AZ 345, MAG 4.6, D 397
978 AUG 01	0947	52	24.	5.27 EARTHQUAKE, AZ 345, MAG 4.5, D 397
978 AUG 01	1026	53	16.	2.21 EARTHQUAKE, AZ 345, MAG 4.2, D 397
978 AUG 31	1400	54	1500.	0.67 EXPLOSION
978 AUG 31	2356	55	21.	0.50 COLLAPSE
978 NOV 02	1525	56	32.	0.71 EXPLOSION
979 JAN 06	0120	57	16.	2.55 EARTHQUAKE, AZ 75, MAG 4.2, D 365
979 JAN 24	1800	58	25.	1.39 EXPLOSION
979 FEB 22	0716	59	8.	4.16 EARTHQUAKE, AZ 005, MAG 3.5, D 210
979 FEB 22	1557	60	700.	2.54 EARTHQUAKE, AZ 005, MAG 5.0, D 210

-BY CONVERSION TO JAMESTOWN SHORT PERIOD (SEE TEXT)

explosion is misidentified as an earthquake.

The following can be cited as distinct advantages of such a discriminant: (1) it is effective to magnitudes as small as can be seen on a high-gain, short-period instrument, i.e., less than ML 3.0 at regional distances; (2) it is simple to apply; (3) it is reasonably easy to find an explanation as to why it is effective; and (4) the quantity measured is a ratio that probably depends weakly on focal mechanism (many takeoff angles at the source contribute to Pg and Sg), hence can be carried over directly to other regions without need of a regional calibration. The discriminant should work because envelope amplitudes should be a measure of S energy and P energy leaving the source. As a shear dislocation releases about 10 times more energy in S than in P (Haskell, 1964), it is expected to have significantly higher S to P ratio than an explosion in a plot like Figure 5. This is the same reason given by Douglas et al. (1971) for effectiveness of the Ms:mb discriminant.

CONCLUSIONS

The results presented here imply that the Pn versus Rayleigh discriminant between explosions and earthquakes, proposed first by McEvilly and Peppin (1972), can no longer be considered effective. A discriminant based on relative excitation of the Pg and Sg phases is fairly effective, could doubtless be refined, and holds the promise of extension to the lowest magnitudes possible (less than ML 3.0 at regional distances). However, this analysis emphasizes the need for theoretical understanding in some depth before empirical seismic discriminants can be used confidently.

ACKNOWLEDGMENTS

This research was supported by the Advanced Research Projects Agency of the Department of Defense and was monitored by the Air Force Office of Scientific Research under Contract No. F49620-77-C-0070. The Seismographic Station of the

University of California at Berkeley provided access to their tape library which is the data source for this paper.

REFERENCES

Haskell, N. A., 1964. Total energy and energy spectral density of elastic wave radiation from propagating faults, Bull. seism. Soc. Am., 54, 1811-1842.

McEvilly, T. V. & Peppin, W. A., 1972. Source characteristics of earthquakes, explosions, and afterevents, Geophys. J. R. astr. Soc., 31, 67-82.

Murphy, J. R. & Lahoud, J. A., 1975. Analysis of Near-Field Ground Motion Spectra from Explosions and Earthquakes, ARPA Technical Report from Computer Science Corporation, February.

Peppin, W. A., 1974. The cause of the body wave-surface wave discriminant between earthquakes and underground nuclear explosions at near-regional distances, PhD thesis, University of California at Berkeley.

Peppin, W. A. & McEvilly, T. V., 1974. Discrimination among small magnitude events on Nevada Test Site, Geophys. J. R. astr. Soc., 37, 227-244.

FIGURE CAPTIONS

Figure 1. Instrument characteristics of the data traces recorded on analog magnetic tape for the Jamestown wideband system. Curves 1 and 2: DHG and DLG; 3: BBV; 4: SPZ.

Figure 2. Log of Rayleigh wave amplitude versus log of Pn amplitude. The larger symbols denote standard measurements (see text) and the smaller ones correspond to any of the starred readings from Table 1. Number beside each symbol is an event number from Table 1. "Collapse" events are the hole collapses following many of the explosions on NTS.

Figure 3. Map view of the California-Nevada region showing locations of wideband station JAS and NTS (triangles), and the earthquakes used in this study (numbers correspond to table 2).

Figure 4. Sample of data to show derivation of the Sg-Pg envelope discriminant. Envelopes are drawn about the Pg and Sg phases by hand, and the am-

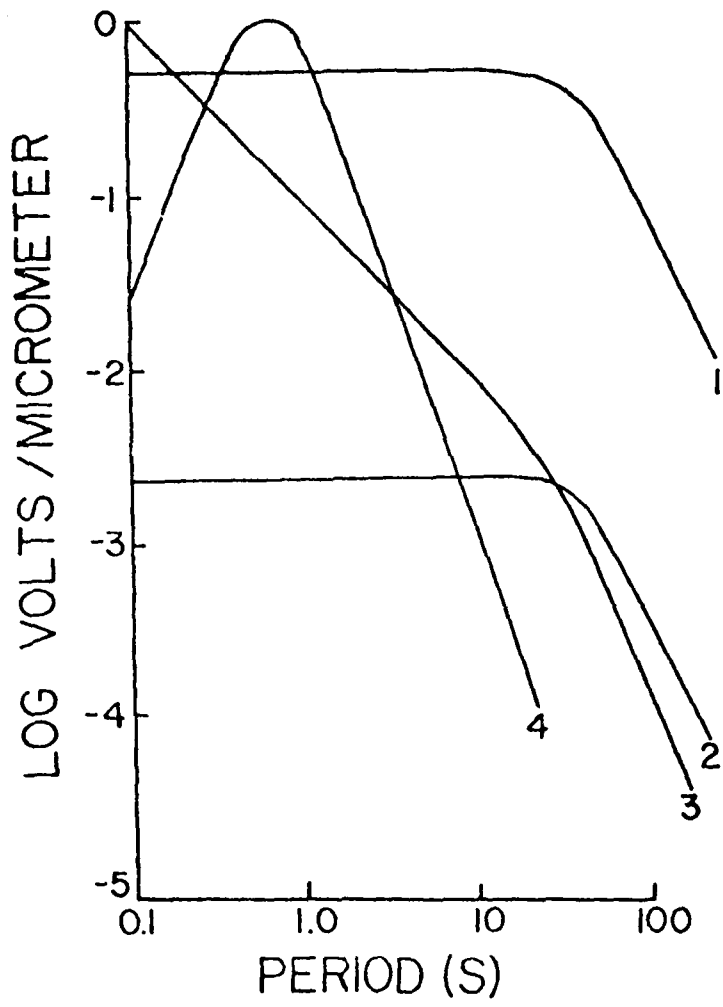


Fig 1

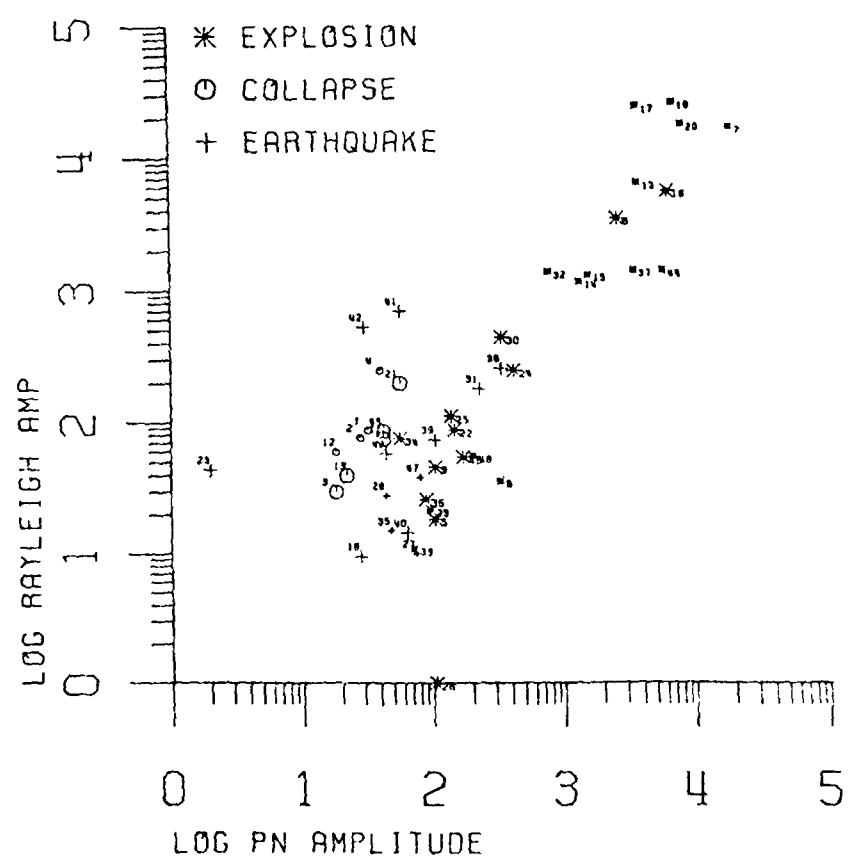


Fig 2

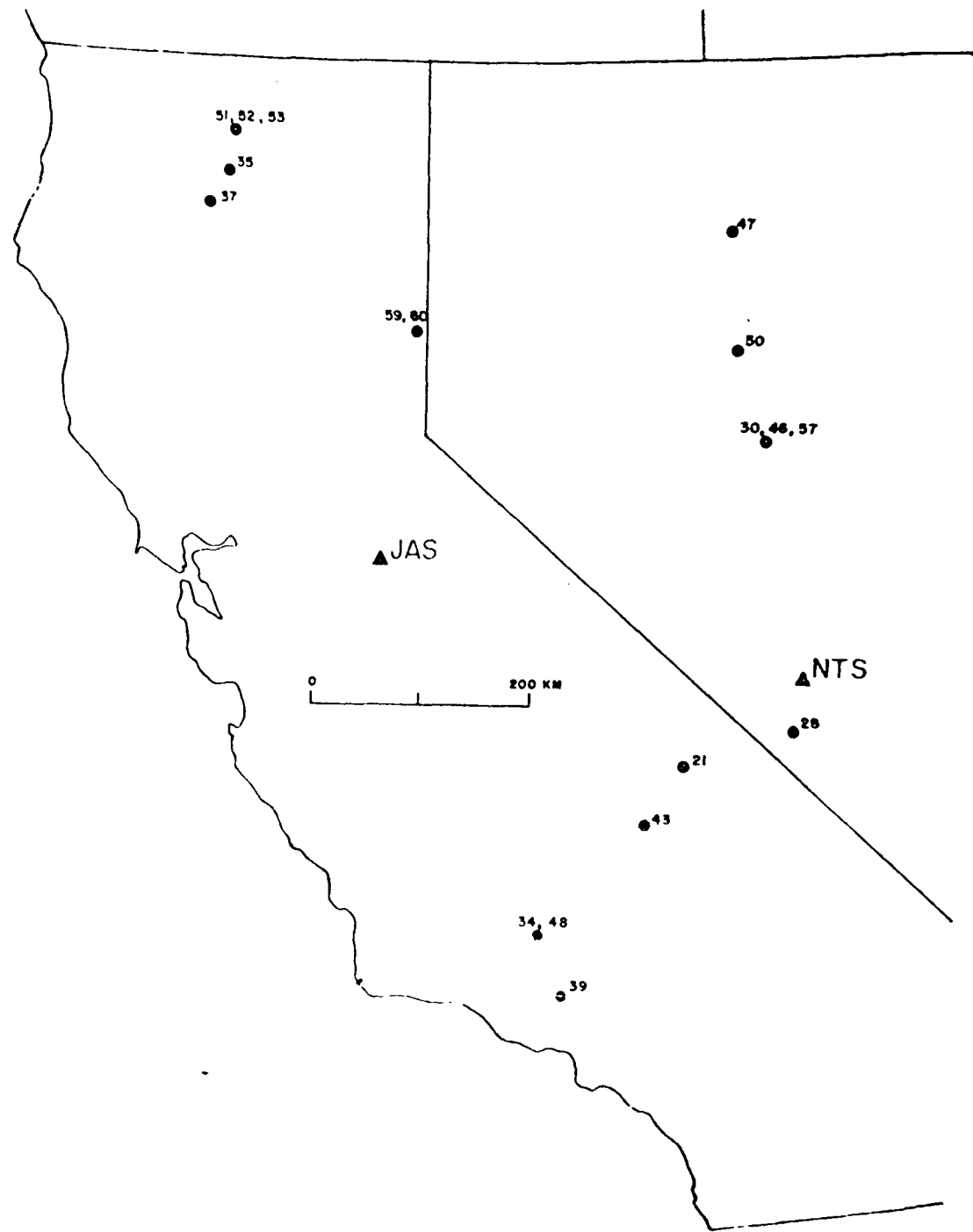


Fig 3

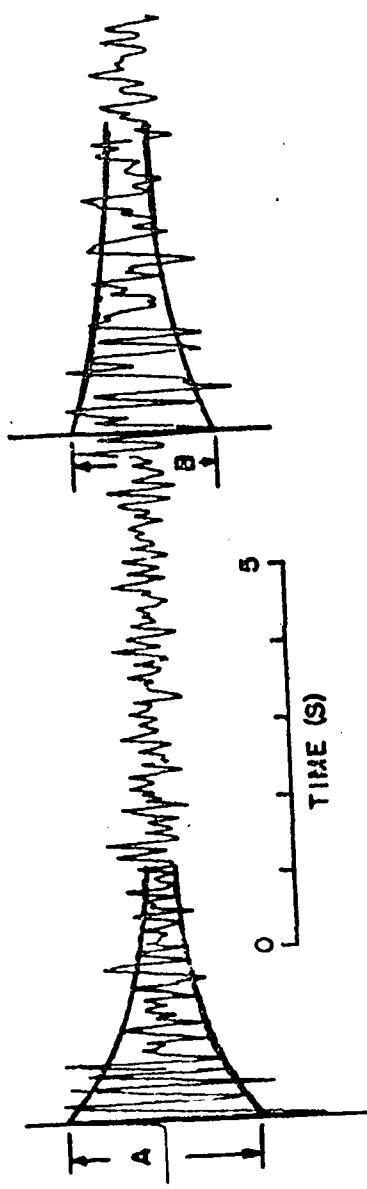


Fig 4

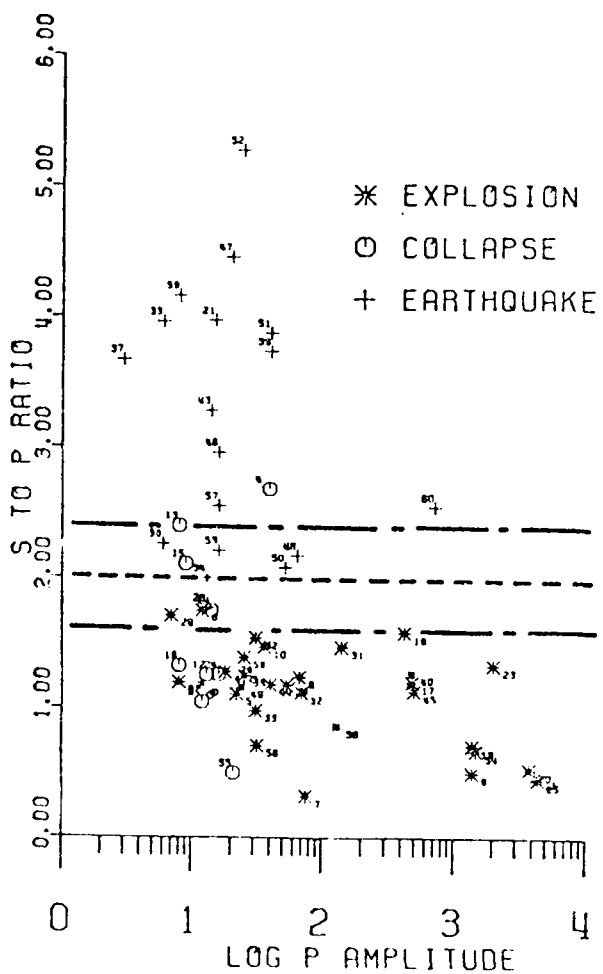


Fig 5

plitude of the envelope at roughly the phase onset is measured, the peak-to-peak amplitudes "A" and "B" for Pg and Sg, respectively in the figure.

Figure 5. Plot of Sg to Pg amplitude ratio (Ratio of B to A in Figure 4) plotted versus log of Pg envelope amplitude, the values given in Table 2. The smaller symbols denote starred readings from the Table. Dashed line is the decision line (earthquakes above and explosions below). Dot-dashed lines delimit a region of uncertain identification (see text).

[6] IMPULSE SOLUTIONS IN A LAYERED ELASTIC MEDIUM:

EXTENDED LAMB'S PROBLEM

William A. Peppin

ABSTRACT

Johnson (1974) has presented the complete solution for displacements and stresses in an elastic halfspace resulting from a localized impulse source (Lamb, 1904). This paper extends Johnson's formulation to a multilayered elastic medium by presenting a solution in terms of generalized rays, and like him this method is exact in the sense that no asymptotic expansion is used. Some sample calculations are presented which compares the method with asymptotic ray theory (Wiggins and Helmburger, 1974), and which shows the importance of the near-field terms in the analysis of real seismograms.

1. Introduction

The purpose of this paper is to extend Johnson's (1974) results for the elastic displacements resulting from point-force and point-couple sources in a homogeneous, isotropic, elastic halfspace; the methods used parallel his work closely (Sato, 1973a, b derives similar results using another approach). The motivation for this presentation derives from recent emergence of excellent, wideband digital data close to explosion and earthquakes sources and the development of the seismic moment-tensor inversion method for source parameters (Gilbert, 1970; Stump and Johnson, 1977; Stump, 1979). The formulation presented here is not amenable to fast computation of such solutions, and the reader who needs speed is referred to existing generalized-ray codes following Wiggins and Helmburger (1974) or to the very fast WKBJ code written by C. H. Chapman, J. A. Orcutt, and M. Reichle following Chapman (1978) and Dey Sarkar and Chapman (1978). It finds application in cases where impulse solutions are required very close to the source (within 10 km), as near-field effects can be observed strongly (see Section 11). Moreover, in many cases the asymptotic ray expansions continue to be accurate even at close distance ranges. Thus, a second motivation is to explore the need for the exact formulation at these ranges. Only aspects of the mathematics unique to this formulation are described below; the interested reader will find all details in Peppin (1974) and Johnson (1974). In this paper equation number "nnn" from the latter reference is cited as "Jnnn".

2. Choice of Coordinates

Let a right-handed Cartesian coordinate system (X_1 , X_2 , X_3) be imbedded in the halfspace with the plane $X_3 = 0$ coincident with the free surface and with the X_3 -axis passing through the source, which is located at $(0, 0, X_3' = -h)$. Let unprimed and primed coordinates represent, respectively, receiver and source coordinates. Note that X_3 is positive upward, unlike Johnson (1974); see Figure 1.

3. Statement of the Problem

Assume a halfspace divided into homogeneous, isotropic, elastic layers. These are numbered downward from the top layer, which is 1, and interfaces are numbered downward from the top of the halfspace, which is a free surface (interface number 0). Each layer is defined by the four quantities a , b , r , and H , the P- and S-wave velocities, the density, and the layer thickness, respectively. All numeric subscripts pertain to the layer number. All interfaces are assumed welded, so that displacement and surface traction are continuous across them. Assume a source buried at depth "h" consisting of a point force in the direction (f_1, f_2, f_3) (cf J4):

$$\underline{f}(x, t) = (f_1, f_2, f_3)^T \delta(x_1) \delta(x_2) \delta(x_3 + h) N_0(t) \quad \dots (1)$$

In (1) the deltas denote Dirac delta functions, the source is located at $(0, 0, -h)$, and the source time history is $N_0(t)$, taken zero for all times $t < 0$. The problem is to compute displacements at any point on the surface of the halfspace in response to this source.

4. Notation

h	source depth (cm)	
λ^2	$p^2 + q^2$ or $a^2 + b^2$, squared horizontal wave slowness (sec/cm) ²	X []
$N_0(t)$	time dependence of applied source	
p, q	wave slownesses in x and y directions (sec/cm)	
r	epicentral distance (cm)	
Ω	Rayleigh's function $(\omega^2 + 4l^2n^2) \Omega^2 + 4l^2\eta_x \eta_y$	X []
s	temporal Laplace transform variable (sec)-1	
T_{ij}	Cauchy stress; jth component of traction across the plane perpendicular to the xi axis (dyne/cm ²)	[]
u_i	elastic displacement (cm)	[]
α_j	P-wave velocity in jth layer (cm/sec)	X []
β_j	S-wave velocity in jth layer (cm/sec)	X []
η_x	$(1/a^2 - \lambda^2) \cdot .5$ vertical P-wave slowness in jth layer (sec/cm) ²	X []
	$\rightarrow \alpha_j^2 - \lambda^2$	[]

η_{pj}	$1/\beta_j^2 - \lambda^2$	X
η	$(1/\lambda_2 - \lambda)^2$ vertical S-wave slowness in jth layer	X
η	(sec/cm) \rightarrow	X
λ_j, μ_j	Lame's elastic constants in jth layer (dyne/cm)	X
ρ_j	density in jth layer (g/cm ³)	X
ϕ	counterclockwise azimuth angle from E, source to receiver \rightarrow	X
ω	$\omega_b^2 - 12 = 1/b^2 - 212 \quad \eta_j^2 - \lambda^2 = 1/\beta_j^2 - 2\lambda^2$	X

5. Solutions in the transform domain Following Johnson (1974) we apply coordinate transformations to the Cauchy-Navier equations J1 and the isotropic generalized Hooke's law (Mase, 1970, p 144) assuming infinitesimal strain (Mase, 1970, p 83). These coordinate transformations are defined below; they take time "t", "x₁", and "x₂" into "s", "p", and "q", respectively. For any function "f" of these variables we define

$$\begin{aligned} \tilde{f}(x_1, x_2, x_3, s) &\equiv \int_0^\infty f(x_1, x_2, x_3, t) e^{-st} dt \\ f(x_1, x_2, x_3, t) &= \frac{1}{2\pi i} \int_{-i\infty}^{i\infty} \tilde{f}(x_1, x_2, x_3, s) e^{st} ds \end{aligned} \quad \text{--- (2)}$$

$$\begin{aligned} \bar{f}(p, x_2, x_3, s) &\equiv \int_{-\infty}^{\infty} \tilde{f}(x_1, x_2, x_3, s) e^{+spx_1} dx_1 \\ \tilde{f}(x_1, x_2, x_3, s) &= \frac{s}{2\pi i} \int_{-i\infty}^{i\infty} \bar{f}(p, x_2, x_3, s) e^{-spx_1} dp \end{aligned} \quad \text{--- (3)}$$

$$\begin{aligned} \bar{f}(p, q, x_3, s) &\equiv \int_{-\infty}^{\infty} \bar{f}(p, x_2, x_3, s) e^{+sqx_2} dx_2 \\ \bar{f}(p, x_2, x_3, s) &= \frac{s}{2\pi i} \int_{-\infty}^{\infty} \bar{f}(p, q, x_3, s) e^{-sqx_2} dq \end{aligned} \quad \text{--- (4)}$$

The requirement for solution of the problem is that all of the transforms defined in (2) - (4) exist and that the inverse transformations can be computed on some contour parallel to the imaginary axis. These conditions are met under J8 (see also Peppin, 1974, pp 157-158). The result is nine equations in the transformed displacements $\underline{\underline{u}}$ and tractions $\underline{\underline{T}}$. These are rearranged to separate P-SV from SH terms (Peppin, 1974, pp 156-160 and 234-236). The result was presented in equivalent form by Gilbert and Backus (1966) and Chapman (1973):

$$\frac{d \underline{\underline{\tilde{V}}}}{d X_3} = S \underline{\underline{M}} \cdot \underline{\underline{\tilde{V}}} + \underline{\underline{\tilde{W}}} \quad \dots \quad (5)$$

where

$$\underline{\underline{\tilde{V}}} = \begin{bmatrix} s(\bar{u}_1 \sin \xi + \bar{u}_2 \cos \xi) \\ \bar{T}_{33} \\ s \bar{u}_{33} \\ \bar{T}_{31} \sin \xi + \bar{T}_{32} \cos \xi \\ s(\bar{u}_2 \sin \xi - \bar{u}_1 \cos \xi) \\ \bar{T}_{32} \sin \xi - \bar{T}_{31} \cos \xi \end{bmatrix}, \quad \underline{\underline{\tilde{W}}} = \begin{bmatrix} 0 \\ -t_3 \\ 0 \\ -f_1 \sin \xi - f_2 \cos \xi \\ 0 \\ -f_2 \cos \xi + f_1 \sin \xi \end{bmatrix}$$

$$\tilde{N}_0(s)\delta(x_3 + h)$$

$$\underline{\underline{M}} = \begin{bmatrix} 0 & 0 & l & 1/\mu & 0 & 0 \\ 0 & 0 & p & l & 0 & 0 \\ \frac{\lambda}{\lambda + 2\mu} & \frac{1}{\lambda + 2\mu} & 0 & 0 & 0 & 0 \\ P - \frac{4\lambda^2\mu(\lambda + \mu)}{\lambda + 2\mu} & \frac{\lambda}{\lambda + 2\mu} & 0 & 0 & 0 & 0 \\ 0 & 0 & 0 & 0 & 0 & 1/\mu \\ 0 & 0 & 0 & 0 & p\mu l^2 & 0 \end{bmatrix}, \quad \begin{aligned} \sin \xi &\equiv 1/l \\ \cos \xi &\equiv q/l \end{aligned}$$

In (5) $V_1 - V_4$ are the transformed displacement-stresses associated with the P-SV problem and V_5, V_6 are those associated with the SH problem (see Peppin, 1974, 237-239). In general, this separation is not possible in the (X_1, X_2, X_3, t) domain.

To solve (5) for V the method is to: solve above and below the source; set conditions joining together the solutions above and below the source. First, note that solutions of (5) can be taken conveniently as a linear combination of the eigenvectors of the matrix M . Chapman (1973) has presented these and the corresponding eigenvalues in terms of vertical wave slownesses

$$\eta_c = \sqrt{\eta_c^2 - \ell^2}$$

where "c" is a or b.

The six eigenvectors and their associated eigenvalues are as follows:

eigenvalue	eigenvector
$-\eta_a$	$A \equiv \frac{i}{\sqrt{2\mu\eta_a}} (-\lambda, \mu\Omega, -\eta_a, 2\mu\Omega\eta_a, 0, 0)^T$
$-\eta_\beta$	$B \equiv \frac{i}{\sqrt{2\mu\eta_\beta}} (\eta_\beta, 2\mu\lambda\eta_\beta, -\ell, \mu\Omega, 0, 0)^T$
$-\eta_\beta$	$C \equiv \frac{1}{\sqrt{2\mu\eta_\beta}} (0, 0, 0, 0, 1, -\mu\eta_\beta)^T$
$+\eta_a$	$D \equiv \frac{1}{\sqrt{2\mu\eta_a}} (\lambda, \mu\Omega, \eta_a, -2\mu\lambda\eta_a, 0, 0)^T$
$+\eta_\beta$	$E \equiv \frac{i}{\sqrt{2\mu\eta_\beta}} (-\eta_\beta, -2\mu\lambda\eta_\beta, -\ell, \mu\Omega, 0, 0)^T$
$+\eta_\beta$	$F \equiv \frac{1}{\sqrt{2\mu\eta_\beta}} (0, 0, 0, 0, 1, \mu\eta_\beta)^T$

... (7)

where

$$\Omega = \eta \beta^2 - \lambda^2$$

1/2 A

$\omega = nb^2 - 12$

Peppin (1974), pp 240-245 shows that A, B, and C are upward-travelling P, SV, and SH waves while D, E, and F are downward-travelling P, SV, and SH waves. Thus, we solve (5) above the source in terms of \tilde{A} , \tilde{B} , and \tilde{C} , and below the source in terms of \tilde{D} , \tilde{E} , and \tilde{F} . That is, we seek constants K1, K2, and K3 such that above the source

$$\tilde{v} = K_1 \tilde{A} e^{-s\eta\beta(x_s+h)} + K_2 \tilde{B} e^{-s\eta\beta(x_s+h)} + K_3 \tilde{C} e^{-s\eta\beta(x_s+h)} \quad \dots (8)$$

and constants K4, K5, and K6 such that below the source

$$\tilde{v} = K_4 \tilde{D} e^{+s\eta\beta(x_s+h)} + K_5 \tilde{E} e^{+s\eta\beta(x_s+h)} + K_6 \tilde{F} e^{+s\eta\beta(x_s+h)} \quad \dots (9)$$

Substitution of (8) and (9) in (5) shows that these are valid solutions for \tilde{V}_1 , \tilde{V}_3 , and \tilde{V}_5 for any value of the constants "K". To find these constants, note that \tilde{V}_2 , \tilde{V}_4 , and \tilde{V}_6 , the transformed stresses, suffer discontinuities due to the presence of the delta function.

Thus, from (5)

$$\begin{aligned} d\tilde{V}_2 &= \left[s(\underline{\underline{M}} \cdot \tilde{\underline{\underline{V}}})_2 + \tilde{W}_2 \right] dx_s \\ \Delta \tilde{V}_2 &= \int_{-h-s}^{-h+s} \left[s(\underline{\underline{M}} \cdot \tilde{\underline{\underline{V}}})_2 + \tilde{W}_2 \right] dx_s \\ &= \int_{-h-s}^{-h+s} \tilde{V} \tilde{V}_2 dx_s \quad \text{for small } \delta \text{ since} \\ &\quad \underline{\underline{M}} \text{ and } \tilde{\underline{\underline{V}}} \text{ are bounded} \\ &= -f_3 \tilde{N}_v(s) \quad \dots \dots \dots (10.a) \end{aligned}$$

Similarly

$$\begin{aligned} \Delta \tilde{V}_4 &= - (f_1 \sin \delta + f_2 \cos \delta) \tilde{N}_v(s) \quad \dots (10.b) \\ \Delta \tilde{V}_6 &= - (f_2 \sin \delta - f_1 \cos \delta) \tilde{N}_v(s) \quad \dots (10.c) \end{aligned}$$

Thus, inserting (10) in (5) to match the solutions above and below the source

$$K_1 A_1 + K_2 \bar{B}_1 + K_4 D_1 + K_5 E_1 = 0$$

$$K_1 A_2 + K_2 \bar{B}_2 + K_4 D_2 + K_5 E_2 = -f_s \tilde{N}_c(s)$$

$$K_1 A_3 + K_2 \bar{B}_3 + K_4 D_3 + K_5 E_3 = 0$$

$$K_1 A_4 + K_2 \bar{B}_4 + K_4 D_4 + K_5 E_4 = -(f_1 \sin \xi + f_2 \cos \xi) \tilde{N}_c(s)$$

$$K_1 C_5 + K_6 F_5 = 0$$

$$K_3 C_6 + K_6 F_6 = -(f_2 \sin \xi - f_1 \cos \xi) \tilde{N}_c(s)$$

- - - - - (11)

so that

$$\left. \begin{aligned} K_1 &= \frac{\tilde{N}_c(s)}{\sqrt{2} \sin \xi} (Z_1 I_x + H_1 l) \\ K_2 &= \frac{-i \tilde{N}_c(s)}{\sqrt{2} \rho \sin \xi} (Z_1 l - H_1 I_x) \end{aligned} \right\} - - - (12)$$

$$\left. \begin{aligned} K_4 &= \frac{\tilde{N}_c(s)}{\sqrt{2} \rho \sin \xi} (Z_1 I_x - H_1 l) \\ K_5 &= \frac{i \tilde{N}_c(s)}{\sqrt{2} \rho \sin \xi} (Z_1 l + H_1 I_x) \end{aligned} \right\} - - - (13)$$

$$\left. \begin{aligned} K_3 &= -\frac{\tilde{N}_c(s) T}{\sqrt{2} \mu \sin \xi} \\ K_6 &= \frac{\tilde{N}_c(s) T}{\sqrt{2} \mu \sin \xi} \end{aligned} \right\} - - - (13)$$

where

$$H \equiv - (f_1 \sin \delta + f_2 \cos \delta)$$

$$T \equiv - (f_2 \sin \delta - f_1 \cos \delta)$$

$$Z \equiv - f_3$$

The solutions (8) and (9) to (5) are obtained by inserting (12) and (13). If the source is on an interface, (12) and (13) do not apply, and we would have to return to (11) and solve with differing source properties above and below the source.

6. Solutions at the Free Surface

All solutions presented in this paper assume a buried source and a receiver placed on the free surface. The condition to be set is that the tractions \bar{V}_2 , \bar{V}_4 , and \bar{V}_6 vanish there. The three cases to consider are: incident P, SV, or SH. Notation used is given in Figure 2. With these definitions, we see for the P problem that

$$\bar{V} (x_3 = 0) = A + P0_{22} D + P0_{42} E \quad \dots (14)$$

With the transformed surface tractions $V_2 = V_4 = 0$, we find that

$$P0_{22} = - \frac{\Omega^2 + 4\ell^2 \eta_x \eta_z}{R}, \quad P0_{42} = - 4i\ell \Omega (\eta_x \eta_z)^{1/2} \quad \dots (15)$$

$$R = \Omega^2 + 4\ell^2 \eta_x \eta_z \quad \text{Rayleigh's function}$$

For the incident SV problem we find $P0_{22} = P0_{44}$, $P0_{42} = P0_{24}$. Thus, from (14) and similar relations for SV and SH we find that the incident displacements are modified by interaction with the free surface through multiplicative factors. The transformed solutions at the free surface apart from the exponential factors in (8) and (9) are

$$\left[\begin{array}{c} \bar{V}_1 \\ \bar{V}_3 \end{array} \right] = \frac{1}{\beta^2 R \sqrt{2f_0^2 \eta_B}} \left[\begin{array}{c} -4\ell N_w \eta \beta \\ -2\Omega N_w \end{array} \right] \cdot K_j \quad (\text{upgoing } P) \quad \left. \right\} \dots (16)$$

$$\left[\begin{array}{c} \bar{V}_1 \\ \bar{V}_3 \end{array} \right] = \frac{1}{\beta^2 R \sqrt{2f_0^2 \eta_B}} \left[\begin{array}{c} 2\Omega \eta \beta \\ -4\ell N_w \eta \beta \end{array} \right] \cdot K_j \quad (\text{upgoing } SV) \quad \left. \right\}$$

$$\bar{V}_5 = \frac{2}{\sqrt{2\mu \eta \beta}} \cdot K_j \quad (\text{upgoing } SH) \quad \left. \right\}$$

In (16) "K_j", j = 1 to 6 are the source factors from (12) and (13); all elastic properties and vertical slownesses depend upon the properties of the source layer in these expressions. In contrast, all elastic properties and vertical slownesses appearing in (16) apart from the K_js depend on the properties of the uppermost layer. Note how (16) shows complete separation of the effects of source and receiver in this problem.

7. Shift to Polar Coordinates in the Transform Domain

A final step is necessary before inversion to the desired displacements. Note that \bar{V}_1 and \bar{V}_5 are not the transforms of physically useful quantities: see (5). To rectify this, DeHoop (1961) suggests a shift in the transform parameters as follows:

$$\begin{aligned} p &= a \cos \phi - b \sin \phi \\ q &= a \sin \phi + b \cos \phi \end{aligned} \quad \left. \right\} \quad \dots \quad (17)$$

where " ϕ " is the polar angle of the line from source to receiver measured from due east (Figure 1). This simplifies the inversion integrals, because under (17)

$$-\text{spx}_1 - \text{sqx}_2 = -\text{spr}\cos(\phi) - \text{qr}\sin(\phi) = -\text{sra}$$

and

$$dpdq = da db.$$

Now define longitudinal and transverse components in terms of previously-defined quantities:

$$\begin{aligned} f_r &= f_1 \cos \phi + f_2 \sin \phi \\ f_\theta &= -f_1 \sin \phi + f_2 \cos \phi \\ u_r &= u_1 \cos \phi + u_2 \sin \phi \\ u_\theta &= -u_1 \sin \phi + u_2 \cos \phi \end{aligned} \quad \left. \right\} \quad \dots \quad (18)$$

where radially away from the source and transverse to the right looking at the source from the receiver are taken as positive. From (17), (18), and (5)

$$\left. \begin{aligned} \bar{\mu}_r &= (\bar{v}_i \alpha - \bar{v}_s b) / s \ell \\ \bar{\mu}_\theta &= (\bar{v}_i b + \bar{v}_s \alpha) / s \ell \\ H &= -\tilde{N}_o(s)(a f_r + b f_\theta) / \ell \\ T &= -\tilde{N}_o(s)(a f_\theta - b f_r) / \ell \end{aligned} \right\} \dots (19)$$

At this point, apart from the modifications needed for computing an arbitrary generalized ray, the method follows Johnson (1974) at and beyond J20. The only significant difference up to this point is that the SV and SH waves are here separated, while in Johnson (1974) they are not. The separation is required in the multilayer case because SV and SH reflection-transmission coefficients differ.

7. Inversion to the Time Domain

We present here specific formulas for the halfspace case; the modification of these to arbitrary generalized rays is easy (see below). Applying (18) and (19) in (8) or (9) using (12) or (12) allows solution in the transform domain for (u_r, u_θ, u_z) . To these apply inversion integrals (3) and (4). Shift the integration variables from $d\rho dq$ to $da db$. The result at the free surface got using (16) is

x w

$$\begin{aligned}
 (\tilde{u}_r, \tilde{u}_\theta, \tilde{u}_z)^T &= \frac{s \tilde{N}_0(s)}{4\pi^2 \mu} \left[\iint_{-i\omega}^{i\omega} \hat{\underline{P}} \cdot \underline{f} e^{-sra - s\eta_x h} da db + \right. \\
 &+ \iint_{-i\omega}^{i\omega} \hat{\underline{V}} \cdot \underline{f} e^{-sra - s\eta_y h} da db + \\
 &\left. + \iint_{-i\omega}^{i\omega} \hat{\underline{H}} \cdot \underline{f} e^{-sra - s\eta_z h} da db \right] \quad \dots (20)
 \end{aligned}$$

where $f = (f_r, f_\theta, f_z)$, \hat{P} is similar to \underline{M} in J16, and where $\hat{S}V + \hat{SH}$ is similar to \underline{N} in J16, i.e.,

$$\hat{P} = \frac{1}{R} \begin{bmatrix} 2a^2\eta_S & 2ab\eta_{S3} & 2ac\eta_{aB} \\ 2ab\eta_S & 2b^2\eta_3 & 2b\eta_a\eta_3 \\ 2c\eta_a & 2b\eta_a & 2\eta_a \end{bmatrix}$$

$$\hat{S}^V = \frac{i}{R} \begin{bmatrix} \frac{a^2 \Omega n_s}{\epsilon^2} & \frac{ab \Omega n_s}{\epsilon^2} & -a \Omega \\ \frac{ab \Omega n_s}{\epsilon^2} & \frac{b^2 \Omega n_s}{\epsilon^2} & -b \Omega \\ -2an_s n_\beta & -2bn_s n_\beta & 2n_s \epsilon^2 \end{bmatrix} \quad \dots (21)$$

$$\hat{SH} \equiv \frac{1}{\epsilon^2 \eta_3} \begin{bmatrix} b^2 & -ab & 0 \\ -ab & a^2 & 0 \\ 0 & 0 & 0 \end{bmatrix}$$

For any specified source type, the integrals (20) must be reduced to a standard form. Here we show the reductions explicitly for a source of type (1). The integral over "a" is reduced by the principle of reflection (Peppin, 1974, pp 246-247) to the domain $[0, i\infty]$. Then we shift the "b" integral to the real axis ($b = i\infty$), on the domain $[0, i\infty]$. In this new domain we discard all terms in the integrand that are odd in λ . The result for the halfspace case is

$$\begin{aligned}
 (\tilde{\mu}_r, \tilde{\mu}_e, \tilde{\mu}_z)^T &= \frac{s \tilde{N}_n(s)}{\pi^2 u} \left[\int_0^\omega \text{Im} \int_0^{ia} \frac{P \cdot f}{s - \tilde{\gamma}} e^{-sra - sith} da dt + \right. \\
 &\quad + \int_0^\omega \text{Im} \int_0^{ia} \frac{sv \cdot f}{s - \tilde{\gamma}} e^{-sra - sith} da dt + \\
 &\quad \left. + \int_0^\omega \text{Im} \int_0^{ia} \frac{sh \cdot f}{s - \tilde{\gamma}} e^{-sra - sith} da dt \right] \dots (22)
 \end{aligned}$$

where P, SV, and SH are derived from (20) by substituting $b = ie$ and dropping all terms odd in this new integration variable.

Now shift the inner "a" integrals in (22) over to the real variable "t" which has units of time:

$$t \equiv ar + \eta_0 H, c = \alpha \text{ or } \beta \quad \dots (23)$$

This deforms the contour of integration from the imaginary axis onto the Cagniard-deHoop contour, which runs along the real "a" axis, then steps into the first quadrant before it reaches the branch point at $\eta_0(\epsilon a)^2 = 0$ on the real "a" axis. The deformation requires that no singularity lies between the two contours, which is true as long as the source is below the free surface (Peppin, 1974, pp 255-258). Under this variable change, the first integral in (22) becomes

$$\frac{s \tilde{N}_0(s)}{\pi \mu} \int_{\epsilon}^{\infty} \int_{t_{min}}^{\infty} \operatorname{Im} \left\{ \tilde{P} \cdot f \frac{da}{dt} \right\} e^{-st} dt d\epsilon \quad \dots (24)$$

It is crucial for the method to note that in (24) the lower limit of the inner integral "tmin" always exceeds zero. This is true because for a range of values $t > 0$, real values of "a" are required in (23), so that the integrand in (24) has no imaginary part. Physically, "tmin" corresponds either to the Fermat arrival time (where the Cagniard-deHoop contour leaves the real axis) or to the earliest headwave arrival time (contour encounters a branch point along the real "a" axis corresponding to a zero of an η_0 not appearing explicitly in (23)). For the halfspace and other special cases, "tmin" can be given explicitly (see J28). Thus, because "tmin" is positive in all cases, when in (24) we invert the order of integration, the inner integral (now over ϵ) extends to a bounded upper limit. A second crucial requirement is that "tmin" is monotonically increasing in " ϵ ", or else this order reversal cannot be accomplished simply.

This point is explicitly true for the halfspace case (see J27) and can be proved for the general case as well (see below). Under this further change, (24) becomes

$$\frac{s \tilde{N}_0(s)}{\pi^2 \mu} \int_0^\infty \left\{ \int_0^{e(t)} \operatorname{Im} \left\{ P \cdot f \frac{da}{dt} \right\} de \right\} e^{-st} dt \quad \dots (25)$$

If $\tilde{N}_0(s)$ is $1/s$, then $N_0(t)$ is $H(t)$, the Heaviside step function. In this case the factor "s" is contained only in the exponent of "e" in (25), so that the time-domain results we want consist of the integrand of the "t" integration in (25). Thus, the time-domain inversion of (20) for a step-function source is

$$(u_r, u_\theta, u_z)^T = \frac{1}{\pi^2 \mu} \left[\int_0^{e_p(t)} \operatorname{Im} \left\{ P \cdot f \frac{da}{dt} \right\} de + \right. \\ + \int_0^{e_{sv}(t)} \operatorname{Im} \left\{ s v \cdot f \frac{da}{dt} \right\} de + \\ \left. + \int_0^{e_{sn}(t)} \operatorname{Im} \left\{ s i \cdot f \frac{da}{dt} \right\} de \right] \quad \dots (26)$$

The form (26) implies that the displacements can be computed at any specified time through real quadratures. Once the desired time "t" is specified, we compute the upper limit $e(t)$ in (26): see below. Then to evaluate the integrand at a submesh point " e_i ", we solve for "a" in (23). All expressions within the integrand are functions of "t", " e_i ", and the value of "a" just found.

8. Generalization to Higher-Order Sources

The displacements resulting from higher-order force moments, equivalent to spatial derivatives of the above fundamental source with

respect to source coordinates, can be obtained as suggested by Johnson (1974). Suppose that we differentiate the equations to be transformed with respect to source coordinates X_1' or X_2' . Then this source derivative would be applied to (1). Notice that an increase in source coordinates is equivalent to a decrease in receiver coordinates by the same amount. Thus,

$$\frac{\partial}{\partial X_j} = - \frac{\partial}{\partial x_j}, \quad j = 1, 2, 3$$

Under (3) and (4) the unprimed (receiver) X_1 and X_2 derivatives lead to a multiplicative factor $-s_p$ and $-s_q$, respectively, which shows up in the source term of (5). Thus, the primed X_1 and X_2 (source) derivatives multiplicative factors $+s_p$ and $+s_q$ in the source term of (5), so that derivatives with respect to either source or receiver coordinates X_1 and X_2 modify the solution by introducing the above factors in (21). For each such derivative another factor of "s" is introduced; thus, to effect Cagniard-deHoop inversion leading to (26), we must modify $N_o(t)$ to eliminate any accumulated multiplicative factors of "s" outside the exponent in (25).

Consider derivatives with respect to source depth. It is convenient to carry that differentiation through to (8) and (9) and take this derivative explicitly. For upgoing rays, noting that the derivative we want is

$$\frac{d}{d(-h)}, \quad +s_1 \gamma_c - s_2 \gamma_c$$

we multiply the solution, hence (22) by $+s_1 \gamma_c$ and $-s_2 \gamma_c$ for upgoing and downgoing rays, respectively ($c = \alpha$ or β).

$$\alpha \quad \beta$$

Thus, to proceed to any higher-order source, introduce in (22) one such factor for each derivative, drop all terms odd in "b" from the result, and proceed exactly as above to a real-valued quadrature. Rather than present a list of these solutions, the reader can see most easily how these derivatives are introduced by studying the relevant

subroutine for computing source, receiver, and source-derivative factors: see the Appendix.

9. Modification for an Arbitrary Generalized Raypath

Formula (26) can be used with slight modification for the case of an arbitrary raypath, as shown in Figure 3. In this case we start with the integral for SV leaving the source downward (the second integral of (26); the factor K_5 in (12)). Cisternas et al. (1973) show that propagation along any realizable raypath can be accounted for in the transform domain by products involving the reflection-transmission coefficients for each interface interaction and exponential decay factors dependent on the vertical layer thickness traversed (this is the distance-decay factor). The results for the ray shown in Figure 3 is to replace the factor

$$e^{+s\eta_B(x_i + h)}$$

in (9) with

$$S_{212} S_{124} e^{-s\eta_B(h_1 + H_2 - h)} = s\eta_{x_2} H_2 - s\eta_{x_1} H_1 \quad \text{--- (27)}$$

where S_{212} and S_{124} are the corresponding reflection-transmission coefficients, and where single subscripts pertain to layer number. Thus the integrand in (26) will contain the added multiplicative factor $(S_{212} S_{124})$ and (23) explicitly becomes

$$t = ar + \eta s_2(h_1 + H_2 - h) + \eta_{x_2} H_2 + \eta_{x_1} H_1 \quad \text{--- (28)}$$

Note that (23) can be solved analytically for "a" (see J31 and J32), but (28) must be solved numerically for "a". For real values of "a", (28) sometimes has two real roots; the smaller of these is taken.

Thus, the procedure is to specify all of the generalized raypaths of interest, introduce the corresponding reflection-transmission factors of each generalized ray in the integrand of (26) and proceed to a real-valued quadrature as before for the halfspace case.

Note that most of the time spent in numerical evaluation of such integrals is in finding the complex roots of (28). Also note that, for complicated raypaths, the kinematic and dynamic groups must be recognized, as a single member of such a group has no physical meaning.

10. Numerical Aspects of the Quadrature in (26)

In (26) it remains to discuss the computation of the upper limits of integration. These must be computed at each time step. The topology of the domain of integration involving these limits is shown schematically in Figure 4. The shaded regions in the figure denote regions of $e-t$ space that contribute to the integral; for a specified time the domain of integration is a vertical line from the $e = 0$ axis at that time to the upper limit of the shaded region. Suppose we desire to compute the integral at time "tp" (see the figure). Then the three limits e_1 , e_2 , and e_3 must all be known. This is because the integrand in (26) contains: bounded but infinite-slope singularities at e_1 and e_2 ; a square-root singularity at e_3 . To achieve sufficient accuracy (1 part in 500,000), the integral is subdivided into regions between these limits. A simple change of variable is sufficient to eliminate each part of the integrand that is non polynomial (Peppin, 1974, pp 192-194).

The headwave limits like e_1 and e_2 derive from analytical formulas like the second of J27 with the obvious extension to the multilayer case (i.e., solve for e in (28) for which $\lambda^2 = \frac{1}{\nu_{e_1}^2}$, and this the corresponding headwave slowness is less than any of the slownesses appearing in the n_{e_1} 's of (28)). The Fermat limit e_3 can only be given explicitly (first of J27) for rays in which only one vertical slowness

nc appears in (24), such as internal layer reflections in addition to the halfspace rays. Otherwise it is found as the value of e which satisfies the expression corresponding to (28) for the given time tp and which satisfies the saddlepoint condition

$$\frac{dt}{da} = 0$$

Peppin (1977) shows that these two conditions are met for the value of "λ" satisfying

$$B(\lambda) = \left(t - \sum_{j=1}^N H_j \eta_j \right) \left(\sum_{j=1}^N H_j / \eta_j \right) - r^2 = 0 \quad \dots (29)$$

where the sums extend over each distinct vertical slowness in expressions like (28) for a particular generalized ray. The zero of $B(\lambda)$ is easy to find numerically; only one real root exists (Peppin, 1977). Substituting this root in (29) permits solution for "a", then for the desired upper limit as $(\alpha^2 - \lambda^2)^{1/2}$. $\alpha^2 - \lambda^2$

A second aspect of the numerical calculations is that the generalized reflection-transmission coefficients must be known. These are provided by Chapman (1973). The computation of these can be laborious, consuming up to 25% of the total processing time required. To make a run involving 25 generalized rays in a fairly complicated layer stack, 100 seconds of CYBER176 time are required for close-in calculations (at distance this can be reduced by an order of magnitude). Many possibilities exist to shorten this processing time considerably, but these have not been fully explored because of the existence of much faster, approximate methods such as the WKBJ method of Chapman (1978).

11. Numerical Examples

A computer program MEXEC, written in FORTRAN, evaluates (26) for

any generalized raypath. The source is specified in terms of an arbitrarily-oriented point force (1) or of spatial derivatives of this source with respect to source coordinates. The subroutine appearing in the Appendix is written to accommodate extension to higher-order sources. In the current version of MEXEC ten components of ground motion are computed; they are the canonical source components of Stump and Johnson (1977) and Stump (1979). Any point source can be expressed as a linear combination of the canonical sources through the seismic moment tensor (Stump, 1979); these sources are the starting point for Stump and Johnson's procedure to invert seismograms for fault parameters. Output of the code has been checked against the calculations presented by Johnson (1974) for the halfspace and by a modification of D. V. Helmberger's code for asymptotic ray calculations of the canonical sources (Walt Silva, personal communication, 1980). MEXEC runs successfully on five CYBER-based systems and on one 32-bit system.

A. The Importance of Near-Field Motions

In Figure 5 are presented displacement seismograms recorded on a wideband digital system (Peppin and Bufe, 1980) close to the hypocenters of two sizeable earthquakes. Also shown are predicted ground motions computed by MEXEC for a halfspace. Note in the figure the distinct ramplike motion between the P and S phases. This is the near-field motion which disappears at distance from the source. Because theoretical and observed traces are so similar, little doubt remains that we have correctly identified near-field motions in these cases. Such motion has been observed on hundreds of displacement seismograms taken within 20 km of the source (Peppin and Somerville, 1980).

B. Comparison with Asymptotic Ray Theory

How significant an error is made by the utilization of the much

faster (factor of 50) asymptotic ray calculation? In many cases, almost none as we shall see. A test run was made for a source depth of 8 km, a receiver distance of 32 km, and a layer thickness of 32 km. The results agree quite closely for all of the ten canonical source components except the transverse ones. Figure 6 shows a comparison for strikeslip sources and Figure 7 for dipslip ones. The disagreement between the two formulations is significant only in the near-field part of the transverse components: asymptotic ray theory produces no near-field term. The data in Figure 5 require these terms to explain the observed ramp between the P and S phases. Note, however, that the step offset on the transverse components (the "far-field" term) agrees quite closely in spite of the discrepancy suggested by the figure (for drawing convenience only). Also note that the differences between the two theories are emphasized in that the calculations shown are for a ramp function source.

C. Source Below a Layer

Finally, consider the case of a source below a slow, soft layer. In Figure 8 we compare radial and vertical components for strikeslip and dipslip sources. Notorious is that: (1) the strikeslip source first motion is impulsive and the dipslip is more similar to the headwave onset SPS, seen clearly on the strikeslip components; (2) first arrivals are more dominant on the vertical components than on the radial ones; and (3) a long-period arrival, probably an interface wave, begins about 4 1/2 seconds after the origin time. Compare the complexity of these traces with the explosion source of Figure 9. Generally, S leaving the source renders the seismograms much more complicated. The calculations for the ten source components required 15 seconds of CYBER 176 time to compute.

Acknowledgments

This work was begun at Lawrence Livermore Laboratory, where it

was supported by contract W-7405-ENG-48 from the Department of Energy. It was also supported by the Defense Advanced Research Projects Agency and was monitored by the Air Force Office of Scientific Research under contract F49620-77-C-0070.

References Cited

Chapman, C. H., 1973. Geophysics 204C Course Notes, University of California-Berkeley, Dept. of Geology and Geophysics.

Chapman, C. H., 1978. A new method for computing synthetic seismograms, *Geophys. J. R. Astron. Soc.*, 54, 481-518.

Cisternas, A., Betancourt, O. and A. Leiva, 1973. Body waves in a "real earth." Part 1, *Bull. Seismol. Soc. Am.*, 63, 145-156.

deHoop, A. T., 1961. Theoretical determination of the surface motion of a uniform elastic halfspace produced by a dilatational, impulsive point force, *La Propagation des Ebranlements dans les Milieux Heterogenes, Colloques Internationaux du Centre National de la Recherche Scientifique, Marseille*, 21-32.

Dey-Sarkar, S. K. and C. H. Chapman, 1978. A simple method for the computation of body-wave seismograms, *Bull. Seismol. Soc. Am.*, 68, 1577-1594.

Gilbert, F., 1970. Excitation of normal modes of the earth by earthquake sources, *Geophys. J. R. Astron. Soc.*, 22, 223-226.

Gilbert, F. and G. E. Backus, 1966. Propagator matrices in elastic wave and vibration problems, *Geophysics*, 31, 326-332.

Johnson, L. R., 1974. Green's function for Lamb's problem, *Geophys. Jour. R. Astron. S.*, 37, 99-132.

Lamb, H., 1904. On the propagation of tremors over the surface of an elastic solid, *Phil. Trans. Roy. Soc. London, A*, 203, 1-42.

Mase, G. E., 1970. Continuum Mechanics, Schaum's Outline Series, McGraw-Hill.

Peppin, W. A., 1974. The Cause of the Body Wave-Surface Wave Discriminant between Earthquakes and Underground Explosions at Near-Regional Distances, Ph.D. Thesis, Univ. of Calif.-Berkeley.

Peppin, W. A., 1977. A Body Wave-Surface Wave Seismic Discriminant at Very Close Distances, Technical Report Z, Air Force Office of Scientific Research, Contract F49620-76-C-0015.

Peppin, W. A. and C. G. Bufe, 1980. Induced versus natural seismicity: search for a seismic discriminant, *Bull. Seismol. Soc. Am.*, 70, 269-281.

Peppin, W. A. and M. R. Somerville, 1980. Spectral studies of earthquakes in the Mammoth Lakes, California region, Nov 1979 to mid July 1980, *EOS, Trans. Am. Geophys. Un.*, 61, 1041.

Sato, R., 1973. Seismic waves due to a dislocation source model in a multi-layered medium. Part I. Theory, *J. Phys. Earth*, 21, 155-172.

b

Sato, R., 1973. Seismic waves due to a dislocation source model in a multi-layered medium. Part II. Numerical calculations for a point source, *J. Phys. Earth*, 21, 401-414.

Stump, B. W., 1979. Investigation of Seismic Sources by the Linear Inversion of Seismograms, Ph.D. Thesis, Univ. of Calif.-Berkeley.

Stump, B. W. and L. R. Johnson, 1977. The determination of source properties by the linear inversion of seismograms, *Bull. Seismol. Soc. Am.*, 67, 1489-1502.

Wiggins, R. A. and D. V. Helmberger, 1974. Synthetic seismogram computation by expansion in generalized rays, *Geophys. J. R. Astron. S.*, 37, 73-90.

FIGURE CAPTIONS

Figure 1. Illustrates geometry of problem. Source is at "S", at a depth "h" below the free surface $X_3 = 0$. Receiver is at epicentral distance "r". "phi" is measured counterclockwise from east.

Figure 2. Gives notation for three problems P, SV, or SH incident at free surface. The factors P_{0ij} are the reflection coefficients at the free surface. Wavy lines denote travelling S-waves, straight lines denote P-waves. Vector notation is defined in (7).

Figure 3. The particular ray described in text. Leaves source as SV in the second layer, converts to P on reflection, and transmits to free surface as P. Epicentral distance is "r", source depth is "h".

Figure 4. Description of domain of integration (shaded) for a generalized ray such as shown in Figure 3, with two headwaves, arrival times t_{H1} and t_{H2} , and a Fermat time of t_F . The true diagram appears as the small one above (each front monotonically increases with t). For clarity the vertical scale is reduced to an appropriate slowness and expanded in the larger diagram below. Let the time " t_P " be selected at which to perform the quadrature. Then the domain of integration is the vertical strip at t_P covering the shaded region. As described in text, we subdivide the domain into three separate intervals using the limits e_1 , e_2 , and e_3 . Times t_{C2} and t_{C1} are the headwave cutoff times beyond which the headwave fronts have no physical

meaning. The Fermat integral extends to all times (area under curve labelled "tF" in top, smaller diagram).

Figure 5. Theoretical versus observed displacements for two earthquakes (left: 26 May 1980 1925 GCT, Mo 2E22 dyne-cm; right: 26 May 1857 GCT, Mo 1.7E23 dyne-cm). The epicentral distance and the focal depth are each about 5 km for these events. For the smaller event a rise time of 0.15 second is assumed, and for the larger event a rise time of 0.45 second. The observations are clipped after onset of S on the larger event. The "near-field terms" give the prominent ramp between the P and S. Synthetics assume a halfspace.

Figure 6. Radial, transverse, and vertical-component strikeslip seismograms for a source in a layer 32 km thick. Solid traces: this formulation; dotted traces: asymptotic Cagniard theory (Wiggins and Helmberger, 1974). Rays include the directs (P, S), the free-surface headwave (sP), and the first multiples (PP, PS, SP, SS). The vertical bars give amplitudes of 2E-25, 5E-25, and 1E-25 cm, respectively, for a source with a strength of 1 dyne-cm. Source time function is a ramp.

Figure 7. Same format as Figure 6 for a dipslip source; radial, transverse, and vertical components. The vertical bars are 1E-25, 1E-25, and 2E-25 cm for a source as in Figure 6.

Figure 8. For a source below a soft, slow layer 1 km thick. Left: strikeslip radial and vertical; right: dipslip radial and vertical. Raysum includes all directs and first multiples arriving before the S wave. "SPS" is the headwave associated with the direct ray SS, the S-wave. The source depth and receiver distance are 1.3 and 8 km, respectively. The layer velocities and density are 1.7E5, 1E5, and 2.0 cgs, and the halfspace velocities and density are 3.34E5, 1.95E5, and 2.7 cgs. On each trace the bar represents 1E-23 cm of displacement for a source with strength 1 dyne-cm. Source time function is a step

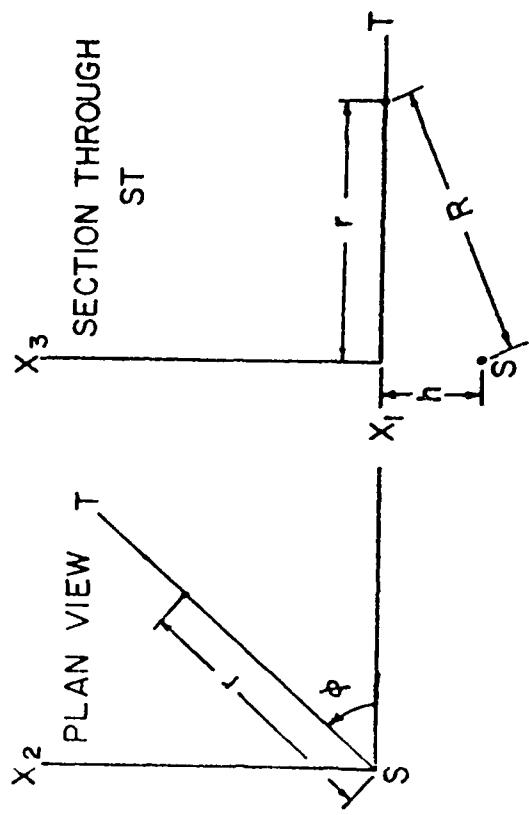


Fig 1

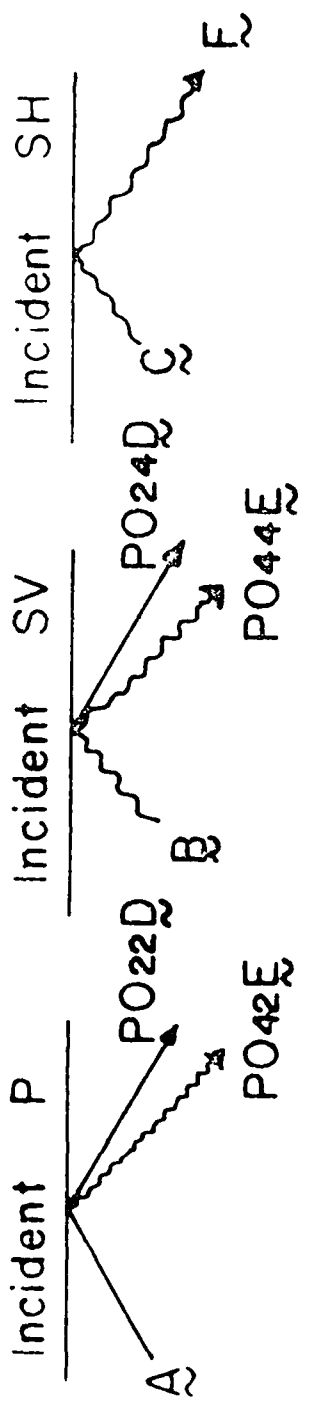


Fig 2

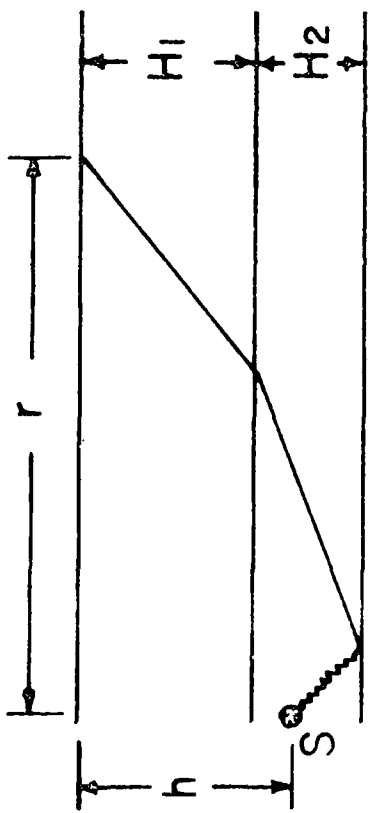


Fig 3

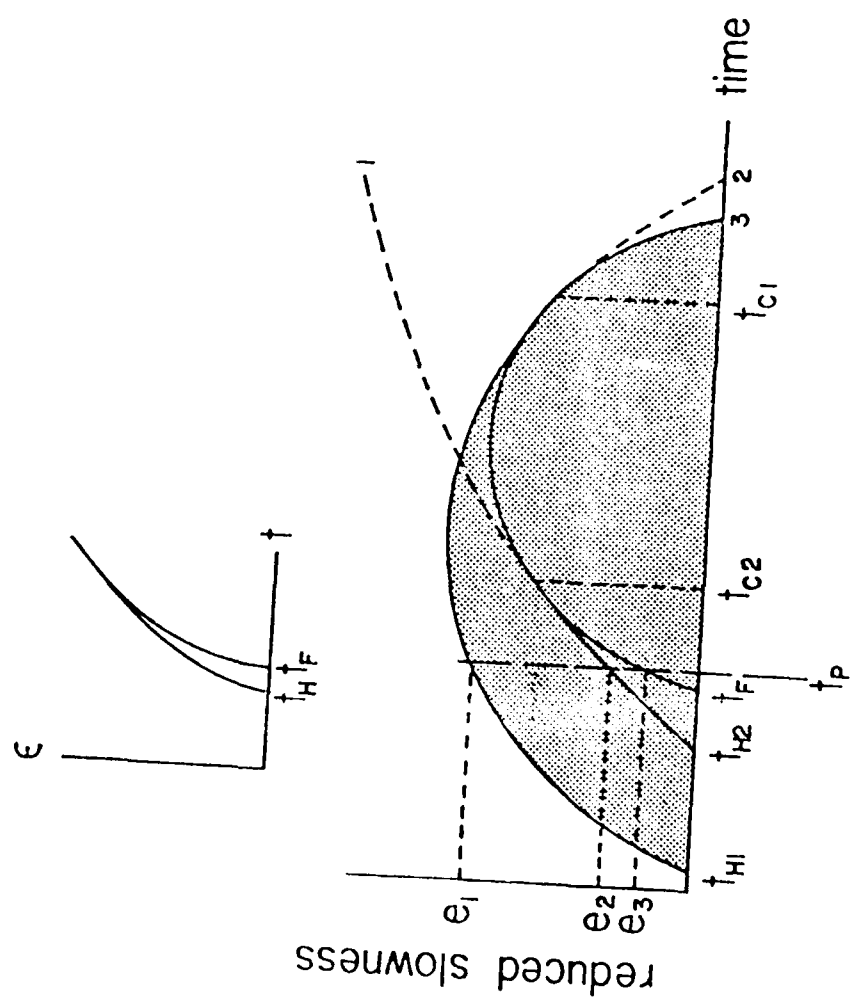


Fig 4

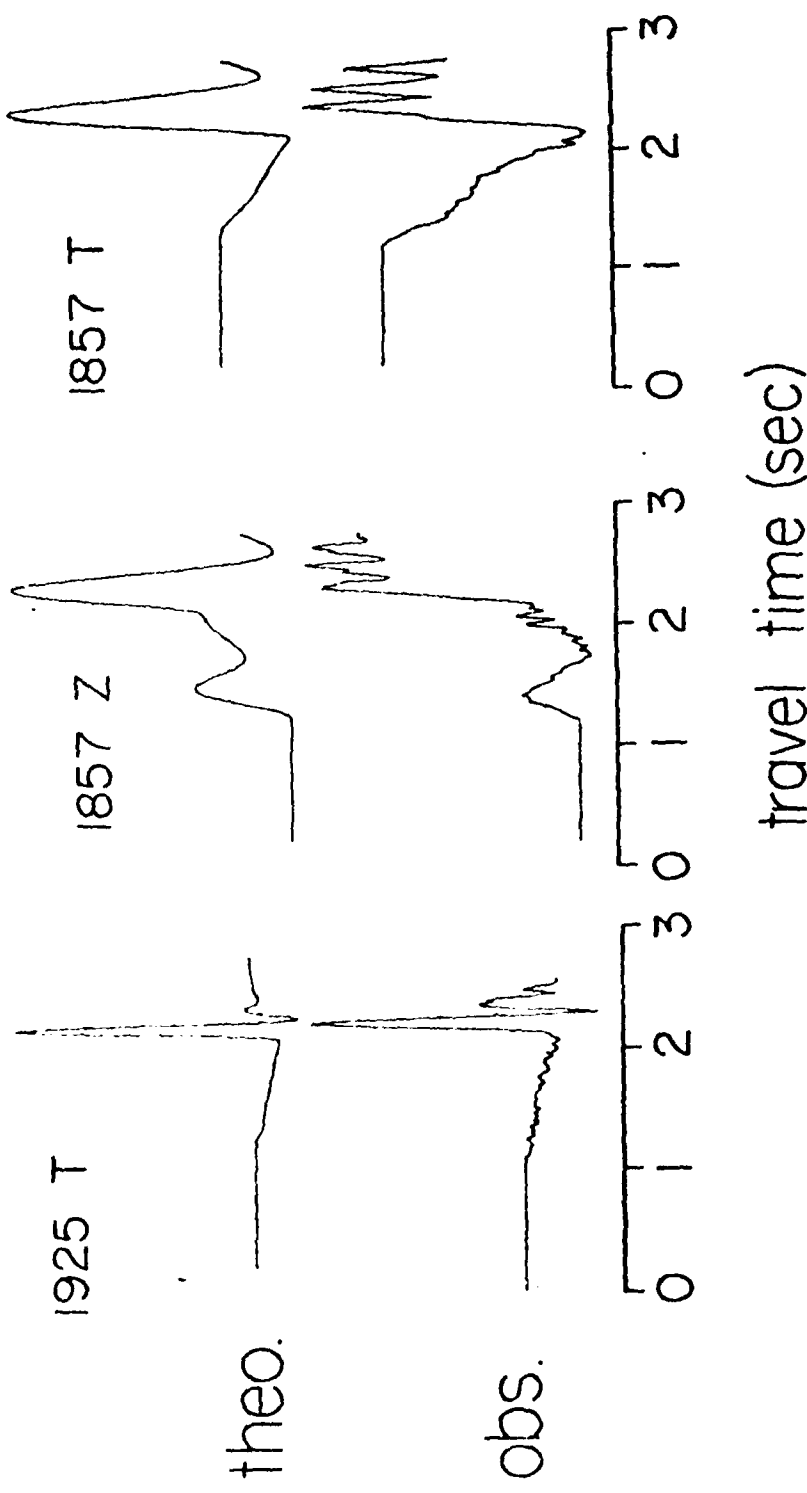


Fig 5

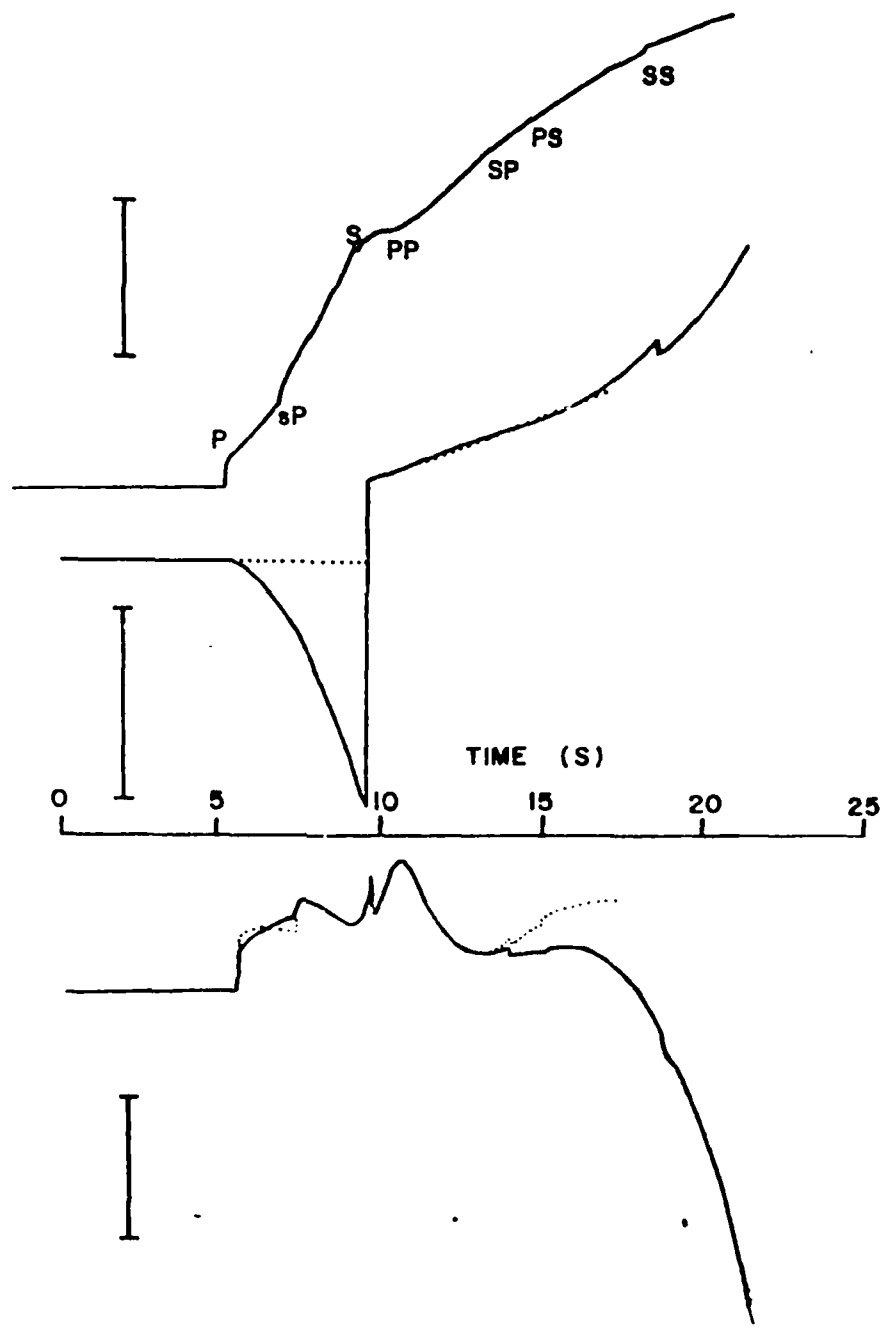


Fig 6

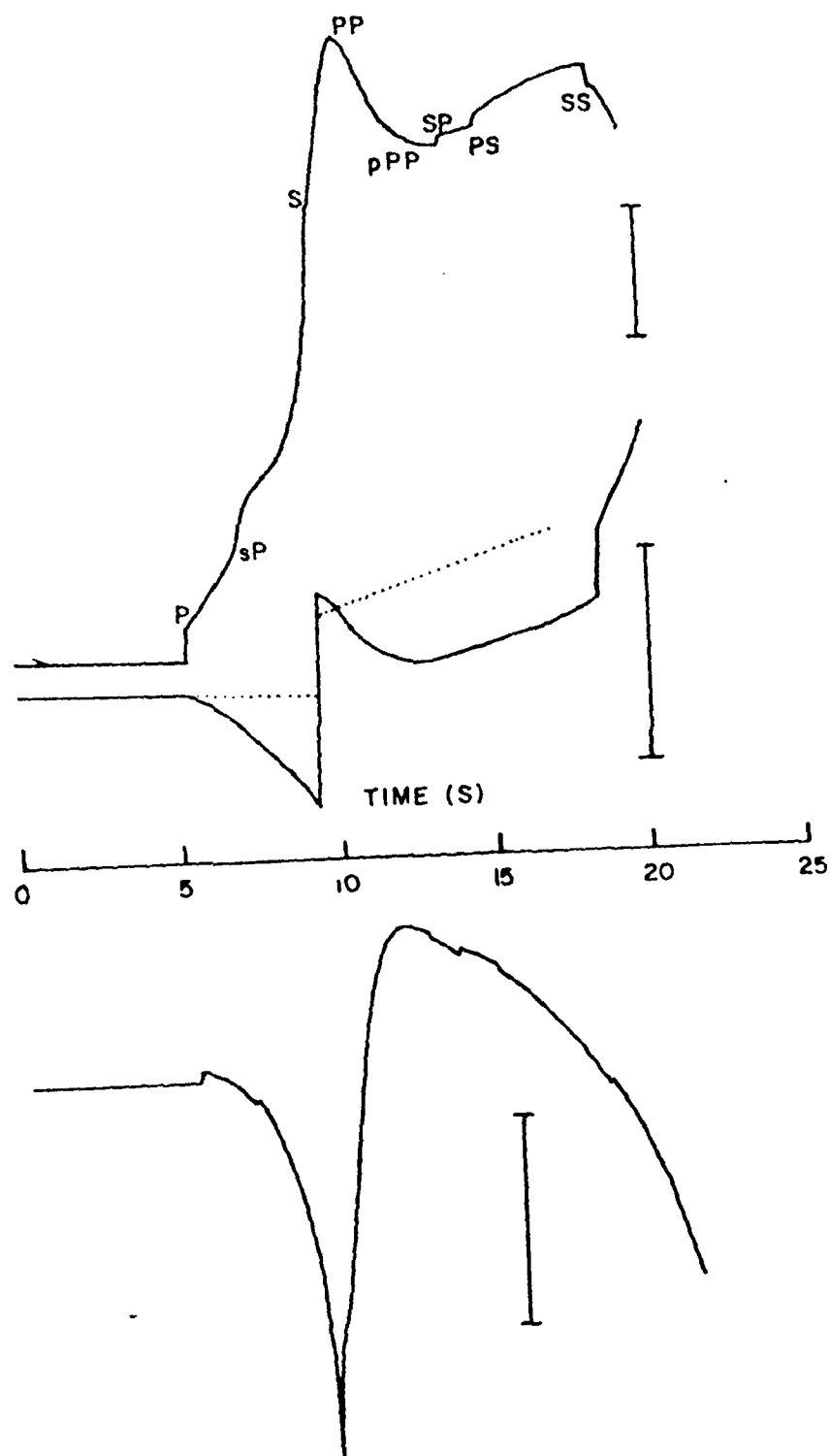


Fig 7

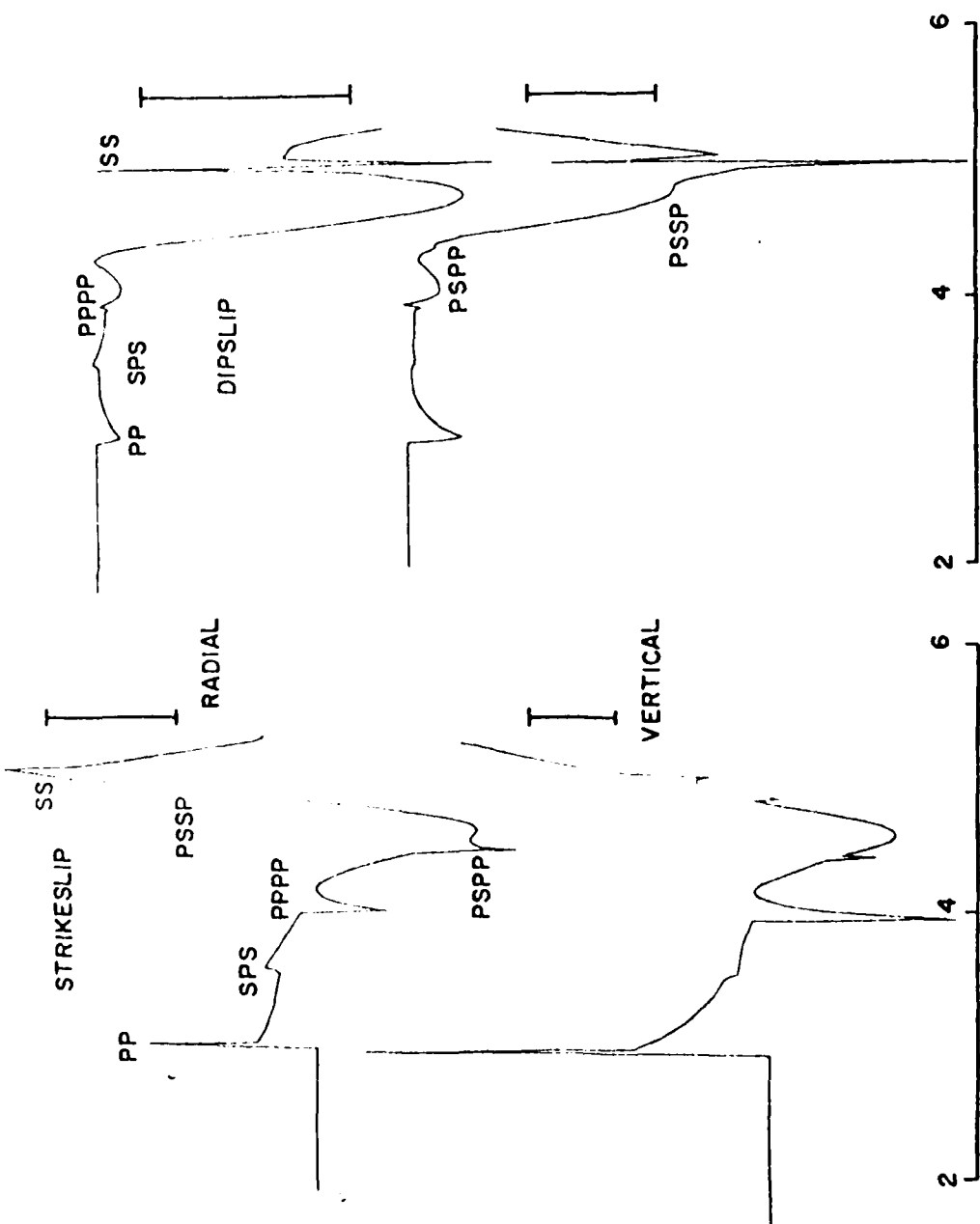


Fig 8

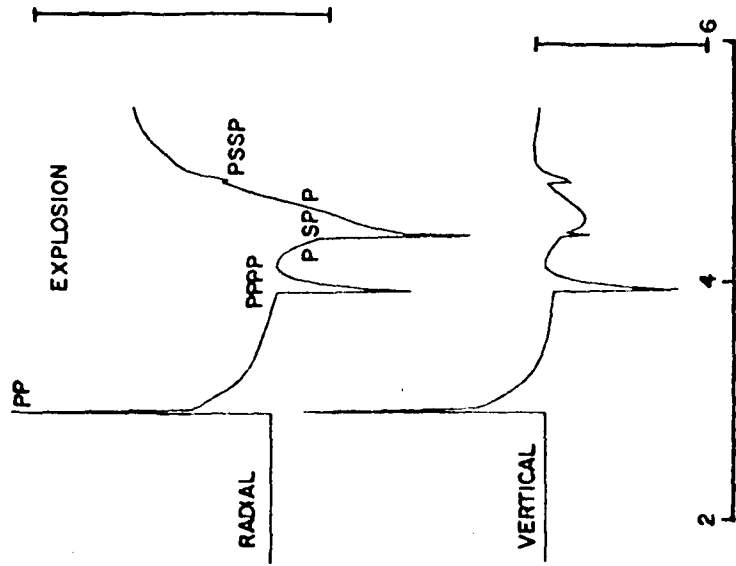


Fig 9

function, and the height of the spikes are conditioned by the sample interval of 0.02 second.

Figure 9. Same format as Figure 8 for the radial and vertical components of an explosion source. The bar is 1.5E-23 cm for a source of unit moment.

[7] SEISMIC DISCRIMINATION USING ONLY PN

William A. Peppin

SUMMARY. Using wideband (0.04 to 10 Hz) data recorded at the four Lawrence Livermore National Laboratory stations, two small Nevada Test Site explosions (12 May 1976 1950 GCT; 01 Nov 1978 1525 GCT) provide Pn data for this study. Using vertical and radial components, the seismograms were inverted for the seismic moment tensor. For each event, the moment tensor elements have significant diagonal components, giving correct identity of them as explosions. Moreover, a "master-event" procedure indicates that if one event is presumed to be an explosion, then the other event is similarly identified with high confidence.

Introduction

In view of recent movement toward a test-ban treaty involving seismic monitoring at regional distances, it is timely to evaluate new methods for seismic discrimination between explosions and earthquakes using regional seismograms. The recently-developed seismogram-inversion method of Stump & Johnson (1977) is

APPENDIX. Subroutine to compute source and receiver factors, together with spatial derivatives of the Green's functions.

Variable Names:

A	rotated horizontal slowness "a" in (17)
B	rotated horizontal slowness "b" in (17)
E	ϵ , where $b \equiv i\epsilon$ below (22)
CL	combined horizontal slowness " λ " in M of (5)
ETAA	vertical slowness n_α in (6)
ETAB	vertical slowness n_β in (6)
ETA-S	vertical slowness at source, "-" is α or β
FOR(J)	source factors for point force in direction X_j
GIJK	Green's function derivatives with respect to X_j (see Johnson, 1974)
LAYER	layer number containing the source
OMEGA	Ω defined below (7)
RALEY	Rayleigh's function defined in (15)
RECEIV(J)	receiver factors for radial, transverse, and vertical components at the free surface

This subroutine returns the 14 non-zero Green's function derivatives $g_{ij,k}$ which are combined via another subprogram into the canonical sources.

Studying this subroutine, the generalization to other problems (e.g., higher-order sources; solutions within the medium) is straightforward.

SUBROUTINE G3(LSQ,CA,E,RFLAG,SFLAG)
COMPLEX LSQ,CA

```
C COMPUTE GIJJ,K AND RETURN THE 14 NON-ZERO QUANTITIES
C THROUGH COMMON BLOCK /GREEN/. THIS COMMON BLOCK IS
C SHARED BY FUNCTION *V3* AND SUBROUTINE *ROMB4*.
C COMMON BLOCK /SUBS/ IS SHARED WITH CONTO2, DADT2,F2,
C ROMCLC,RTC0E2,XFER.
C
C COMMON /GREEN/ ETAA,ETAAS,ETAB,ETABS,GCALL,G111,G131,
+ G221,G311,G331,G122,G212,G232,G322,G113,G133,G223,G313,G333
  COMPLEX ETAA,ETAAS,ETAB,ETABS,G111,G131,G221,G311,G331,
+ G122,G212,G232,G322,G113,G133,G223,G313,G333
  COMMON /SUBS/ ALPHA(7),BETA(7),CMTORS,COEFFS(20),COSTH,FLAG,
+ INTYPE,JTYPE(20),KROOT,KRT,L,LAYER,LISTFL,LROMB,
+ NEWC(30),NEWH(30),NEWN,NEWNL,NJTYPE,NLIST(20),PROD,PU(7),
+ R,RHO(7),ROOT,SHEAR1,SINTH,T,TCTHOR,TFERMT,TORSMC,TSTHOR,U,
+ UROMB,USQ,XLSQ
  REAL L,LROMB,NEWC,NEWH
  COMPLEX COEFFS,PROD,ROOT
  INTEGER DERIV(14),FORCE(14),COMP(14)
  COMPLEX B,CL,DER(3),FACTOR,FAC2,FOR(3),OMEGA,RALEY,RECEIV(3),
+ TEMP(14)
  EQUIVALENCE (TEMP(1),G111),(TEMP(2),G131),(TEMP(3),G221),
+ (TEMP(4),G311),(TEMP(5),G331),(TEMP(6),G122),(TEMP(7),G212),
+ (TEMP(8),G232),(TEMP(9),G322),(TEMP(10),G113),(TEMP(11),G133),
+ (TEMP(12),G223),(TEMP(13),G313),(TEMP(14),G333)
  DATA DERIV,FORCE,COMP/1,1,1,1,2,1,2,2,3,3,3,3,1,3,2,1,3,
+ 2,1,3,2,1,3,2,1,1,2,3,3,1,2,2,3,1,1,2,3,3/
```

```

CL=CSQRT(LSQ)
B=(0.,1.)*E
DO 30 J=1,14
30 TEMP(J)=0.

C
C COMPUTE SOURCE FACTORS
C
IF(SFLAG.NE.1.)GO TO 1
C
C P UP FROM SOURCE
C
FACTOR=1./CSQRT(2.*RHO(LAYER)*ETAAS)
FOR(1)=-CA*FACTOR
FOR(2)=-B*FACTOR
FOR(3)=-ETAAS*FACTOR
GO TO 5
1 IF(SFLAG.NE.3.)GO TO 2
C
C P DOWN FROM SOURCE
C
FACTOR=1./CSQRT(2.*RHO(LAYER)*ETAAS)
FOR(1)=-CA*FACTOR
FOR(2)=-B*FACTOR
FOR(3)=ETAAS*FACTOR
GO TO 5
2 IF(SFLAG.NE.2.)GO TO 3
C
C SV UP FROM SOURCE
C
FACTOR=1./CSQRT(2.*RHO(LAYER)*ETABS)
FAC2=FACTOR*ETABS/CL
FOR(1)=-(0.,1.)*CA*FAC2
FOR(2)=-(0.,1.)*B*FAC2
FOR(3)=(0.,1.)*CL*FACTOR
GO TO 5
3 IF(SFLAG.NE.4.)GO TO 4
C
C SV DOWN FROM SOURCE
C
FACTOR=1./CSQRT(2.*RHO(LAYER)*ETABS)
FAC2=FACTOR*ETABS/CL
FOR(1)=(0.,1.)*CA*FAC2
FOR(2)=(0.,1.)*B*FAC2
FOR(3)=(0.,1.)*CL*FACTOR
GO TO 5
4 IF(SFLAG.LT.4.5)GO TO 5
C
C SH AWAY FROM SOURCE
C
FACTOR=CL*CSQRT(2.*PU(LAYER)*ETABS)
FOR(1)=-B/FACTOR
FOR(2)=CA/FACTOR
5 CONTINUE

```

```

C RECEIVR FACTORS, ONE FOR EACH VALUE OF *I*.
C
C IF(RFLAG.NE.1.)GO TO 6
C
C P UP AT RECEIVER
C
OMEGA=BETA(1)-2*LSQ
RALEY=OMEGA*OMEGA+4.*LSQ*ETAA*ETAB
FACTOR=1./(SHEAR1*RALEY*CSQRT(2.*RHO(1)*ETAA))
RECEIV(1)=-FACTOR*4.*ETAA*ETAB*CA
RECEIV(2)=RECEIV(1)*B/CA
RECEIV(3)=-FACTOR*2.*OMEGA*ETAA
GO TO 8
6 IF(RFLAG.NE.2.)GO TO 7
C
C SV UP AT RECEIVER
C
OMEGA=BETA(1)-2.*LSQ
RALEY=OMEGA*OMEGA+4.*LSQ*ETAA*ETAB
FACTOR=1./(SHEAR1*RALEY*CSQRT(2.*RHO(1)*ETAB))
RECEIV(1)=FACTOR*(0.,2.)*OMEGA*ETAB*CA/CL
RECEIV(2)=RECEIV(1)*B/CA
RECEIV(3)=-FACTOR*(0.,4.)*CL*ETAA*ETAB
GO TO 8
7 IF(RFLAG.NE.5.)GO TO 8
C
C SH UP AT RECEIVER
C
FACTOR=2./(CL*CSQRT(2.*PU(1)*ETAB))
RECEIV(1)=-B*FACTOR
RECEIV(2)=CA*FACTOR
8 CONTINUE
C
C SET UP FOR CORRECT SPATIAL DERIVATIVES
C "DER" CONTAINS FACTORS FOR DERIVATIVES WRT SOURCE
C COORDS X,Y,AND H. "SIGNUM" SET NEGATIVE FOR UPCOMING
C WAVES AND THE "H" DERIVATIVE.
C
DER(1)=CA
DER(2)=B
DER(3)=ETAA
IF((SFLAG.NE.1.),AND,(SFLAG.NE.3.))DER(3)=ETABS
DO 20 J=1,14
SIGNUM=1.
IF(((SFLAG.EQ.3.),OR,(SFLAG.EQ.4.),OR,(SFLAG.EQ.6.)),AND,
+ (DERIV(J).EQ.3))SIGNUM=-1.
IF(SFLAG.LT.4.5)GO TO 21
IF((J.NE.1),AND,(J.NE.3),AND,(J.NE.6),AND,(J.NE.7),AND,
+ (J.NE.10),AND,(J.NE.12))GO TO 20
21 TEMP(J)=RECEIV(COMP(J))*FOR(FORCE(J))*DER(DERIV(J))*SIGNUM
20 CONTINUE
C FACTORS GIJK RETURNED THRU COMMON (EQUIVALENCE TO TEMP)
RETURN
END

```

ideal in two ways for this problem: first, the method produces a complete set of source time functions, one for each component of the seismic moment tensor $M_{ij}(t)$, and second, confidence analysis is introduced naturally in the calculation. The decision as to the identity of an event involves examination of the trace $M_{11} + M_{22} + M_{33}$. If this quantity is large relative to the off-diagonal components, the event is identified as an explosion. "Large" can be defined to suit the criteria of the analysis.

I describe an effort to invert the seismic phase Pn for the moment tensor. Two explosions are considered: 12 May 1976, 1950 GCT, $ML = 4.6$, and 01 Nov 1978, 1525 GCT, $ML = 4.3$. The events are selected because they are fairly small and because appropriate seismic data is available. Seismic data analyzed consists of the radial, transverse, and vertical components of ground motion recorded by the wideband Lawrence Livermore National Laboratory (LLNL) stations MNV, 200 km NW, ELK, 400 km NNE, KAN, 350 km ESE, and LAN, 350 km S of the test site. Several considerations motivate the use of Pn alone in the analysis: (1) as it is a first arrival, it should be a relatively simple phase to synthesize at regional distances as compared with, say the complex Pg phase; (2) it samples a small cone of incidence angles (i.e., near a phase velocity of 8 km/s), so provides a somewhat standardized sampling of the source; (3) it is seen at great distances in Asia where discrimination is of interest; (4) at low-noise sites, magnitude 4 events can probably be investigated out to 1,000 km using this procedure; and (5) as it is mainly a deep-crustal phase, we can suppose it escapes some distortions caused by near-surface lateral variations. The disadvantages are that Pn is a small-amplitude phase and that it is not a direct wave. As a refracted wave it is sensitive not only to first-order velocity variations, but to second-order ones. In spite of these difficulties, the results obtained appear quite promising.

Method of Analysis

Data for the two explosions, recorded on analog magnetic tape (FM mode de-

viated 40%) was digitized at 50 samples/s after application of an anti-aliasing filter at 10 Hz. Windows 2.54 seconds long, including only the Pn and its related phases, but excluding direct arrivals such as PMP, were selected at the four LLNL stations. For 12 May the data traces used were: radial, transverse and vertical (R, T, Z) at MNV; Z at KAN; R, T, and Z at LAN; Z at ELK. For 01 Nov the same traces excepting the ELK vertical were used. The data was conditioned using a 10% cosine taper. In order to apply Stump & Johnson's (1977) procedure, we must: (1) select a suitable earth model, (2) compute the necessary synthetic seismograms, and (3) invert the seismograms for the moment tensor time traces $M_{ij}(t)$ using the "frequency-domain" approach. The model selected was a three-layer crust over a halfspace of 7.8 km/s (Priestley & Brune, 1978). The synthetic seismograms computed are for a shallow (1/2 km) source. Ten components of motion must be computed, namely the ten "canonical source components" (strike-slip, dip-slip, compensated linear vector dipole, and explosion). Any point source representable as a linear combination of Green's function derivatives can be represented as a linear combination of the ten canonical source components through the seismic moment tensor of order 2 (Stump, 1979). These source components were computed by exact Cagniard-deHoop theory (Peppin, 1981). Finally, the seismograms and source components are inverted for six time traces $M_{ij}(t)$, each 2.54 seconds long, using a generalized inverse technique.

Results

In Figure 1 we compare observed vertical-component Pn waveforms with the synthetic seismogram for an explosion source with a stepup time of 0.3 second. As can be seen, the data are distressingly unlike the synthetics. Thus, the outlook for success appears quite bleak. We fit only the vertical and radial components, downweighting the transverse ones, because the transverse components are hopelessly contaminated by multipathing (synthetic transverse two orders of magnitude smaller than verticals, but observed transverse of comparable amplitude). Examples of the fits between observed and synthetic seismograms are given in Figure 2. It is not notorious that the fits are very close, because

the number of components being fit is small (seven for 01 Nov and eight for 12 May); given as few as six components, an exact fit would be obtained for almost any Green's function selected. Note in the figure the tremendous difference in signal character for the two explosions; the inversion simply places this character in the time traces of $M_{ij}(t)$, giving an unacceptably long and complex source time history for these events.

Consider now the maximum (unsigned) trace amplitudes of $M_{ij}(t)$ for the two events. They are (normalized to unit determinant)

$$\begin{bmatrix} 1.37 & .534 & .00385 \\ .534 & 1.21 & .00781 \\ .00385 & .00781 & .732 \end{bmatrix}$$

for the 12 May event and

$$\begin{bmatrix} 1.51 & .532 & .0518 \\ .532 & 1.08 & .0187 \\ .0518 & .0187 & .749 \end{bmatrix}$$

for the 01 Nov event. We see that the diagonal elements dominate, which suggests that each event should be identified as an explosion. Moreover, suppose we declare that the 12 May event is indeed an explosion. Let factors P_{ij} be determined such that

$$\underline{M_{ij}} \text{ (12 May)} + P_{ij} = \det \underline{M_{ij}},$$

and let $\underline{P_{ij}}$ be added to the $\underline{M_{ij}}$ array for the 01 Nov event. Then the adjusted 01 Nov array becomes almost pure explosion in character:

$$\begin{bmatrix} .86 & .002 & -.048 \\ .002 & 1.13 & -.010 \\ -.048 & -.010 & .983 \end{bmatrix}$$

Thus, a "master-event" method is able to establish quite clearly the identity of an unknown if a known is established. This is a significant result because: (1) the signal character of the two events differs so greatly (Figure 2); (2) 12 May included data at Elko while 01 Nov did not; (3) 12 May was in Yucca Valley and 01 Nov was on Pahute Mesa, and (4) 01 Nov was overburied.

It is of some interest to investigate the deviatoric part of the $M_{ij}(t)$. At any specific time this array (with signs) has a set of eigenvectors which point in the principal directions of stress (Gilbert, 1973; Stump, 1979). Consider a stereographic plot of the eigenvectors for the 12 May event associated with the minimum and maximum eigenvalues (axes of compression and extension), shown in Figure 3. These axes cluster mainly about two areas on the stereonet. Strike-slip motion is indicated in a sense similar to some of the mechanisms observed by Hamilton & Healy (1969) for BENHAM aftershocks on Pahute Mesa.

Discussion

The results agree in one important aspect with other efforts at inversion (Stump, 1979; Stump & Johnson, 1981). It appears that the amplitudes of the M_{ij} will be insensitive to errors in the Green's functions selected, while the phase information is indeed quite sensitive. Thus, we can place little stock in the extended duration of the source (no doubt an artifact of incomplete knowledge of the Pn phase); nor can we place much confidence in the inferred directions of stress for the deviatoric part of the solution. However, it is clear that with better knowledge of the structure these results could be improved. Furthermore, the results presented here based only on amplitude of the M_{ij} appear to be of considerable interest.

Note that we have attempted no inversion of earthquake data using the Pn phase (lack of any known suitable event near the test site recorded on the three-component LLNL stations). We have good reason to suppose that any Pn data will invert to a significant isotropic component in M_{ij} , since, for example, Pn

contains no significant SH component (apart from multipathing) which would tend to drive down the isotropic component. However, it is difficult to believe that our master-event technique, applied to an earthquake, would give so nearly an isotropic result. Moreover, in Figure 3 we see the potential for analysis of the deviatoric part of the source. For a pure explosion, we should have expected a patternless distribution of eigenvectors (this is the degenerate eigenvalue problem). Figure 3 provides the opportunity to estimate the focal mechanism from a considerable number (up to one estimate for each seismogram time sample, here 128) of independent estimates. In sum, this line of analysis appears definitely worth pursuing in connection with seismic discrimination, with the present results quite encouraging.

Acknowledgments

This work was supported by the Defense Advanced Research Projects Agency and was monitored by the Air Force Office of Scientific Research under contract F49620-77-C-0070. Brian Stump kindly provided the use of his inversion program. Jim Hannon of LLNL cooperated in obtaining the data used in this analysis. The University of California Seismographic Station kindly provided facilities for digitization of the seismograms.

References Cited

Gilbert, F., 1973. Derivation of source parameters from low-frequency spectra, Phil Trans. Roy. Soc. London, Ser. A., 274, 369-371.

Hamilton, R. M. & Healy, J. H., 1969. Aftershocks of the BENHAM nuclear explosion, Bull. seism. Soc. Am., 59, 2271-2281.

Peppin, W. A., 1981. Impulse solutions for a layered elastic medium: extended Lamb's problem, J. phys. Earth, submitted.

Priestley, K. F. & Brune, J. N., 1978. Surface waves and the structure of Nevada and western Utah, J. geophys. Res., 83, 2265-2280.

Stump, B. W., 1979. Investigation of Seismic Sources by the Linear Inversion of Seismograms, Ph.D. Thesis, University of California-Berkeley.

Stump, B. W. & Johnson, L. R., 1977. The determination of source parameters by the linear inversion of seismograms, Bull. seism. Soc. Am., 67, 1489-1502.

Stump, B. W. & Johnson, L. R., 1981. The effect of Green's functions on the determination of source mechanisms by the linear inversion of seismograms, manuscript in preparation.

Figure Captions

Figure 1. Comparison of synthetic seismogram, vertical component, with observed vertical components at Landers (left) and Elko (right). Top traces: computed ground displacement, step-function source; second traces: after applying instrument correction, essentially to ground velocity; third traces: convolution of second trace with a source time function of 0.3 second stepup time; bottom traces: data. The synthetics consist almost entirely of the downgoing Pn and its reflection at the free surface; other phases are multiples in, the top (3 km thick) layer.

Figure 2. Comparison of observed seismograms (top of each pair) with fitted seismograms (bottom of each pair). Left: 12 May 1976; right: 01 Nov 1978. On the radial traces away from the source is up, and on the vertical traces compression is downward. The relative scales of the pairs are correct. The fits are as good on vertical and radial traces not shown, but not on the transverse, which were downweighted.

Figure 3. Stereo projection of axes of compression (left) and extension (right). Each point gives the eigenvectors of $M_{ij}(t)$ at a particular time step. The inferred mechanism is NW strikeslip, either right-lateral or left-lateral, depending on how the clusters on the stereonet are selected.

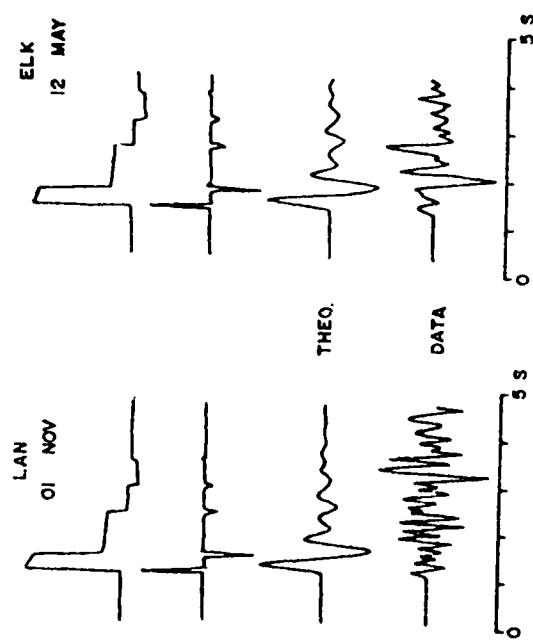


Fig 1

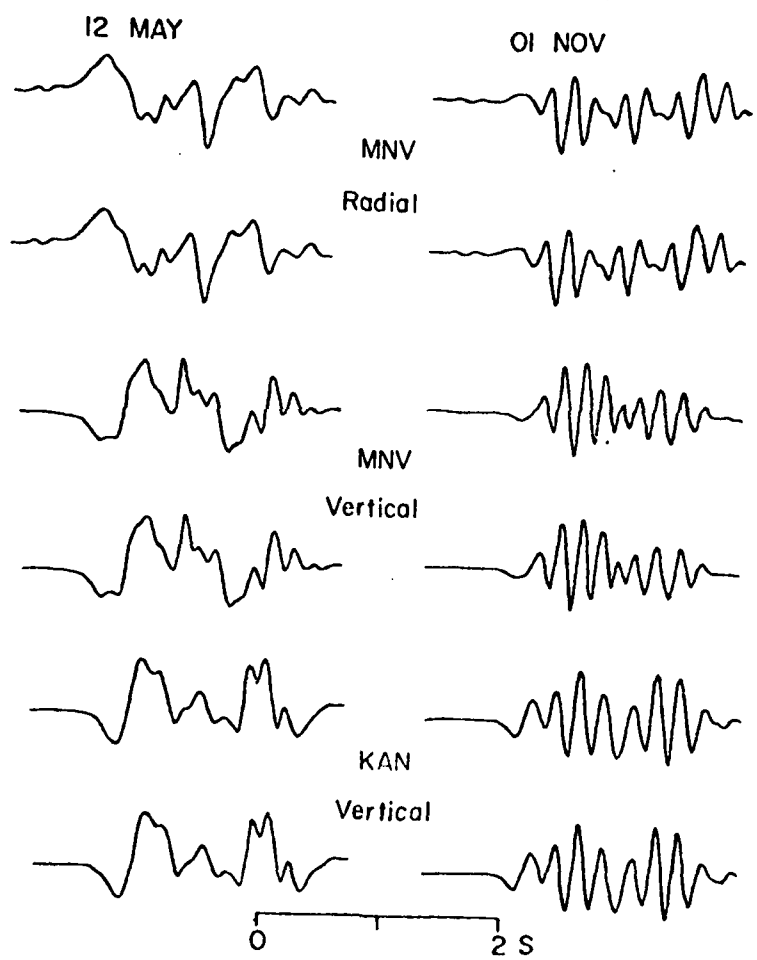


Fig 2

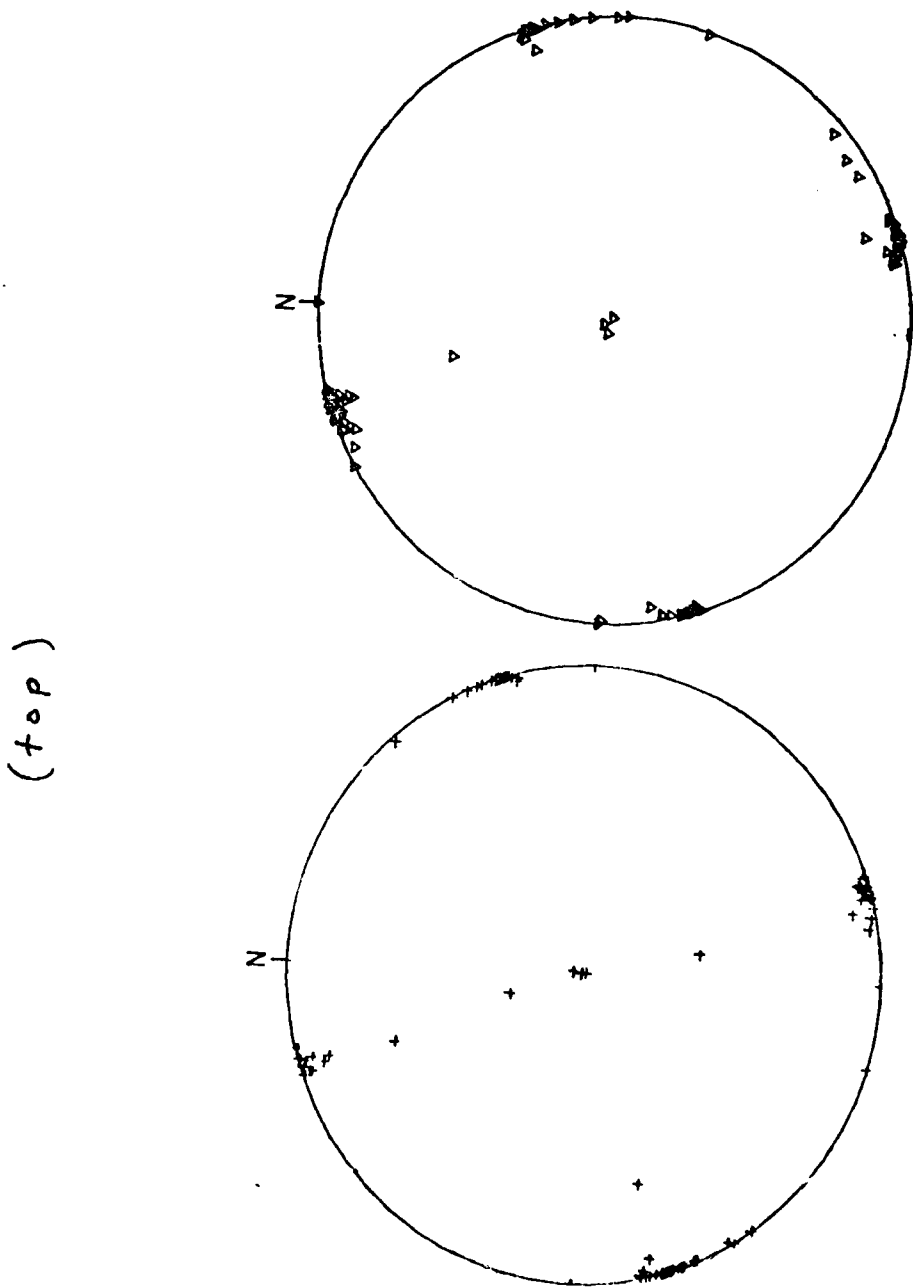


Fig 3